Aus dem Mannheim Institute for Intelligent Systems in Medicine (MIISM)

der Medizinischen Fakultät Mannheim
(Direktor: Professor Dr. med. Frank Giordano)

LOW DOSE RATE PROSTATE BRACHYTHERAPY

Inauguraldissertation
Zur Erlangung des Doctor scientiarum humanarum (Dr. sc. hum.)

der

Medizinischen Fakultät Mannheim

der Ruprecht-Karls-Universität

zu

Heidelberg

Vorgelegt von
Ernest Chukwudi Nwabueze Okonkwo

aus

Bamenda, Kamerun

2025

Dekan: Prof. Dr. med. Sergij Goerdt

Referent: Prof. Dr. rer. nat. Jürgen W. Hesser

Table of Contents

Appendix

List of Tables

List of Figures

List of Abbreviations

PTV	Planning Target Volume
PSA	prostate-specific antigen
I-125	Iodine-125
Pd-103	Palladium-103
Cs-131	Cesium-131
CCD	Charge Coupled Device
CT	Computer Tomography
MRI	Magnetic Resonance Imaging
AAPM	American Association of Physicists in Medicine
TG	Task Group
DVH	Dose Volume Histograms
EBRT	External Beam Radiation Therapy
GEC-ESTRO	Groupe Européen de Curiethérapie and European Society for Radiotherapy and Oncology
HDR	High-Dose-Rate
ITP	Inverse Treatment Planning
I-125	Iodine-125
POM	Polyoxymethylene
LDR	Low-Dose-Rate
LDR-PB	Low-Dose-Rate Prostate Brachytherapy
OARs	Organs at Risk
Bq	Becquerel
SNR	Signal-to-Noise Ratio
RT	Radiation Therapy
TPS	Treatment Planning System
TRUS	Transrectal Ultrasound
LCD	Liquid Crystal Display

1. Introduction

Prostate cancer is among one of the most common cancers affecting men worldwide, with a steadily increasing incidence projected to continue. According to the GLOBOCAN (Global Cancer Observatory) 2022 report, an estimated 1.47 million new cases were diagnosed in 2022. It is the second most common cancer and ranks fifth among cancer-related deaths in men worldwide. The incidence is notably higher in Europe and North America than in sub-Saharan Africa and the Caribbean, where the mortality rate is higher due to limited access to treatment services [1][2], with key factors such as age and diet, influencing the risk of prostate cancer [3].

Advancements in prostate cancer screening, mainly through prostate-specific antigen (PSA) testing, have improved early diagnosis and led to higher survival rates [4]. Early detection allows patients to be presented with various treatment options tailored to the stage of the disease [4]. These treatment options include active surveillance, hormonal therapy, radical prostatectomy, brachytherapy, cryotherapy, and external beam radiation therapy (EBRT). In some cases, combined modality therapy, such as brachytherapy with EBRT, may be the recommended option.

Prostate cancer is classified into four stages. Staging is determined by the Gleason score that is assessed at biopsy. Stage 1 is defined as low-risk cancer, where the tumour is confined to the prostate, whereas stage 4 is defined as high-risk cancer, where the cancer has spread beyond the prostate. As highlighted by the Institute for Clinical and Economic Review (ICER), treatment options for low-risk prostate cancer generally offer similar effectiveness [5]. However, some advantages of brachytherapy include escalation of the dose to the primary target organ and reduction of treatment-related toxicities due to the rapid dose drop-off that minimises dose to the surrounding Organs at Risk (OARs). Moreover, brachytherapy is cost-effective compared to other treatment modalities [6].

Prostate brachytherapy can be administered as low-dose-rate prostate brachytherapy (LDR-PB), also known as permanent interstitial seed implants, is illustrated in Figure 1.1 [7]) with the patient positioned in the lithotomy position, or high-dose-rate prostate brachytherapy (HDR-PB). In HDR-PB, the radioactive source, usually Iridium-192, is precisely driven to the predefined targets within the prostate. The source delivers the dose at each planned location by dwelling in the position for the determined duration. After applying the prescribed dose, the source is retracted into its shielded storage.

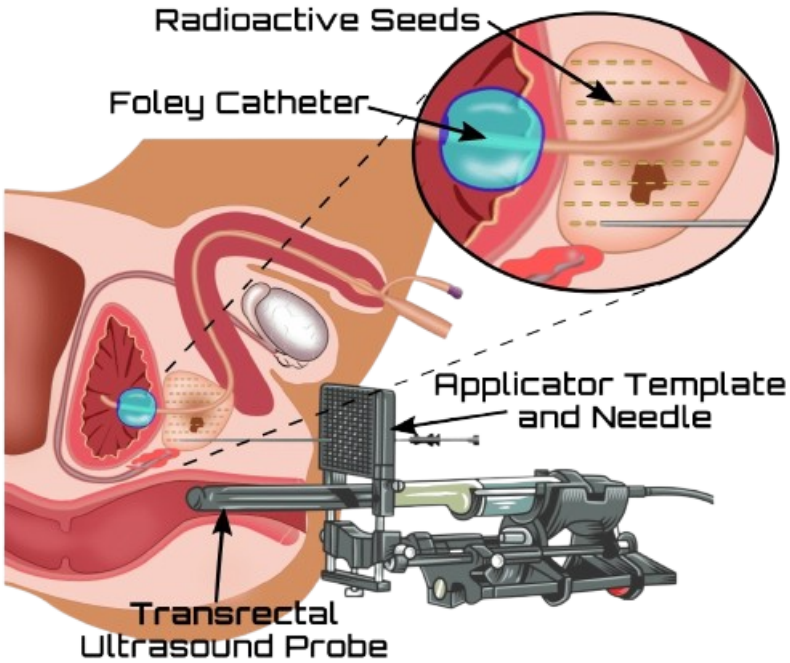

Figure 1.1: Schematic of low-dose-rate transrectal ultrasound prostate brachytherapy adapted with permission from OncologyMedicalPhysics [7]).

Despite the advantages and progress made over the years in the use of radioactive isotopes for the treatment of prostate cancer brachytherapy, there has been a decline in hospitals able to offer the multidisciplinary treatment modality to prostate cancer patients. This decline is attributed to various challenges associated with the modality [8][9]. The challenges include, but are not limited to, the complex nature of the multidisciplinary work environment, the steep learning curve involved, the apparatus for radioactive seed handling, the low reimbursement compared to other modalities such as EBRT, and patient selection criteria, especially with respect to prostate size and prediction of pubic arch interference [10].

The purpose of this study is to investigate the impact of strategies aimed at improving the workflow of LDR-PB so as to mitigate some of the challenges associated with the modality. This study aims to investigate strategies to address some of the challenges associated with LDR-PB, to make the procedure's workflow less complex, to help stop its decline, and to encourage more hospitals to make the treatment modality available to patients with prostate cancer.

1.1 Motivation and Objectives

LDR-PB involves the implantation of radioactive sources (Iodine-125 (I-125), Palladium-103 (Pd-103), or Cesium-131 (Cs-131)) into the prostate. The dose rate range is typically between 0.4 and 2 Gy/h [11]. As already mentioned, LDR-PB is an effective and well-established treatment modality for localised prostate cancer, with extensive literature that shows high disease control rates and minimal treatment-related toxicity [12][13][14][15][16]. However, its use has decreased in recent years. Compared to other modalities like EBRT, there has been less research focused on ways to improve the multidisciplinary procedure. This study addresses some of the key factors that have contributed to the decline of LDR-PB [17]. This includes the steep learning curve for novice brachytherapists, the need for workflow optimisation, modification of the QuickLink™ loader used for seed strand configuration, and the use of non-rigid templates [18].

The study analyses an LDR-PB patient databank to confirm the effectiveness of the modality as reported in the literature [19]. By validating the patient data and addressing the aforementioned challenges, the work aims to simplify the LDR-PB procedure, improve radiation protection, and enhance patient outcomes in terms of dose coverage to the target tissue and less dose to the OARs.

The study investigates aspects of the challenges by focusing on four areas: template design, source strength verification, seed-strand logistics, and shortening of the steep learning curve. Beginning with the introduction, this thesis is divided into five chapters. Following the introduction are the chapters on the materials and methods, results, discussion, and conclusion of the work. The complete list of publications section contains two submitted articles that are part of this study. The accepted manuscript, based on the proposed strategy for shortening the learning curve in LDR-PB, is still to be published. In line with

the Task Group 64 (TG-64) report [20], the journal article by the author of this dissertation together with a physician colleague (both as first authors) demonstrates the importance of combined expertise leading to optimal treatment outcomes for prostate cancer patients treated with LDR-PB at the Ortenau Klinikum between March 2002 and July 2016 [19].

1.2 Background

The LDR-PB treatment technique has advanced from a pre-planned method to an intraoperative procedure, where planning and implantation are performed in the operating room during the same session under transrectal ultrasound (TRUS) guidance [21]. Treatment planning and delivery are performed interactively, allowing real-time guidance of seed/seed strand deposition in the prostate. Hence, this enables adjustments to optimise the dose distribution to the target tissue while ensuring that the dose to the OARs is minimal. This real-time intraoperative planning showcases the significant advances in ultrasound imaging technology, leading to image-guided brachytherapy (IGBT), thereby facilitating personalised and adaptive treatments in prostate brachytherapy [22][11]. Furthermore, computer tomography (CT) and magnetic resonance imaging (MRI) are also used to assess possible interference with pelvic anatomy and to confirm prostate size, supporting the patient selection process. CT is also used for post-implant dosimetric planning, which is usually conducted four weeks after the implant [23][24]. MRI, combined with TRUS imaging during the intraoperative volume study process, allows better visualisation of localised prostate tumours. This is an essential factor in focal prostate therapy, where only the tumour lesion is targeted [25]. The benefit of focal prostate brachytherapy lies in the minimal radiation dose to unaffected areas of the prostate gland and surrounding OARs owing to the steep dose gradient [26].

1.2.1 Radioactive Source and Seed Technology

Radium was the first radioactive source used in the treatment of prostate cancer in 1911. It was temporarily inserted into the prostate through a urethral catheter. Since 1917, implantation has been performed transperineally [27]. Today, LDR-PB involves the permanent implantation of tiny solid radioactive seeds in the prostate target volume. They generally have a length of approximately 4.5mm and a diameter of about 0.8mm. This enables transperineal insertion through

needles into the prostate target volume. The most widely used radioisotopes are I-125, Pd-103, and more recently, Cs-131 [15]. Table 1.1 shows the frequently used radioisotopes and their properties [28][29][30]. Cs-131 was introduced in the early 21st century to address the need for a source with a short half-life. This allows for faster radiation delivery compared to I-125 and Pd-103. This means that with a half-life of 9.7 days, most of the dose is delivered within weeks, leading to faster patient recovery from toxicity-related effects and improved PSA control outcomes [31]. Similar to I-125, Cs-131 decays via electron capture. It generates photons with prominent peaks in the range between 29 to 34 keV [32]. Several dosimetric studies have shown that Cs-131 has a better implant dose distribution than I-125 and Pd-103 [14][33].

The delivery of radioactive seeds has advanced and shielded packaged seeds can be delivered (classified as UN2910) on the same day of the implant (just in time delivery before the implant) [34]. Users can also order extra calibrated radioactive seeds to verify their activity strength, as recommended by the American Association of Physicists in Medicine (AAPM) and the Groupe Européen de Curiethérapie-European Society for Radiotherapy and Oncology/Advisory Committee on Radiation Oncology Practice (GEC-ESTRO/ACROP) [35][36]. Vendors such as Eckert & Ziegler™ and Bard™ Medical provide various seed delivery options [37][38]. The Eckert & Ziegler™'s IsoSeed® radioactive seeds can be delivered as single seeds or preloaded needles [39]. There is also the option of stranded seeds with biodegradable spacers called IsoCords®. Similarly, Bard™ Medical offers seeds in Mick® cartridges, preloaded needles, or the QuickLink® delivery system. The QuickLink® system allows brachytherapists to assemble seed trains with biodegradable spacers according to the treatment plan. Biodegradable spacers improve seed placement and dose distribution and reduce seed migration and loss [40]. The spacers remain in the prostate for approximately 3-6 months before complete decomposition. The seeds are made of biocompatible materials that can remain in the prostate permanently without harming the patients.

Several innovative source designs and their dosimetric characteristic were recently investigated, with results offering promising prospects for the future of LDR-PB. One such source design is the implantable CivaSheet®/ CivaStrings® Pd-103 radioactive source [41][42][43]. Using a straight or bent string radioactive source can significantly reduce dosimetric variations caused by seed bunching and migration [44]. The development and usage of biodegradable

	Iodine-125	Palladium-103	Cesium-131
Half life (days)	59.4	16.99	9.65
Photon Energies (keV)	27-35	20-23	29-35
Dose Rate Constant (Gy/h U)	.0096 - .0104	.0069	.0105
Decay	X-ray / Gamma photon	Gamma photon	Gamma photon
Daughter nuclide	Tellurium-125	Rhodium-103	Xenon-131
Delivery rate	90% in 204 days	90% in 58 days	90% in 33 days
Monotherapy (Gy)	145-160	120 - 125	115
Anisotropy Factor	0.930	0.877	0.969

Table 1.1: Characteristics of commonly used Isotopes in LDR Prostate Brachytherapy.

materials to minimise and prevent seed bunching and migration has become a standard method. In addition to the mentioned developments, the advent of electronic brachytherapy with operational kilovoltages of less than 100kV is also a treatment option for prostate cancer patients [45].

1.2.2 Theory

The decay of I-125 occurs via electron capture, in which the nucleus captures an inner orbital electron, resulting in the conversion of a proton into a neutron and the emission of a neutrino. This process leaves the nucleus in the excited state. Because of electron capture, a vacancy is created in the inner K-shell of the atom, which is filled by an electron from a higher shell. The energy released during these electronic transitions produces characteristic X-rays in the 27-31 keV range. Additionally, Auger electrons may be emitted due to energy transfer during relaxation. After electron capture, low-energy gamma photons (approximately 35 keV) are emitted as part of the nuclear de-excitation process. The decay process can be represented as follows:

$$^{125}\text{I} + e^{-} \rightarrow ^{125}\text{Te}^{*} + \nu_e + \gamma_{\text{35 keV}} + \text{X-rays}_{\text{27-31 keV}} \tag{1.1}$$

Where:

- ^{125}I is the iodine-125 nucleus,
- e^{-} is the captured electron,
- $^{125}\text{Te}^{*}$ is the excited state of tellurium-125,
- ν_e is the emitted neutrino.
- $\gamma_{\text{35 keV}}$ represents the emission of gamma photons with energy around 35 keV,
- $\text{X-rays}_{\text{27-31 keV}}$ represent the characteristic X-rays emitted as electron transitions to fill inner-shell vacancies in the tellurium atom, typically in the K-shell to L-shell range (27-31 keV).

The photoelectric effect is the primary mode of interaction between the photons emitted by I-125 and matter. Other less significant interactions in this energy range include Compton scattering, Auger electron emission, and Rayleigh (coherent) scattering. These interaction modes are illustrated in Figures 1.2 and 1.3.

In the photoelectric effect, a photon is fully absorbed by an electron bound to an atom, transferring all of its energy to the electron. This causes the electron to be liberated from the atom, resulting in the atom becoming ionised. This

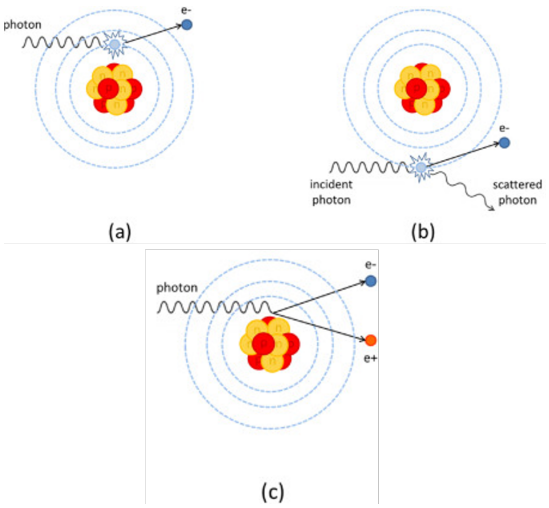

Figure 1.2: The three main photon interaction processes of interest in radiation therapy. (a) Photoelectric effect, (b) Compton effect, (c) pair production[46].

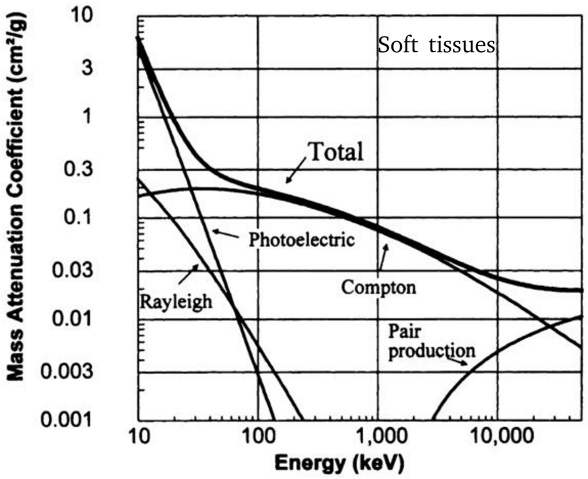

Figure 1.3: Mass attenuation coefficient for soft tissues ($Z \approx 7.5$) plotted against photon energy, highlighting the contributions of various photon interaction processes, including Rayleigh scattering, photoelectric absorption, Compton scattering, and pair production [47].

interaction is critical for energy deposition in tissues. The kinetic energy of the liberated electron is given by:

$$KE_e = h\nu - BE_b \tag{1.2}$$

Where:

- KE_e is the kinetic energy of the liberated electron,
- $h\nu$ is the energy of the incident photon,
- BE_b is the electron's binding energy in the atom [48].

This process is called direct ionisation, where a photon dislodges an electron from an atom. In indirect ionisation, photons break molecular bonds, such as water molecules, leading to the creation of reactive radicals such as hydroxyl radicals. These radicals can damage critical cellular components such as DNA, proteins, and membranes. Depending on the extent and type of damage, the cell may undergo one of the following responses: it may attempt to repair the damage, experience mutations due to incorrect repair, or undergo cell death if the damage is too severe. In radiation therapy, the goal is often to induce cell death in tumour cells while limiting the damage to healthy tissues.

1.2.3 Treatment Planning

The success of LDR-PB can be partly attributed to the gradual, continuous development of the treatment workflow. Some notable processes, such as pre- and post-planning, have been incorporated into the brachytherapy treatment planning system (TPS). The pace of its development has been relatively slow compared to other treatment modalities, such as EBRT, where significant resources have been invested in advancing the TPS. In comparison, research and investment in TPS for LDR-PB have been limited. However, owing to continuous investigative efforts by the brachytherapy community to enhance the modality, significant changes in planning strategies have been achieved. These changes have led to improved post-implant dosimetry outcomes, minimised toxicity, preserved organ functionality, and enhanced quality of life for patients [49]. Modern LDR-PB techniques have evolved beyond manual seed placement methods such as the Patterson-Parker, Quimby, and Paris techniques [50][51][52][53]. Currently, treatment planning systems utilise advanced algorithms that optimise seed placement based on the patient's specific anatomy, proximity to OARs, and tumour shape.

The globally used brachytherapy dosimetric protocol for calculating the dose delivered by implanted radioactive seeds is the TG-43 from the AAPM [54]. The TG-43 is based on detailed experimental measurements or Monte Carlo simulations of dose-rate distributions around radioactive seeds rather than simple point- or line-source approximations. This protocol uses source-specific parameters such as the dose-rate constant, radial dose function, seed geometric factor and anisotropy factor to estimate the dose distribution. However, the TG-43 protocol has limitations, as it assumes a homogeneous medium (water), that does not account for tissue heterogeneity, which is an essential factor affecting dose distribution. Additionally, TG-43 does not account for seed-to-seed interactions, which may influence dose accuracy [55].

Advanced methods such as model-based dose calculation algorithms are now being implemented to account for tissue heterogeneity in brachytherapy [56]. However, in LDR-PB, where TRUS is the primary imaging modality, the limitations of the TG-43 protocol remain. Real-time ultrasound imaging provides good spatial information but lacks the electron density information necessary for accurate dose calculation correction. Monte Carlo simulations have demonstrated the importance of considering tissue heterogeneity in dose calculations,

particularly for LDR brachytherapy sources, with potential differences in dose distribution of up to 15 % depending on tissue composition [55].

This consideration is particularly important in cases involving prostate calcification or reimplantation, in which previously implanted seeds may remain. Precise treatment planning requires accurate system commissioning, ensuring that it reflects the radiation characteristics of specific seeds, as outlined in the AAPM TG-56 and TG-43U guidelines [57]. Inverse planning—a method where the desired dose distribution is first defined [58][59], and then optimisation algorithms such as simulated annealing and greedy optimisation are used to determine the optimal seed placement—is now widely used in LDR-PB [60]. Some TPS, such as VariSeed™, include analytical tools such as sector analysis, which help clinicians adjust the maximum dose based on tumour localisation identified from biopsy results. Transperineal ultrasound-guided biopsy data can be integrated into the system, enabling real-time mapping, tracking and optimisation of seed placement in the cancerous regions of the prostate [61]. This facilitates tailored, image-guided treatment, with the option of incorporating MRI fusion for even greater precision in targeting the tumour based on localisation [62][63].

As artificial intelligence and machine learning evolve, new algorithms could revolutionise treatment planning, potentially enabling automated planning with robotic implantation for even greater precision and efficiency in LDR-PB [64].

1.3 State-of-the-art

1.3.1 Insertion Templates

Rigid templates are essential components in LDR-PB. They generally consist of a physical block with a two-dimensional grid system with holes spaced 5mm apart. The grid axes are annotated with numbers and letters, allowing the treatment planner to communicate precise needle insertion points to the physician. Vendors offer two template types: reusable and disposable. The template as presented in the schematic in Figure 1.1 plays a key role in guiding transperineal needle insertion, ensuring consistency in needle insertion, and placement of radioactive seeds within the prostate. By providing a stable and reproducible framework, the templates help to minimise needle deflection. In addition, the straight path it provides for the needles helps minimise damage to

surrounding critical structures, such as the urethra and rectum. The physical template fixed to the stepper must be aligned with the TRUS imaging system and TPS grids to ensure the accuracy of needle insertion. Misalignment between the electronic imaging grid and physical grid can lead to suboptimal dose distribution, thereby increasing the risk of treatment failure and unnecessary doses to organs at risk.

Recent advancements include the development of 3D-printed patient-specific templates tailored to each patient's anatomy, allowing for better flexibility in needle trajectories and improved dosimetric outcomes [65][66]. These templates provide additional insertion paths, enhancing the seed distribution for larger prostate glands. In addition, there is growing interest in robot-assisted brachytherapy, which can improve precision by automating needle insertion and seed placement. Although robotic systems [67] may eventually replace the need for rigid templates, ongoing research is needed to determine whether a mean error of 0.79 mm ± 0.32 mm needle targeting precision in a phantom offered by robotic systems has a significant clinical impact as compared to manual implantation [68]. Patient preference and acceptance of robotic procedures still remains an area to investigate [69][70][71].

Despite the benefits of rigid templates, they still face limitations, especially in larger prostates or when navigating complex anatomical structures such as the bladder neck. The template fixed grid system does not allow oblique needle trajectories; therefore, it cannot always navigate more complex insertion paths to avoid critical anatomical structures. Although advancements have been made in other areas of LDR-PB, there has been relatively little innovation in the design of rigid templates.

Part 1 of this study investigated quality improvement to patient dosimetry by the use of a custom-designed, in-house template incorporating oblique needle placement. This non-conventional template, designed with an angular degree of needle freedom, can improve implant quality by minimising the dose to OAR. It could also facilitate better access to the target volume in patients with pubic arch interference, as shown in Figure 1.4. Strassmann et al. also demonstrated the degree of freedom achieved through robotic oblique needle insertion [72].

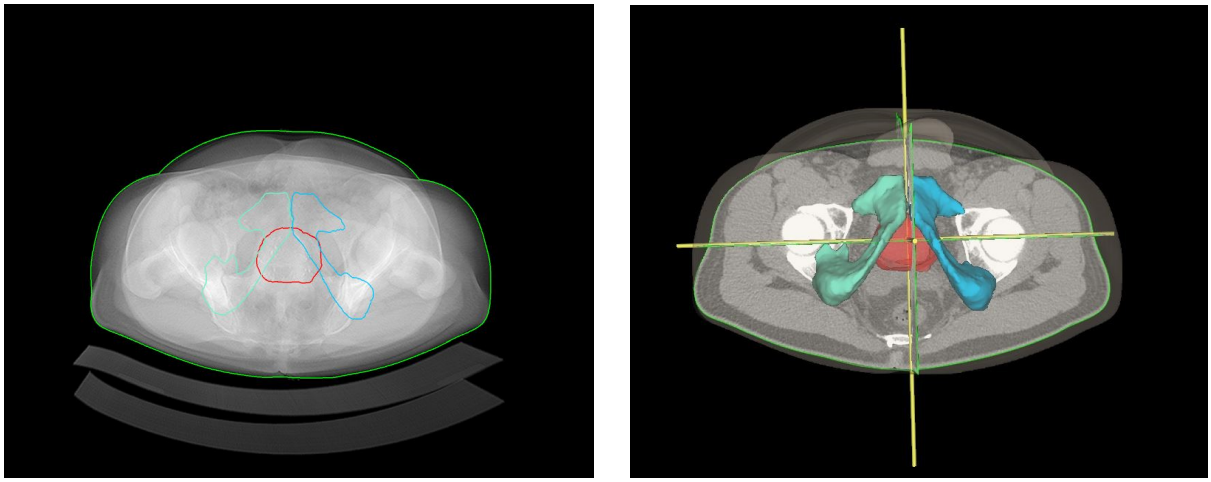

Figure 1.4: Patient image with the prostate volume of $65\,\mathrm{cm}^3$ showing pubic arch interference, leading to limitation in optimal positioning of radioactive sources.

1.3.2 Seed Strength Verification

Verification of seed strength in LDR-PB is essential to ensure accurate dose delivery. Historically, discrepancies between manufacturers' stated seed activity and actual strengths have been reported, often due to manufacturing malfunctions, contamination with impurities or human errors, which posed risks of under- or over-dosing because of inadequate quality of production [73]. In response, regulatory bodies such as the AAPM and the United States Nuclear Regulatory Commission (NRC) introduced stricter guidelines for seed strength verification, to be performed by medical physicists in medical facilities, as outlined in TG-43U and TG-56 reports [54][57].

Manufacturers now send sample seeds to primary standards laboratories such as the Physikalisch-Technische Bundesanstalt (PTB) in Germany for precise calibration using free-air ionisation chambers. These calibrated seeds are then used by secondary standards laboratories and manufacturers to calibrate their equipment and, ensure traceability and accuracy [74].

Clinically, well-type ionisation chambers are used to verify the strength of the seed by comparing the measured activity with the values of the manufacturer's seed certificate. To maintain sterility, clinics often order extra seeds from the same batch for verification, thereby avoiding problems with sterilisation after testing. AAPM recommends that at least 10% of the seeds be verified before implantation to ensure consistency with the stated activity of the manufacturer[57]. The air kerma strength S_k is calculated using:

$$S_k = M \cdot N_k \cdot K_P \tag{1.3}$$

where M is the measured chamber reading, N_k is the chamber calibration coefficient and K_P is the temperature/pressure coefficient.

Past errors underscore the need for stringent quality control at manufacturing and clinical levels to ensure that the prescribed dose matches the total seed strength. The introduction of the Nucletron FIRST system was a notable advancement in automated seed verification [75]. However, there has been limited progress in advancing technology and integration with intraoperative real-time prostate brachytherapy [74]. This might be due to the relatively low reimbursement rates associated with LDR-PB. However, such a system would optimise clinical workflows and reduce human errors.

1.3.3 Seeds logistics and strands

Another challenge in LDR-PB is ensuring the real-time accountability of radioactive seeds, documenting stranded seed patterns, and managing the logistics of implanted seeds.

Strict adherence to sterile conditions during seed handling is important to avoid source contamination [76]. Additionally, there is a high risk of seed loss and radiation exposure among hospital staff members. As a result, many clinicians prefer to perform seed strength accountability post-implant when sterile conditions are not a limitation. To address these challenges, the implementation of a feature on the Bard-QuickLink™ Loader that allows for intraoperative seed logistics accounting during the implant procedure was proposed.

Commonly used handling systems for LDR-PB include the QuickLink™ Loader from Bard Medical (Bard Medical Division, Covington, GA, USA) and the Eckert & Ziegler Medical (Berlin, Germany) [18][77]. These systems lack the functionality to account for the logistics of implanted materials. The goal of the work is to streamline the treatment workflow by minimising the influence of human factors that may introduce additional stress to brachytherapy clinicians during the procedure. The clinic in this study employs the QuickLink™ Loader device for seed strand configuration. For the feasibility study, a TOSHIBA CCD linear image sensor was incorporated into the Bard QuickLink™ Loader.

2. Material and Methods

This section describes the methods and procedures used to evaluate the feasibility of integrating a linear image sensor into the QuickLink™ Delivery System for handling seeds and connectors during intraoperative LDR-PB [78], along with the in-house custom-designed template aimed at addressing the aforementioned challenges. The methodology is divided into three parts, each addressing key aspects of the study. Part 1 details the custom-designed in-house prostate perineal needle template and the phantom test setup. Part 2 focuses on seed strength verification, while Part 3 covers seed logistics and strand lengths. All radiation protection measures were implemented in accordance with the German Radiation Protection Act and Ordinance, adhering to the ALARA principle to ensure minimal radiation exposure [79].

2.1 Part 1: Template

One of the primary objectives of brachytherapy treatment is to reduce the risk of toxicity to the genitourinary system while optimally delivering the prescribed dose to the tumour volume, thus enhancing the probability of effective tumour control and improving the patient's quality of life. The GEC-ESTRO guidelines recommend dosimetric constraints to limit toxicity levels [58].

2.1.1 Patient Data

This section is based on retrospective re-planning of previously treated intraoperative LDR-PB plans of 34 patients. These patients were treated with a prescription dose of 160 Gy delivered using I-125 seeds with activities ranging from 0.460 to 0.595 mCi. The mean prostate volume was 30.24 cm^3, with a range of 17.5 cm^3 to 65.38 cm^3. The mean urethral and rectal volumes were 1.36 cm^3 and 5.56 cm^3, respectively. Patients were treated between March 2017 and February 2019. The Retrospective planning was performed using the Varian VariSeed™ TPS [80]. For consistency, the dosimetric constraints (Table 2.1 [58])

applied in this study were identical to those used in the original intraoperative planning. Similar to the other studies in this thesis, the Ethics Committee of Mannheim University [2018-870R-MA] approved retrospective studies using patients' LDR-PB plans.

Organ	Parameter	Description
Prostate	P_D90	Minimum dose received by 90% of the prostate volume should be greater than 90% of the prescribed dose
	P_V100	Prostate volume receiving 100% of the prescribed dose should be greater than 95%
	P_V150	Prostate volume getting 150% of prescribed dose should be between 45% and 65%
Urethra	U_D10	Dose to 10% of urethra should be less than 150% of the prescribed dose
	U_D30	Dose to 30% of urethra should be less than 130% of the prescribed dose
Rectum	R_D2cm^3	Dose to 2cm^3 of rectum should be less than 145 Gy
	R_D0.1cm^3	Dose to 0.1cm^3 of rectum should be less than 200 Gy
	R_V100	Rectum volume getting 100% of prescribed dose (Reporting parameter)

Table 2.1: GEC-ESTRO recommended parameters for low-dose-rate prostate brachytherapy.

A copy of each patient's treated intraoperative plan (IntraOp) was generated and renamed to reflect the insertion of oblique inner needles planning (ObInp). In these retrospective plans, only the inner needles and seeds were manually planned using oblique trajectories. The inner needles are of particular interest because of their dosimetric effect on the bladder neck, urethra, and rectum [81]. The dosimetric parameters for each patient were analysed and compared between intraoperative and retrospective treatment plans. This compares the effect of using the rigid conventional template and the in-house design oblique template on dose metrics. Finally, the prototype rigid oblique template was tested on a phantom (see Figure 2.6) to evaluate its potential applicability in clinical settings. All data were analysed using MATLAB® and Microsoft Excel®.

2.1.2 Template Design

The custom-made template was constructed of polyoxymethylene (POM). POM was selected because of its known mechanical properties and low coefficient of friction μ, which ranges from 0.1 to 0.25 [82]. This low friction minimises resistance during needle insertion, ensuring smoother needle insertion and seed placement. Figure 2.3 illustrates the custom-designed template with an inserted 18-gauge needle positioned at grid hole D3.5 at an oblique angle of 30°. Additionally, POM's compatibility with various sterilization methods, particularly autoclaving, makes the template reusable. As shown in Figure 2.4, the template is designed to be easily disassembled, making it efficient for the sterilisation process. The components of the template, shown in Figure 2.2, were machined from cubic blocks of POM [83]. Similar to the conventional rigid template in Figure 2.1, it features a matrix of grid holes spaced 5 mm apart, with nine additional specialised holes allowing for oblique needle insertion.

The incorporation of nine oblique needle insertions was based on a statistical evaluation of the treated patient data, which indicated that the number of inner needles used ranged from three to nine. Centrally positioned oblique needle insertion further facilitates single-seed deposition at various angles (±30°) within the prostate apex, enhancing flexibility in the dose distribution. The design aims to optimise the target coverage. These nine chambers contained spherical structures, each with a central drilled hole, enabling insertion angles that are not achievable with the conventional template. The holes are designed to accommodate 18-gauge needles. Needle orientation and oblique insertion were achieved by rotating the spheres with the needle inserted, allowing adjustment to the desired oblique direction. The spheres were positioned to align with the parallel grid holes and securely held by the template front-end plate. The back-end plate was assembled with the front-end plate to ensure that the spheres were held in place. To further maintain stability and prevent unintended rotation, the template was secured at its four corners using screws.

The design offers greater adaptability, particularly in patients with larger prostate volumes or pubic arch interference, where conventional parallel-needle insertion techniques may be inadequate. This design allows for better coverage in challenging anatomical scenarios. The proposed approach builds on and refines the conventional parallel needle technique by adopting a hybrid method that integrates both parallel and oblique insertions, improving the dose distribution in the prostate while reducing the dose to the OARs. Figure 2.5

shows the schematic drawing of the template. Without the two metal footings, each with a height of 19.2 mm, the template body has a height of 85.5 mm and a width of 80 mm. Refer to Figure 2.5 for a detailed view of the template's dimensions.

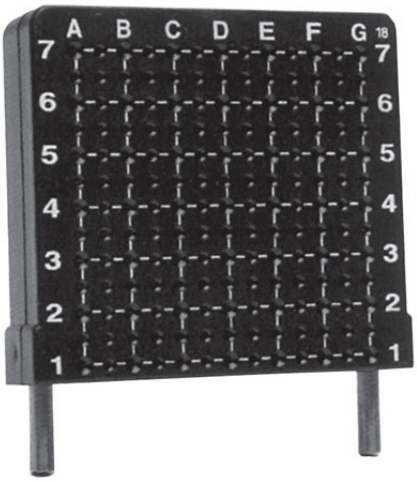

Figure 2.1: Mick® Brachytherapy Template [84]

As shown in Figure 2.2, the grid coordinates, marked with alphanumeric labels, are located along the periphery: letters (A–G) represent the horizontal axis, and numbers (1–7) represent the vertical axis. As with the conventional template, these coordinates align with the digital grid of the TPS and the digital grid of the TRUS system for 18-gauge needles. Additionally, clinicians can use column D on the template to align the prostate laterally, ensuring the urethra is centred.

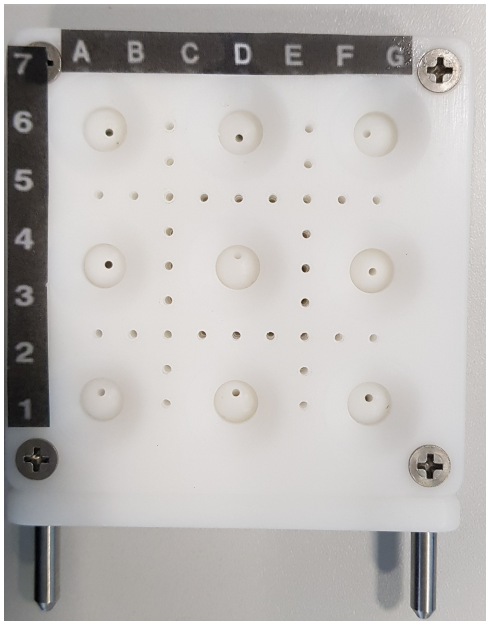

Figure 2.2: Illustrates the front view of custom design template, showing key structural elements (parallel and oblique insertions).

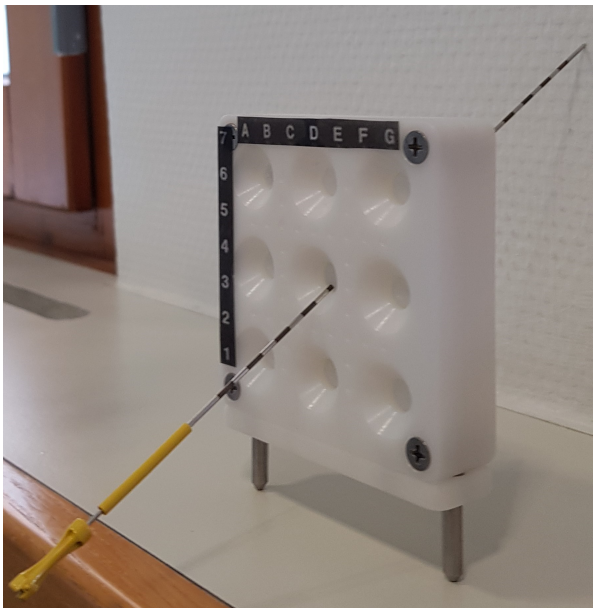

Figure 2.3: Shows the custom design template featuring oblique needle insertion at a 30°angle at insertion hole D3.5.

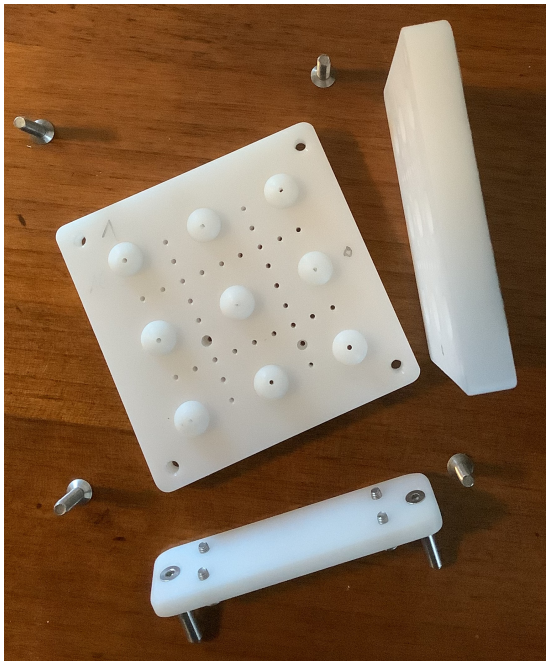

Figure 2.4: Illustrates the disassembled custom design template to show the various parts, facilitating efficient template sterilisation.

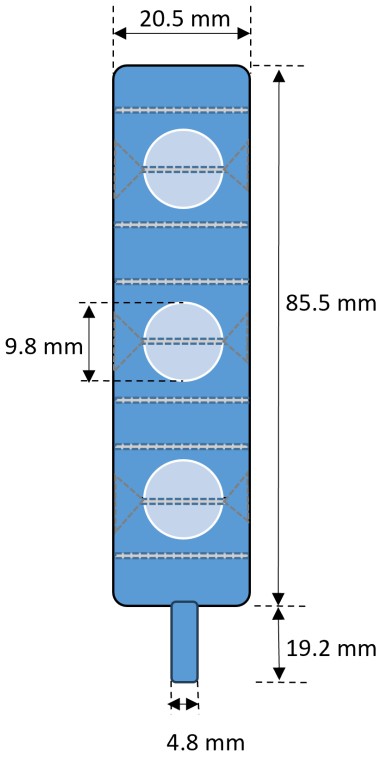

Figure 2.5: Shows the custom design template with annotated dimensions.

To increase the oblique angle of insertion, the entrance and exit areas around the nine oblique grid holes are bevelled, allowing angles of ±30°. The ±30° range was selected as it represented the maximum angle range that still allowed sufficient clearance for rigid needle insertion between the oblique bevelled grid holes. These nine specialised grid holes, which support oblique insertion, enhance adaptability for various prostate shapes and sizes and are particularly helpful for navigating around anatomical obstructions such as the pubic arch (Figure 1.4). Finally, at both horizontal ends of the template are the two metal footings designed for mounting on the stepper.

2.1.3 Planning Procedure

After creating a copy of the original treatment plan, the peripheral needles and seeds remained unchanged, and the seed strength was maintained according to the intraoperative treatment. However, the inner seeds were unlinked and replanned. The inner needles' insertion points must be changed to incorporate oblique needle orientation into the TPS. However, changing the insertion points also changes the position of the seeds. Therefore, to maintain the location of the seed, a curvature tool was used to manipulate the orientation of the inner seeds (Figure 2.7 and Figure 2.8), which then reflects the needed oblique insertion.

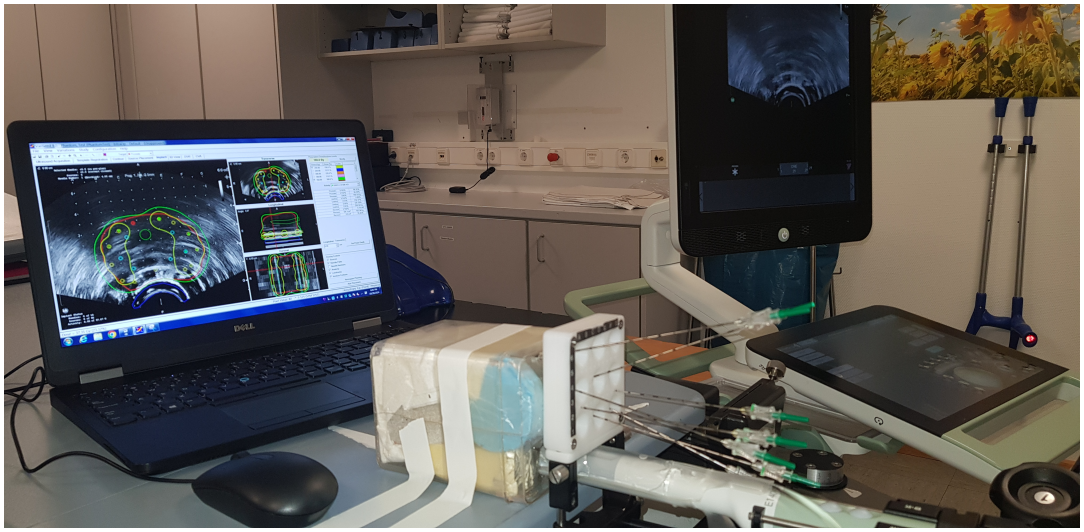

Figure 2.6: Phantom-based ultrasound guided intraoperative setup (Phantom prostate size 65.02 cm^3) with phantom on the treatment couch, with already inserted needles. Behind the phantom is the TPS notebook.

The total number of inner seeds was not altered. Instead, their trajectories were adjusted to achieve oblique placement without changing the actual insertion point of the needles. To evaluate the practicability of the novel physical template in real-world settings, a prostate phantom was developed and used for phantom-based intraoperative procedures. The size of the phantom prostate was 65.02 cm^3. Figure 2.6 shows the setup based on a phantom of the intraoperative procedure.

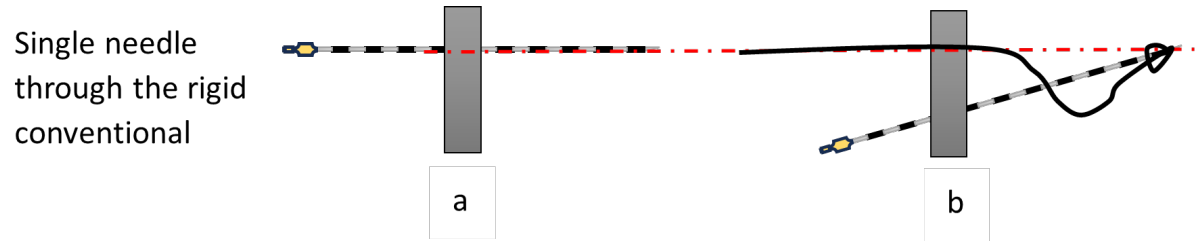

Figure 2.7: Figure (a) simulates the needle parallel path through the physical template. This is also represented so in the TPS. Figure (b) shows a sketch of the in-house design template with oblique needle insertion. In order not to change the position of the needle, the needle within the prostate is deformed to mimic the oblique entry, which allows seed deposition at the desired angle, as indicated by the curved arrow in Figure (b).

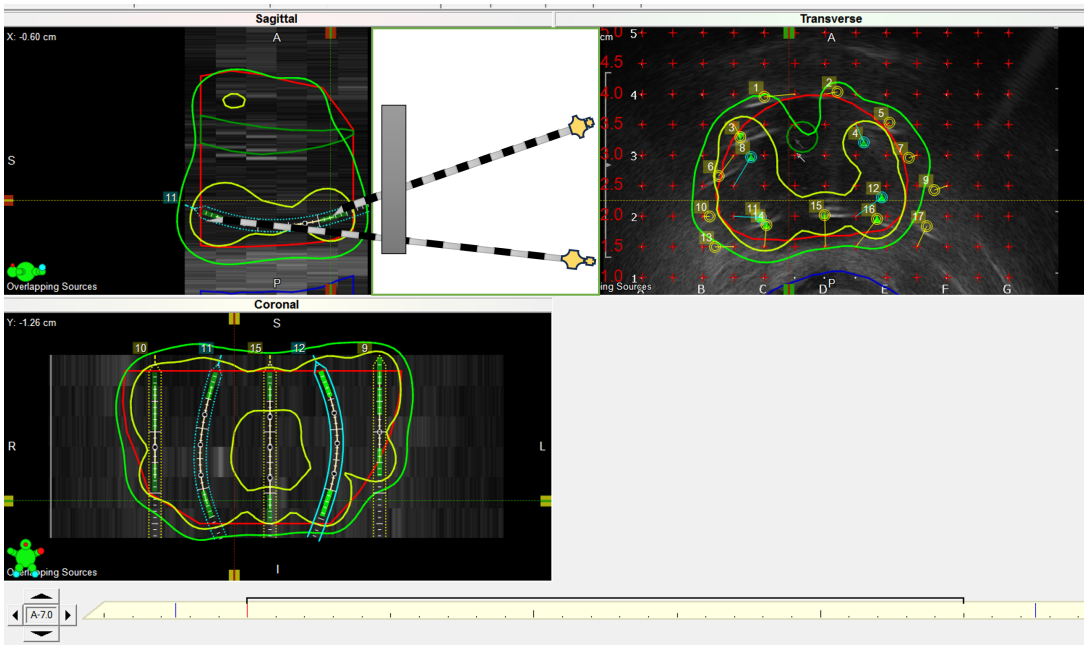

Figure 2.8: Illustrates the un-linking of the inner seeds and provides a visual representation of the angle achieved through oblique insertion, facilitated by the proposed physical template design.

Figure 2.9 demonstrates the concept that the in-house design template provides. With the needle trajectory, the seeds are brought to an orientation in which the surface of the OARs exposed to high doses is minimized [81].

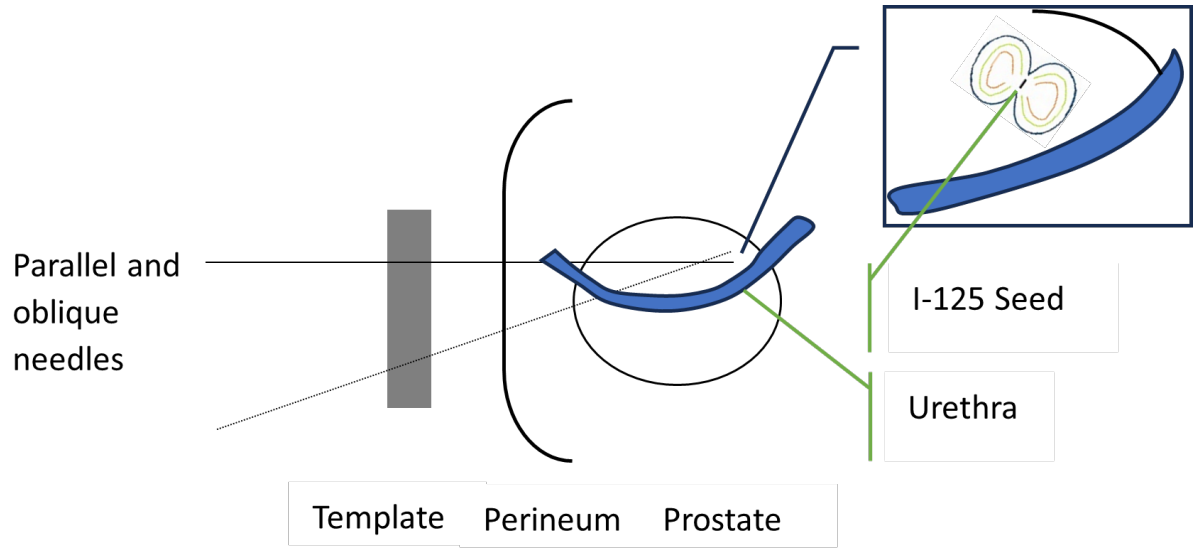

Figure 2.9: Parallel and oblique needle insertions through a physical template, highlighting the potential of oblique needles to provide a more favourable orientation for inner seed deposition that minimises the dose to the urethra.

2.1.4 Application in Phantom

The phantom used in this part of the study was based on the CIRS Model 053 prostate phantom [85], which was designed to evaluate the functionality of the custom-designed template (Figure 2.10). The inner dimensions of the plastic container were 95.95 mm × 95.95 mm × 132.88 mm. To simulate the surrounding tissue, the space remaining in the container was filled with bolus tissue-equivalent material. Styrofoam sheets with a thickness of 20 mm were used to secure a 10 mm thick rectum wall made of bulus material, on which a 65.02 cm^3 lean meat sample simulated prostate tissue. The volume was measured using the water displacement method. A 50 mm segment of a Foley catheter shaft was used to model the urethra, which was inserted into a 10 mm wide channel at the centre of the lean meat.

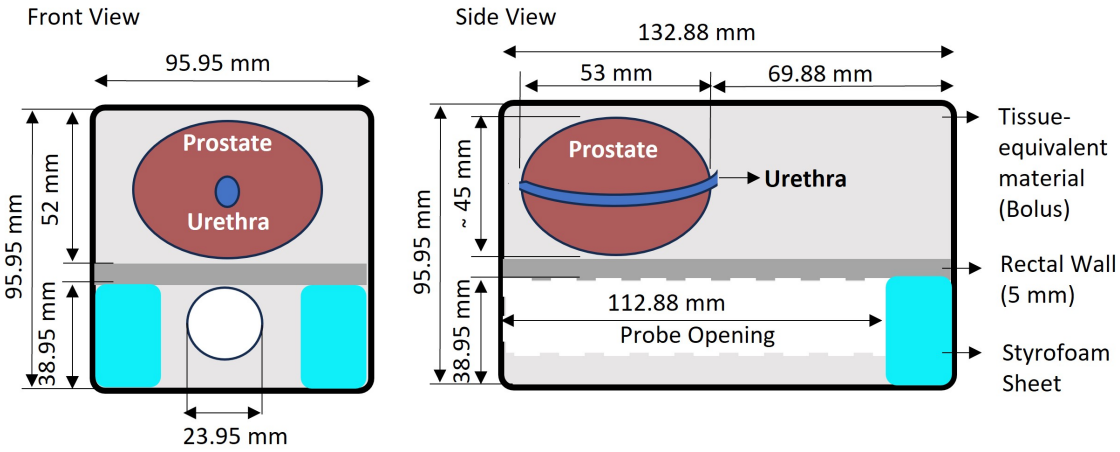

Figure 2.10: Figure illustrates prostate phantom design and dimension. The phantom was used to test the functionality of the custom-designed template.

A treatment plan was generated using the VariSeed™ nomogram planning, followed by manual optimisation of needle orientation through forward planning. Oblique inner needles were inserted under longitudinal TRUS guidance. After identifying the insertion coordinates of the oblique needles on the template, the needles were inserted under TRUS guidance in the longitudinal plane. Their obliqueness was then manually adapted in the TPS to align with their visualisation on TRUS, and the prostate dose coverage was subsequently updated accordingly.

2.2 Part 2: Seed Strength Verification

LDR-PB is based on a multidisciplinary team to ensure the safe and effective implantation of radioactive seeds [86] into the patient‘s prostate. To reduce operator dependency and improve workflow, it is essential to optimise specific tasks, allowing clinicians to focus on critical aspects of the therapy [23]. Since 2002, over 300 patients at Ortenau Klinikum Offenburg-Kehl have undergone LDR-PB, and the team adopted the intraoperative planning technique in 2016. One major challenge is the verification of the strength of seeds, which must be performed under sterile conditions a day before the implant, making the process not only time-consuming but also involves the risk of contamination and radiation exposure. The objective of this section was to demonstrate the use of a linear CCD sensor to measure seed strength and assess the feasibil-

ity of integrating the sensor into the loader system for in-situ seed strength verification during the implant procedure.

Although several pre-implantation seed strength assay methods exist [76][75], intraoperative verification of all seeds used for clinical treatment remains unaddressed. This study proposes enhancing the QuickLink™ Loader to enable real-time seed verification during intraoperative implantation, which would streamline the procedure workflow. Previous approaches, such as those of Lee et al. [87], focused on batch verification outside the operating room. Real-time intraoperative seed verification during the procedure with a CCD line sensor is a significant advancement in the field of brachytherapy. To the best of current knowledge, this study appears to be the first investigation into the use of a line camera for seed strength verification. This section describes the materials and methods used to implement and evaluate the proposed enhancement of the loader.

2.2.1 Background

The Bard QuickLink™ Loader is a mechanical device designed to configure prostate brachytherapy seed strands. This project component evaluates seed strength measurement using a compact line sensor camera, highlighting its potential to enhance the functionality of the loader system by enabling real-time strength measurement of I-125 seeds during intraoperative procedures.

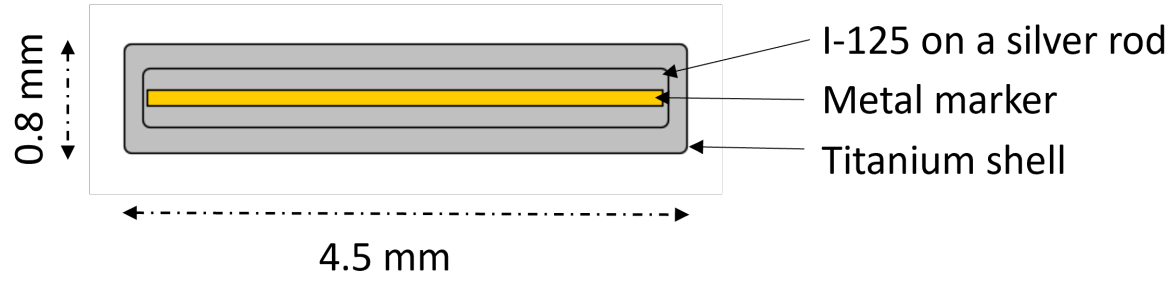

Figure 2.11: Iodine-125 model STM1251 for prostate implant, the metal core improves seed visibility under X-ray or CT used for post-planning dosimetry.

In clinical practice, the STM 1251 I-125 seed model supplied by Bard Medical was utilized by the department [88]. This model consists of adsorbed I-125 on a silver rod encapsulated in a titanium shell (see Figure 2.11). The patient-specific seed package was accompanied by a source certificate and a decay factor

table, which were used to calculate the actual activity. Figure 2.12 provides an indication of the frequency of various I-125 seed activities used in the clinical department in this study between January 2016 and February 2024.

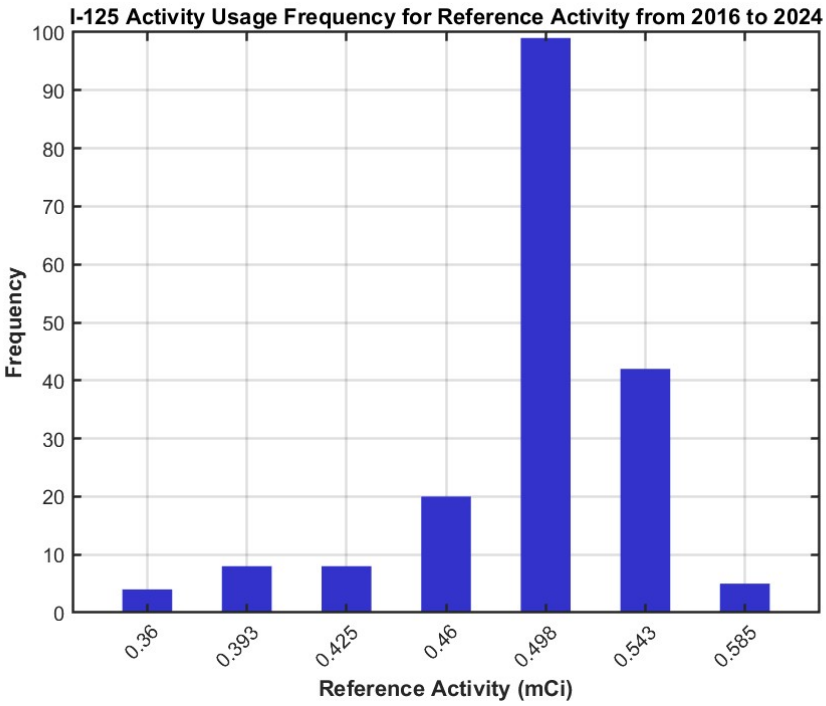

Figure 2.12: The frequency of reference activity usage for implants from January 2016 to February 2024

In both this and the seed logistics and stands study in section 2.3, a Toshiba TCD1304 CCD monochrome linear image sensor was used, which features 3,648 linear pixels with a glass substrate cover. The TCD1304 sensor had a spectral response spanning 400 to 1100 nm, with a maximum sensitivity between 550 and 600 nm. Each pixel element measures 8 µm x 200 µm, with an 8 µm centre-to-centre spacing. The sensitive area of the sensor spans a width of 29.1 mm (as illustrated in Figure 2.13 [89]). The maximum data rate was 500 kHz per pixel, facilitating rapid data acquisition [89].

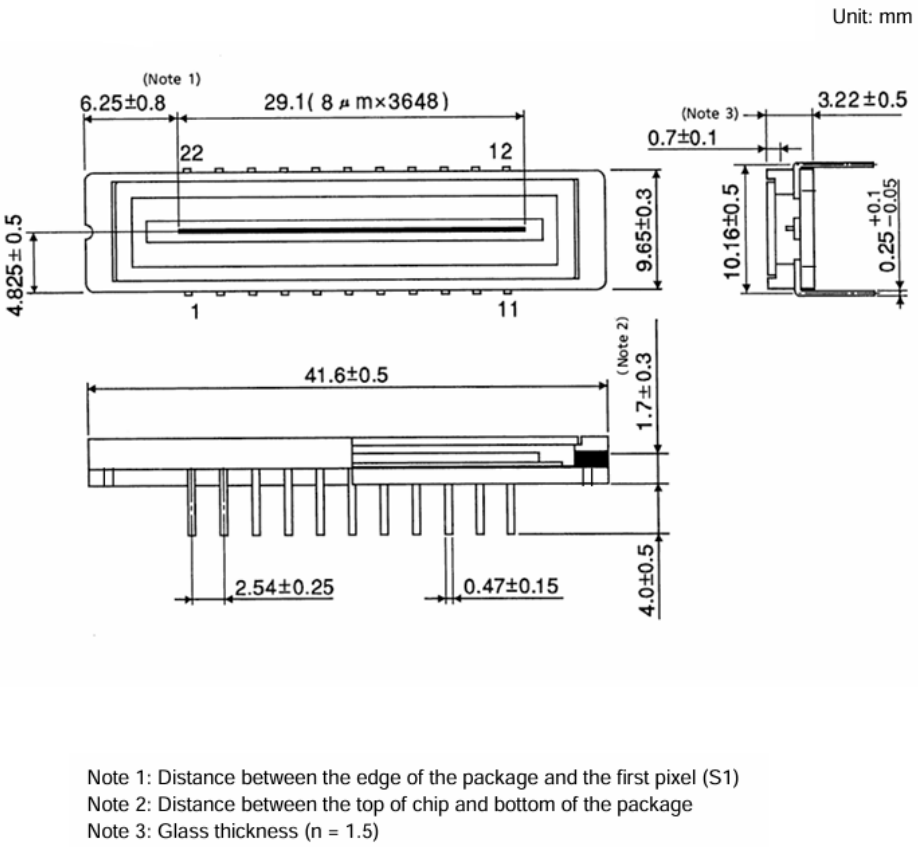

Figure 2.13: Schematic of the Toshiba TCD1304 CCD monochrome linear image sensor (taken from the datasheet) highlighting its dimensions and features.

To drive the linear CCD sensor, a programmed STM32F401CCU6 microcontroller was employed, in combination with a Raspberry Pi 4B Starter Kit featuring 4 GB RAM and a 4-core 1.5 GHz processor. The sensor was used to capture radiation, both directly and indirectly, via an EJ-200 (Eljen Technology Inc., Sweetwater, TX) scintillator. For direct measurements, the radioactive seed was placed on the sensor using a 3D printed collimator (see Figures 2.14 and 2.15). In the context of the entire study, Polyterra material was employed for all 3D printing performed with CraftBot Flow IDEX 3D printer and PLA filament. Four collimators with different rectangular aperture sizes were 3D printed. The aperture dimensions were as follows: 5.5 mm × 1.8 mm, 15.5 mm × 1.8 mm, 20.5 mm × 1.8 mm, and 25.5 mm × 1.8 mm. For indirect measurements, the radioactive seed was placed on the EJ-200 scintillator, which was firmly attached to the sensor using the same collimator.

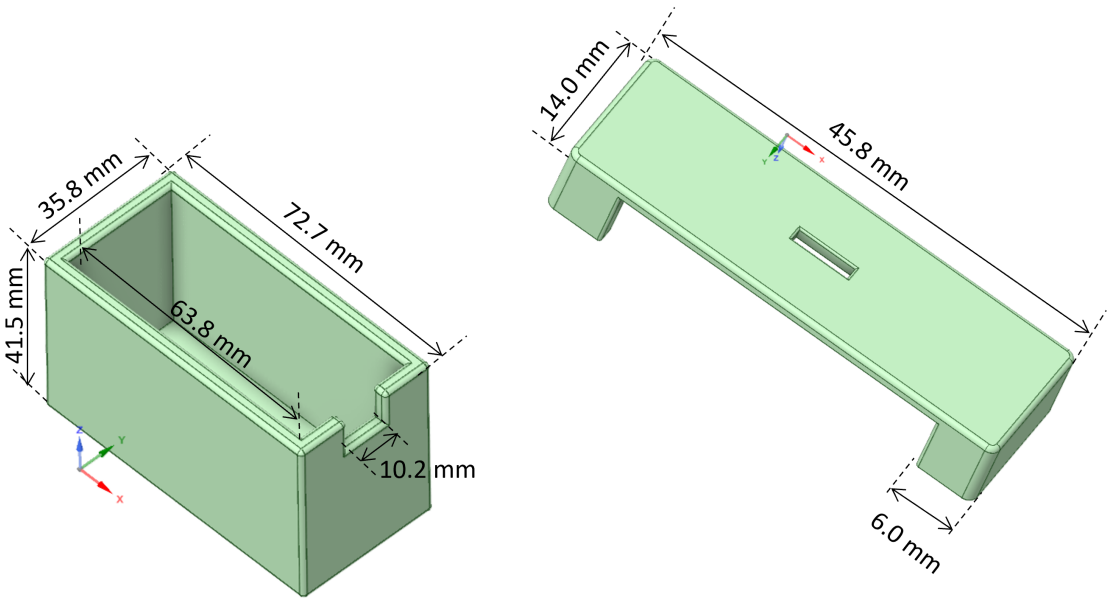

Figure 2.14: The design of the 3D printed light tight cover and the collimator to position a single seed at the centre of the detector.

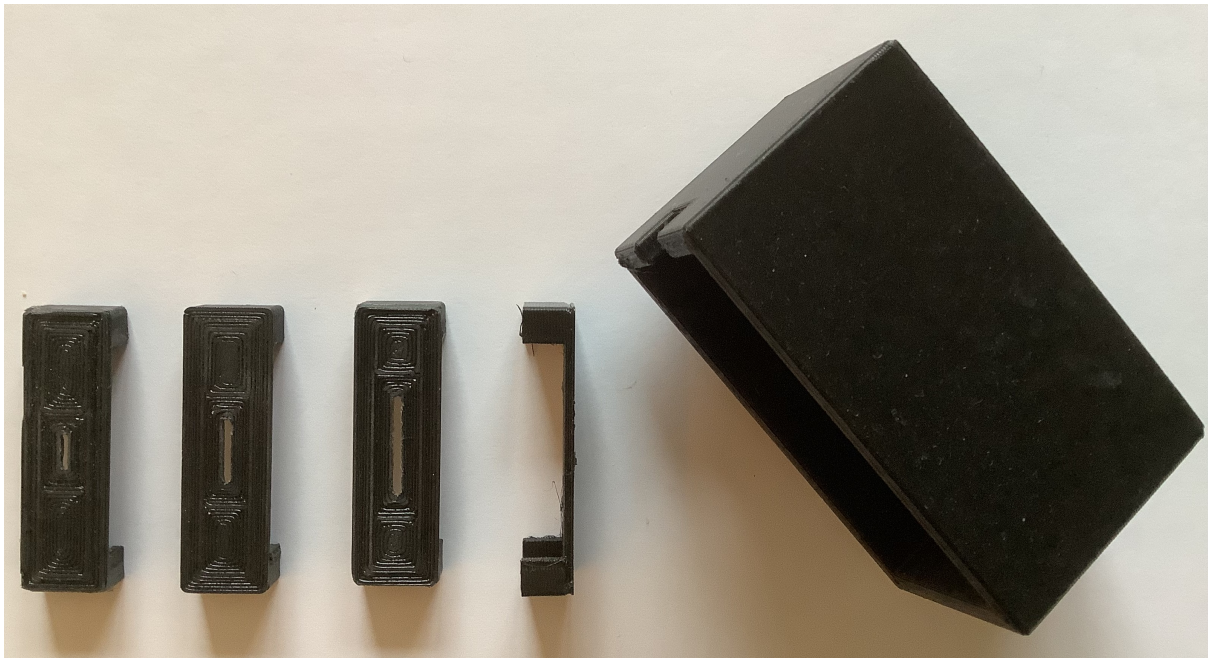

Figure 2.15: Image of 3D printed collimators with rectangular aperture sizes of 5.5 mm × 1.8 mm, 15.5 mm × 1.8 mm, 20.5 mm × 1.8 mm, and 25.5 mm × 1.8 mm along side with the ligth-tight cover.

The EJ-200 scintillator, provided by Scionix Holland B.V., can convert gamma radiation into visible light, which can be detected by the CCD sensor. The scintillator's peak emission wavelength is approximately 425 nm, and although it is not perfectly aligned with the CCD's peak sensitivity, it is still within the detection range of the sensor [90]. The pairing of the CCD sensor with the EJ-200 scintillator enables the conversion of gamma rays into visible light that can be detected by the CCD.

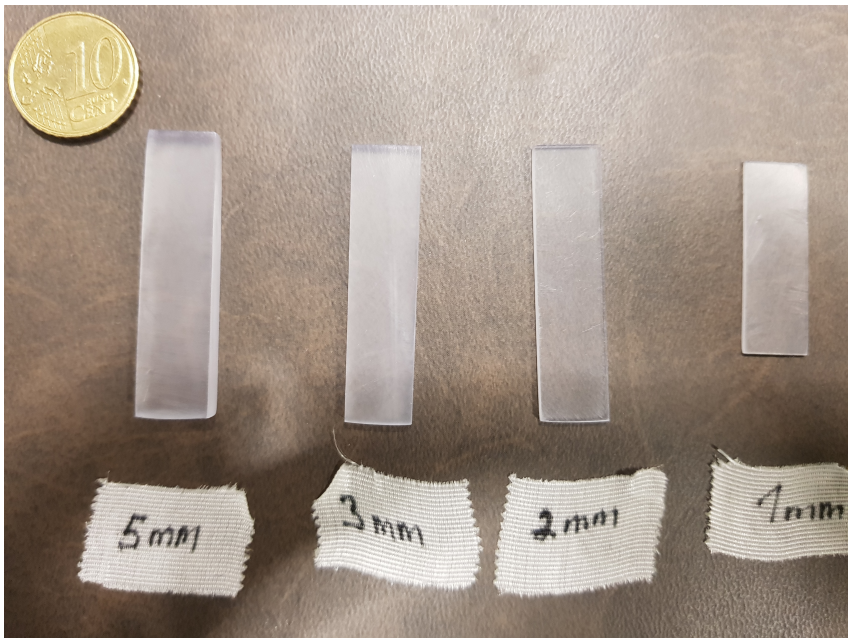

Figure 2.16: EJ200 scintillator samples were prepared in varying thicknesses of 1 mm, 2 mm, 3 mm, and 5 mm to investigate the optimal thickness for scintillation efficiency.

While the EJ-200 scintillator was not ideal for this application, it was the only scintillator available for this study. The ideal scintillator would have been Cesium (Cs) Iodide (I) doped with Thallium (Tl) (CsI(Tl)), which emits light at approximately 540 nm, closer to the peak sensitivity of TCD1304 [91]. To determine the optimal scintillator thickness, several samples were prepared, each with thicknesses of 1 mm, 2 mm, 3 mm, and 5 mm (as shown in Figure 2.16). These samples were manually cut using a precision band saw with a fine-toothed blade to minimise material loss and preserve structural integrity. The thicknesses were verified with Alpha Tools digital calliper (model number 20497503). The calliper's specified accuracy for measurements below 100 mm is ±0.02 mm. Considering both systematic and random uncertainties, the total

uncertainty in verifying measurements using the calliper was determined to be ±0.038 mm.

Firstly, the signal output was measured with and without the EJ-200 scintillator to evaluate the difference in signal output, with the expectation that the setup with the scintillator would yield a higher output compared to the setup without it. A specially designed 3D-printed light-tight cover was used to prevent interference with ambient light during the measurements (Figures 2.14 and 2.15). The background noise from the set-up was measured 3 times to characterise the background noise in the absence of a radioactive source. Before proceeding with the experiment, the number of photons expected to reach the detector surface was manually calculated. The reason was to validate the output of the system and to help identify errors in setup.

2.2.2 Photon estimation and optimal total frame time calculation

Assuming that the I-125 seed, whose activity is to be measured by placing it on the sensor, has an activity of 0.464 mCi, the number of photons emitted per second can be calculated by converting the activity to becquerels [92]. This means that the number of disintegrations per second for the 0.464 mCi radioactive seed is approximately 1.72×10^7 photons per second (refer to the Appendix for the calculation).

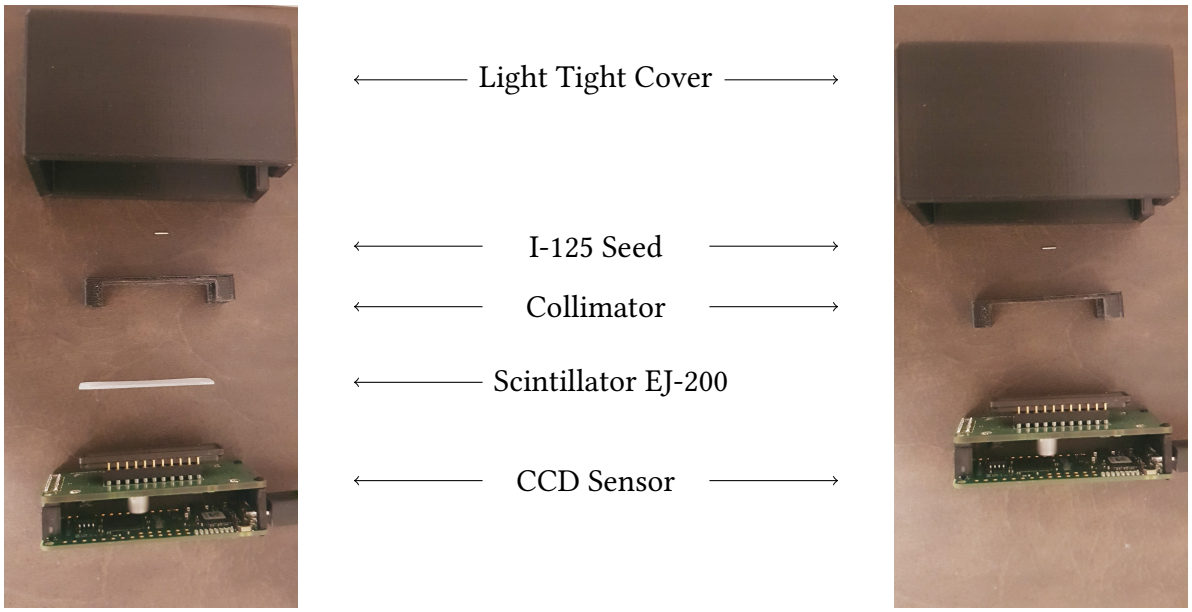

Figure 2.17: Measurement setup: On the left for setup involving the EJ-200 scintillator and on the right without the EJ-200. The collimator holds the seed on the detector, and the light-tight cover is placed over the probe.

Figure 2.17 illustrates the experimental setup. The transmission through the 0.7 mm glass cover of the CCD camera, which protects sensitive elements, was accounted for by calculating the linear attenuation coefficient for photon energies in the 27-35 keV range [93]. The transmission rate was found to be 90%. Finally, considering minimal scattering and absorption beyond the glass cover, along with the geometric factor, the quantum efficiency of the TCD1304 CCD sensor was estimated to be approximately 10% [94], the number of photons reaching the detector was estimated to be approximately 58,405 photons per second. The detailed calculations are provided in the Appendix for reference. Considering the number of photons that would reach the detector, data were collected over measurement durations of 10, 15, 20, and 30 seconds. Three measurements were recorded for each of the mentioned durations with moving average filter window sizes of 5, 45 and 99. In all the studies involving the use of the TCD1304 sensor in this work, data acquisition was performed by recording every second frame, effectively reducing the temporal resolution while minimizing the data volume and computational load.

For optimal measurements, improved SNR, and manageable data throughput, a 30 Hz frame rate with an exposure time of 26 ms and a read-out time of 7.3 ms was used (total time per frame = 33.3 ms). This provided a better

signal quality and improved the SNR. A higher frame rate of 60 Hz allows for more dynamic measurements with an exposure time of 9.4 ms but reduces detector sensitivity and SNR and increases background noise (calculation in the Appendix). Following the measurements of single seeds, measurements were conducted for a Seed_space_seed strand. Measurements were performed at a standard room temperature (approximately 20°C to 25.7°C) and a pressure of 998.5 hPa.

The MATLAB® signal analysis tools were employed to process the batch data, beginning with wavelet denoising to smooth the raw data [95][96]. To further enhance the data quality because of excessive noise, a Savitzky-Golay filter was applied to the denoised signal [97].

Seed regions were identified using peak detection techniques. Gaussian and Lorentzian models were then fitted to confirm the seed location on the detector. The results were then plotted, and source strength results were displayed. The calculation incorporated the areas under the Lorentzian fit for various reference activities using MATLAB®'s linear fit model (as shown in Listing A.1 provided in the appendix). The experimental setup closely mirrored that used for seed logistics and strands in part 3, with the primary difference being the incorporation of a light-tight cover, as illustrated in Figures 2.18 and 2.17.

2.3 Part 3: Seed Logistics and Strands

In this section of the study, a TOSHIBA TCD1304 CCD monochrome linear image sensor featuring 3648 linear pixels with a glass substrate cover was used. The pixel element size was 8 µm by 200 µm on an 8 µm centre [89]. The sensitive area extends 29.1 mm wide, enabling precise measurement of the incident light intensity. The sensor's capability to accurately detect the contour of objects makes it suitable for measurements in this portion of the study. To drive the linear CCD sensor, a programmed STM32F401CCU6 microcontroller combined with a Raspberry Pi 4B starter kit with 4GB RAM and a 4 x 1.5 GHz processor was employed. The setup also included a 19" LG LCD Monitor [98]. Using the electronic shutter function of the CCD, the exposure time was precisely controlled. The resulting signals were transferred to the computer via a USB port for subsequent processing. For the construction of seed strands, the QuickLink™ Loader from Bard Medical was used, a widely used seed strand handling system.

In this part of the study, the proposed position for the second CCD sensor is at the centre of the assembly base, beneath the ruler. The lead glass door above the assembly base and ruler allows access to light, which is essential for the second sensor's operation [99].

2.3.1 Experimental Setup

The remaining implantation materials from previous I-125 seed implantation procedures were used for this investigation. For the first part of the study, elapsed I-125 sources with insignificant radioactive source strength were used. For the second part, I-125 seeds still containing measurable radiation were used. The schematic of the experimental setup is shown in Figure 2.18.

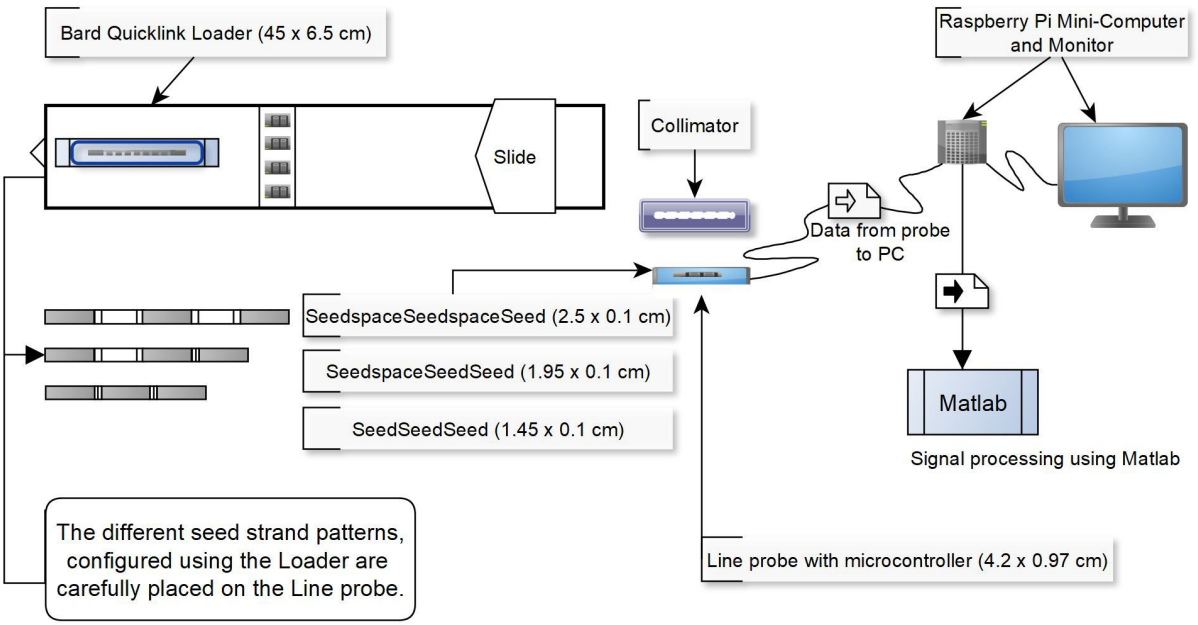

Figure 2.18: Schematic representation of the experimental setup illustrating the study's configuration with component dimensions specified in parentheses

A custom collimator was designed and fabricated using a 3D printer to prevent the seed from rolling over the detector. The collimator served to obscure the unused areas of the sensor and assist in positioning the seeds precisely in the centre of the sensor, as presented in Figure 2.19 and 2.15 of Subsection 2.2.1.

First, the effect of partial illumination from a single seed was examined. The signals of a single seed, with and without the collimator were measured. The

Figure 2.19: Collimator over the sensor probe and a seed strand on the central axis un-collimated part of the probe

second experiment focused on recognizing the stranded seed patterns. As illustrated in Figure 2.20, three seed patterns were considered for each batch of the reference activity: Seed-Space-Seed-Space-Seed, Seed-Seed-Seed, and Seed-Space-Seed-Seed. The lengths of the seed strands were manually calculated based on the manufacturer's specification [18][99].

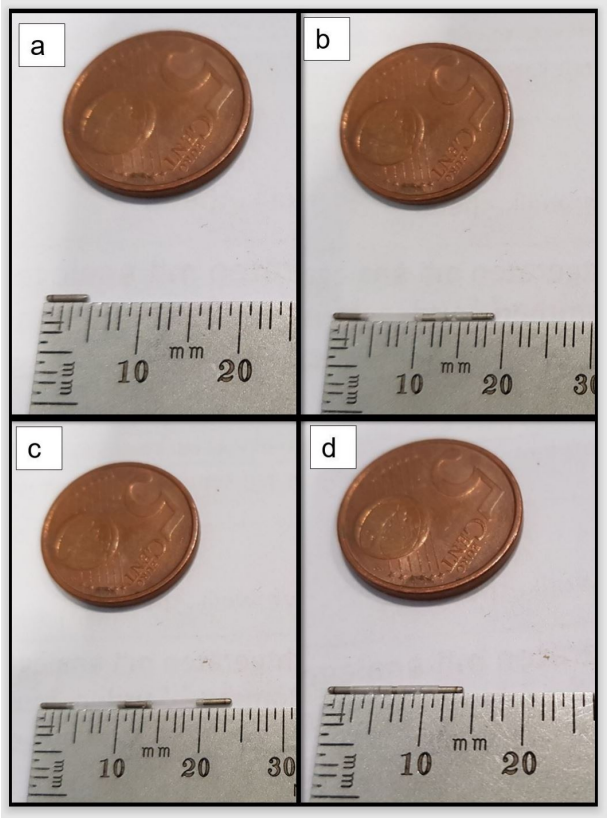

Figure 2.20: (a)Single seed,(b) Seed-Space-Seed-Seed strand, (c) Seed-Space-Seed-Space-Seed-Strand, (d) Seed-Seed-Seed strand

Standard Sourcelink™ connectors of 5.5 mm were used to build seed-to-space strands and 0.5 mm for Seed-to-Seed Sourcelink™ connectors. The study

involved three seed strand patterns to assess the sensor's ability to identify and document the seed strand pattern, accurately count the number of seeds, and evaluate the impact of seed strength on sensor output. To capture the data accurately, the exposure time of the photodiode array was set to 0.16 ms, and the frame time was adjusted to 105.19 ms under normal light conditions and average room temperature. The settings were determined following extensive testing of various exposure and frame time combinations. A short integration time was selected to prevent the line sensor from being overexposed. All data were collected and analysed using Microsoft Excel® for data entry and preliminary processing and MATLAB® for signal processing and visualization.

3. Results

3.1 Part 1: Template

With the prostate periphery needles of 34 patients left in place, the inner needles were manually replanned retrospectively to improve dosimetry through oblique deposition of inner seeds. As described in Subsection 2.1.3, these plans were created assuming that the physical in-house template guided the needle insertion. As shown in Table 3.1, the mean volumes of the prostate, rectum and urethra were 30.42 cm³, 5.56 cm³ and 1.36 cm³, respectively. The maximum prostate volume was 65.38 cm³. Table 3.2 compares the dosimetric parameter between the standard clinical plan (IntraOp) and the optimised plan with oblique needles (Obinp) for the patient with the maximum prostate volume in the data.

Parameter	IntraOp (Mean ± SD)	ObInp (Mean ± SD)	p-Value
Prostate Volume (PTV)	30.42 ± 11.58	-	-
V100 %	98.39 ± 0.69	99.31 ± 0.29	$p < 0.001$
V150 %	62.18 ± 5.31	59.17 ± 7.46	$p = 0.031$
D90	194.93 ± 5.31	194.63 ± 13.92	$p = 0.908$
Rectum Volume	5.56 ± 1.69	-	-
D0.1cm^3	164.55 ± 27.29	156.00 ± 25.17	$p = 0.002$
D2cm^3	98.03 ± 18.85	98.16 ± 20.47	$p = 0.958$
V100 %	5.49 ± 5.79	0.18 ± 0.17	$p < 0.001$
Urethra Volume	1.36 ± 0.79	-	-
D10	213.13 ± 9.81	205.45 ± 7.68	$p < 0.001$
D30	201.42 ± 7.33	195.60 ± 5.54	$p < 0.001$

Table 3.1: Statistic table of dosimetric parameters for intraoperative and retrospective oblique inner needles/seeds plan in condition with paired t-test results

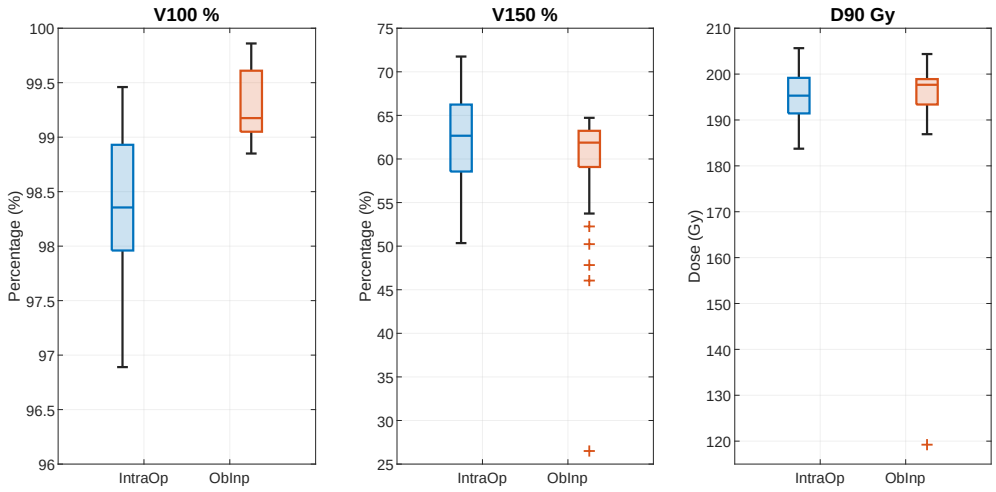

Figure 3.1: Boxplots comparing dosimetric parameters (V100%, V150%, and D90 Gy) between the intraoperative plan (IntraOp) in blue and the oblique inner needle plan (Oblnp) in red. The plots show the median, interquartile range, and the overall distribution of each parameter. The V100% and D90 Gy parameters showed higher median values for the Oblnp plan than for IntraOp, whereas V150% was lower for Oblnp with greater variability and more outliers in the low-dose range, indicating a reduction in high-dose regions.

Not only is the dose distribution to the prostate target volume improved by 1.9%, but the dose to organs at risk is notably minimised, with reductions of 20.32% and 11.89% in D0.1cm^3 and D2cm^3 for the rectum, respectively, and 4.24% and 2.88% in D10Gy and D30Gy for the urethra. This trend of enhanced dose distribution, coupled with minimised doses to OARs, was consistently observed across all patients. No correlations were observed between tissue volumes and dosimetric parameters. For each dosimetric constraint of the two sets of plans for all 34 patients, the mean, median, minimum, maximum, standard deviation, and the 25th and 75th percentile were calculated. The results for target volume (PTV prostate), urethra, and rectum are presented in Table A.1, A.2, and A.3 in the Appendix.

Parameter	Intraoperative (IntraOp)	Oblique needle plan (ObInp)	Units
Prostate Volume (PTV)	65.38	65.38	cm^3
V100 %	97.24	99.08	%
V150 %	62.38	63.00	%
D90	196.10	198.10	Gy
Rectum Volume	5.13	5.13	cm^3
D0.1cm^3	176.45	140.60	Gy
D2cm^3	122.21	107.68	Gy
V100 %	5.41	0.18	%
Urethra Volume	3.83	3.83	cm^3
D10	216.66	207.48	Gy
D30	206.99	201.03	Gy

Table 3.2: Comparison of dosimetric parameters for maximum prostate volume between parallel and oblique planning approaches for inner seeds placement.

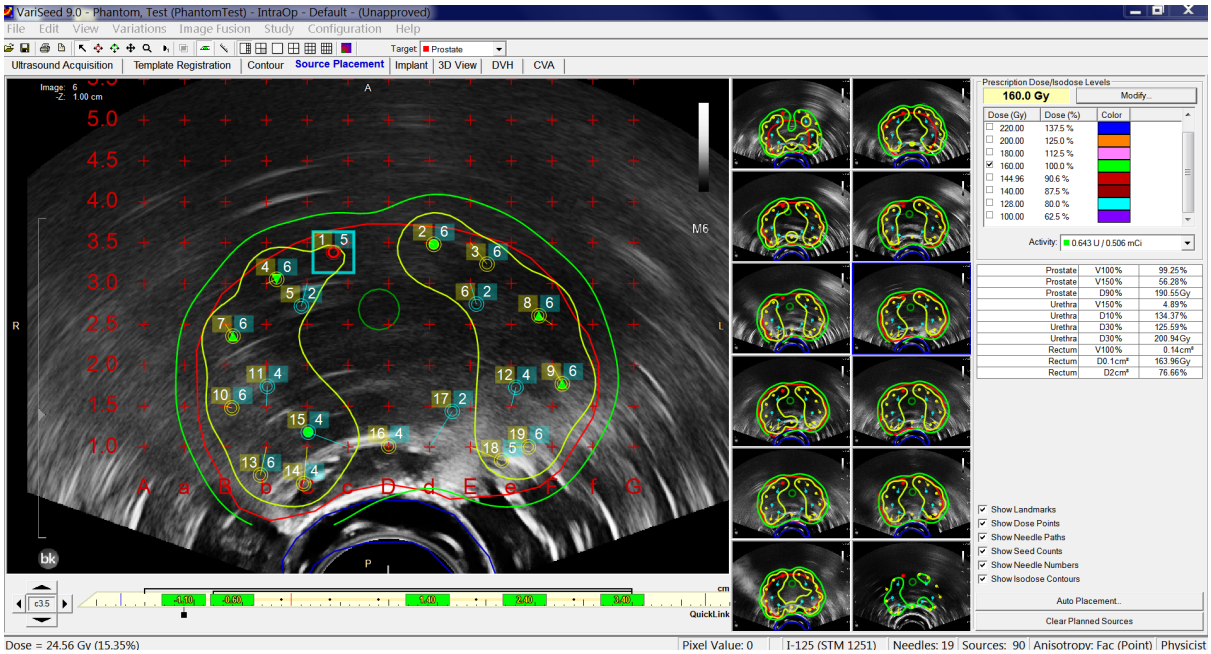

Figure 3.2: Treatment plan generated with the VariSeed® TPS, showing dose coverage (dosimetric parameter) on the right and the target volume dose coverage on the left. The green isodose line is the 95% of the prescribed dose of 160 Gy. The target structure is in red.

A paired t-test was performed to compare the dosimetric parameters between the intraoperative treatment plan and retrospective plan for the target volume, urethra, and rectum (Table 3.1). The results indicate that, apart from D2cm³ (the dose to 2 cm³ of the rectum) and D90 (the dose received by 90% of the prostate volume), which remained relatively consistent between the two plans, the proposed approach improved the remaining dosimetric parameters. Although D2cm³ did not show statistical significance, the dosimetric parameter for the

retrospective study for the large prostate volume (65.38 cm³) suggests that the oblique inner needle planning approach is particularly beneficial for larger prostate glands for this dosimetric parameter (see Figure 3.2).

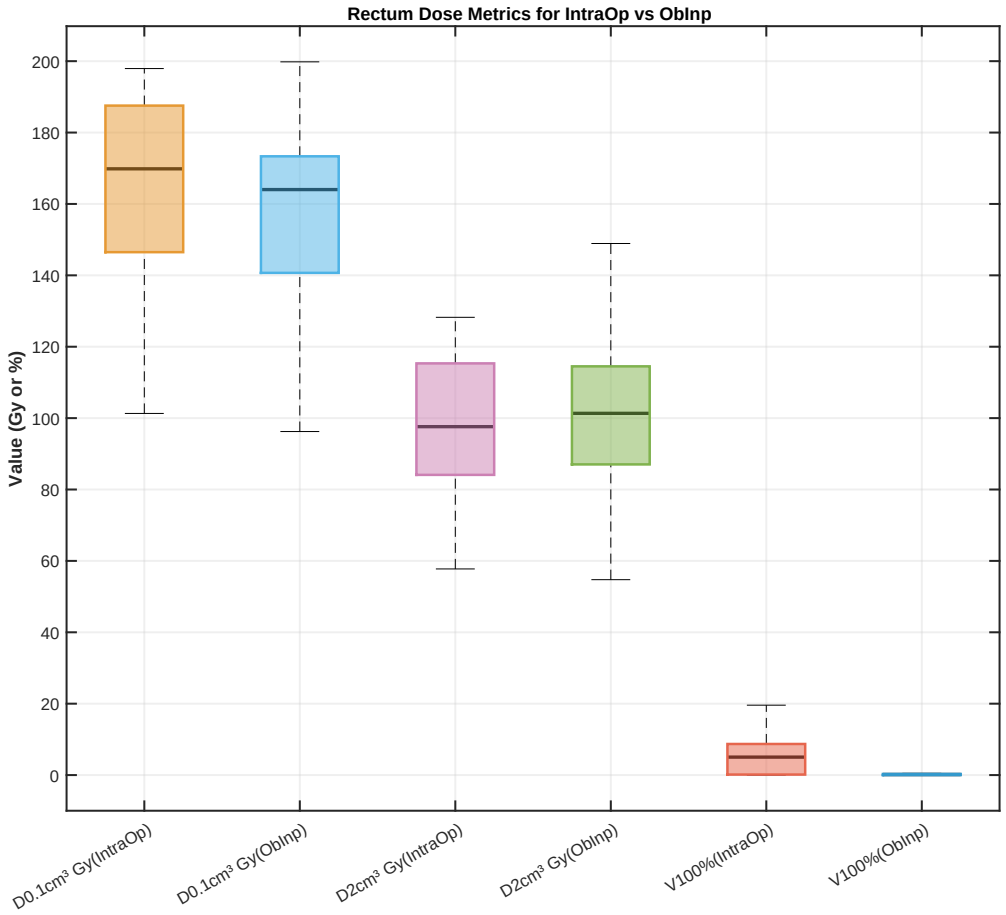

Figure 3.3: Boxplots comparing rectal dose metrics between the intraoperative plan (IntraOp) and oblique inner needle plan (Oblnp). The metrics include D0.1 cm³ Gy (dose for the most exposed 0.1 cm³ of the rectum), D2 cm³ Gy (dose for the most exposed 2 cm³ of the rectum), and V100% (percentage of rectal volume receiving 100% of the prescribed dose). The Oblnp plan demonstrated lower median values for D0.1 cm³ Gy and V100% than the IntraOp plan. However, D2cm³ Gy was slightly higher for ObliqP, whereas V100% demonstrated a substantial reduction, indicating improved rectal dose-sparing.

A boxplot was generated to illustrate the impact of oblique inner needle planning. Figures 3.1, 3.3, and 3.4 demonstrate a notable improvement in the dose distribution to the planning target volume. Specifically, the Figures highlight a significant decrease in the OARs dose with the retrospective plan across most dosimetric parameters. The outliers of prostate V150% indicated a superior treatment plan because this might indirectly be related to the minimised dose

of the OARs. It is also worth noting that the V150% values should fall within the constraint range of 45% to 65% of the prostate volume, as this indicates an optimal plan. Finally, Figure 3.2 shows a successful simulated phantom-based intraoperative procedure. To achieve improved dose distribution and adherence to dose constraints, as shown in Table 2.1. The plan included 19 needles (13 peripheral needles and 6 inner needles) and 90 seeds, with an individual seed activity of 0.506 mCi. Optimal dose coverage was achieved in the phantom, with dose distribution characterised by a V100% coverage of 99.25%, V150% of 56.28% and D90% of 190.55 Gy. The dose to OARs was minimal, with urethra D30% at 125.59 and Rectum D2cm^2 at 76.66%. This representative phantom procedure demonstrates the feasibility of accurate needle insertion using the custom-designed template.

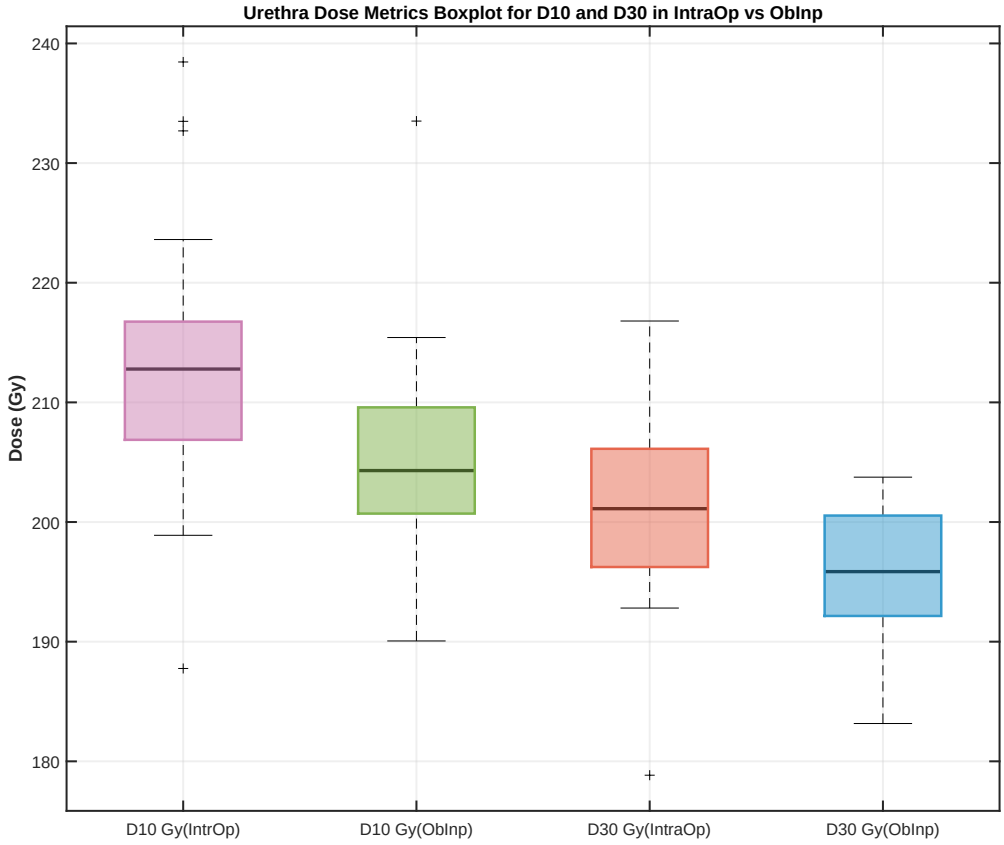

Figure 3.4: Boxplots comparing urethral dose metrics (D10 Gy and D30 Gy) between the intraoperative plan (IntraOp) and oblique inner needle plan (Oblnp). D10 Gy represents the dose for the most exposed 10% of the urethral volume, whereas D30 Gy corresponds to the dose for the most exposed 30% of the urethral volume. The Oblnp plan demonstrated lower median values for both D10 Gy and D30 Gy than IntraOp, indicating improved urethral dose sparing. The presence of multiple outliers in the IntraOp plan highlighted cases of increased urethral dose exposure.

3.2 Part 2: Seed Strength Verification

Figure 3.5 shows the intensity profile of an I-125 seed with an activity of 0.506 mCi (reference activity was 0.543 mCi) placed on a CCD sensor with 3,648 linear pixels. The data was extracted from a single CSV file. The original signal in grey and the denoised signal in red are plotted to show the noise reduction. The high-signal region is highlighted in green, which indicates the position of the seed on the sensor.

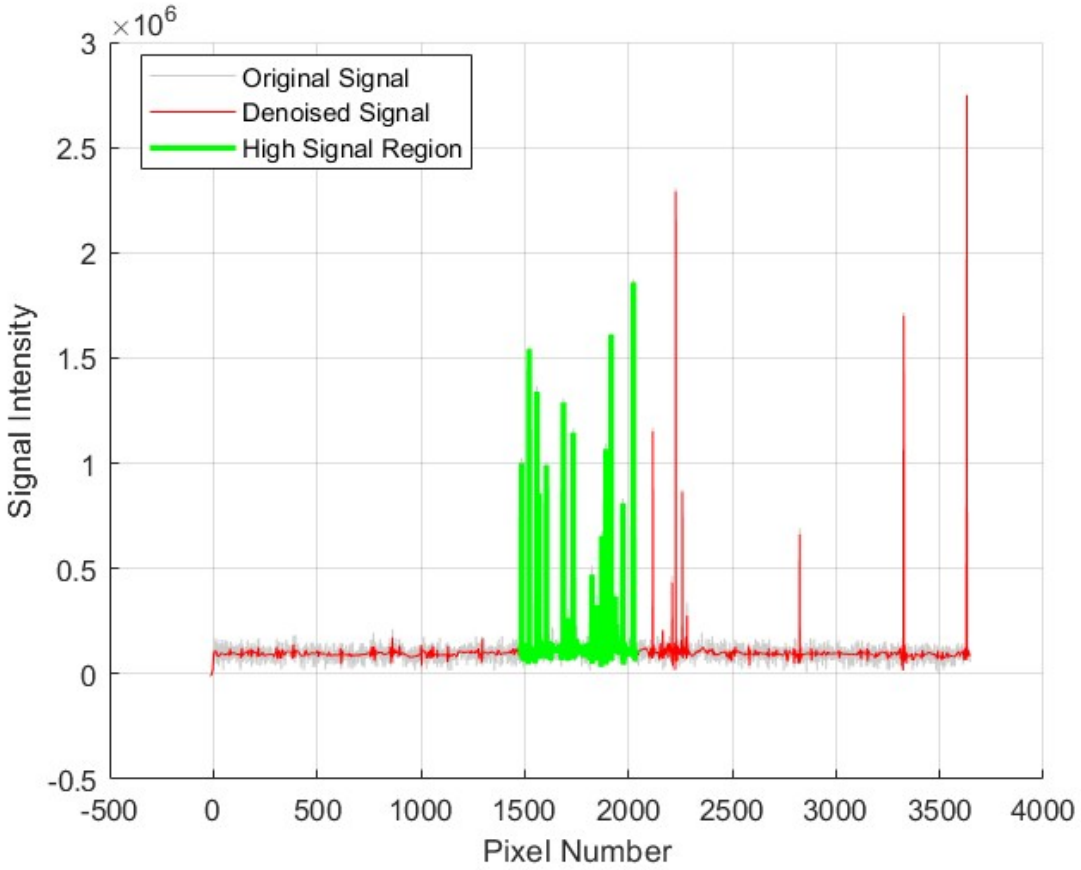

Figure 3.5: Figure shows the denoised measured signal intensity from a single I-125 seed placed on the CCD sensor. The high-signal green region highlights the position of the seed on the sensor. The random peaks observed may be partly due to electronic interference and Compton scattering, where some photons interact with electrons, altering their direction and energy and leading to unpredictable pixel detection. Signal acquired using an exposure time of 26 ms.

The detected peaks within the high signal region, spanning pixel numbers between 1481 and 2043, correspond to the physical length of the seed, stated as 4.5 mm [100]. Specifically, the high-intensity region begins at the pixel $x_{\text{start}} = 1481$ and ends at the pixel $x_{\text{end}} = 2043$. Therefore, the total number of pixels covering this high-signal region is:

$$\Delta x = x_{\text{end}} - x_{\text{start}} = 2028 - 1466 = 562 \text{ pixels}$$

As mentioned previously, the sensor pixel size was 0.008 mm per pixel. This implies that the physical length (L) of the high-intensity region, which represents the length of the radioactive seed, can be calculated as:-

$$L = \Delta x \times \text{pixel size} = 562 \times 0.008\,\text{mm} = 4.496\,\text{mm}$$

The calculated value agreed with the known physical length of the I-125 seeds. The peaks outside the high-intensity region are attributed to Compton and Rayleigh scattering [101], which do not contribute to the high-intensity region associated with the seed.

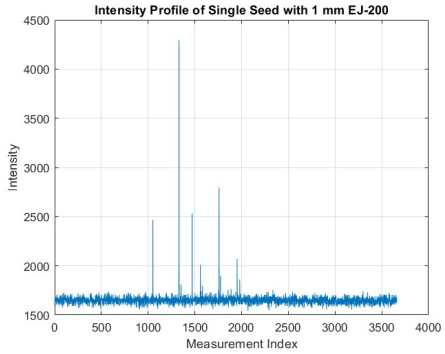

(a) Intensity profile of a single I-125 Seed with 1 mm EJ-200 scintillator sheet fixed directly on the CCD sensor.

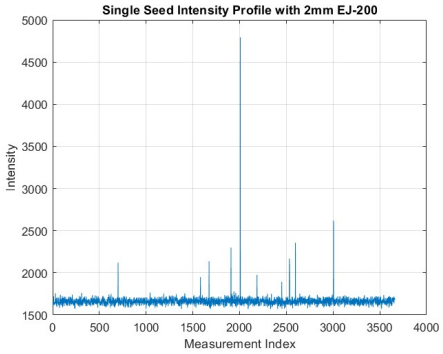

(b) Intensity profile of a single I-125 Seed with 2 mm EJ-200 scintillator sheet fixed directly on the CCD sensor.

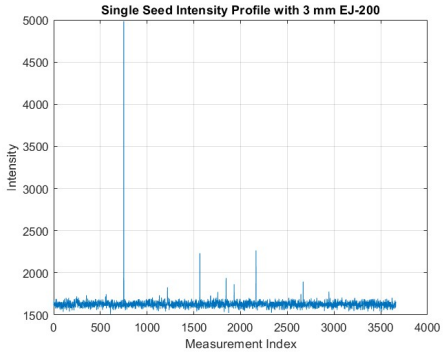

(c) Intensity profile of a single I-125 Seed with a 3 mm EJ-200 scintillator sheet fixed directly on the CCD sensor.

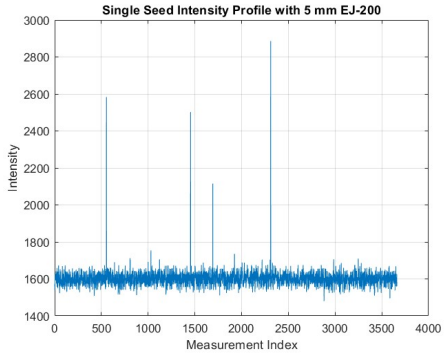

(d) Intensity profile of a single I-125 Seed with 1 mm EJ-200 scintillator sheet fixed directly on the CCD sensor.

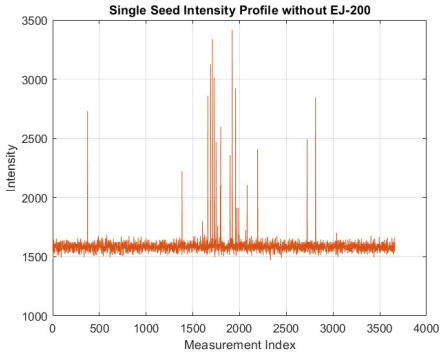

(e) Intensity profile of a single I-125 Seed without EJ-200 scintillator sheet fixed directly on the CCD sensor.

Figure 3.6: Intensity profiles of a single I-125 seed with varying EJ-200 scintillator sheet thicknesses. The y-axis represents the signal intensity (photon counts), and the x-axis corresponds to the pixel number.: (a) 1 mm, (b) 2 mm, (c) 3 mm, (d) 5 mm and (e) without any scintillator on the detector. The exposure time was set to 26 ms.

Table 3.3 and Figure 3.6 present the results of the measurements with varying EJ-200 scintillator thickness to determine the optimal thickness to be used for the detection system. This is important since the efficiency of photon detection depends on the balance between photon absorption by the scintillator and light collection by the sensor. As shown in Figure 3.6, the signal loss was observed in the measurements using the EJ-200 scintillator. This is attributed to the poor coupling between the scintillator and the CCD sensor. The uneven surface of the scintillator sheets, which were manually cut, led to air gaps that introduced reflections and scattering, leading to the creation of artefacts that contributed to the elevation of the peak intensity as seen in Figure 3.6, for measurements with thickness of 1 to 3 mm [102][103]. For measurement with a 5mm EJ-200, the thickness was too thick for efficient signal detection within the given energy range. In the measurement (Figure 3.6(e)) without a scintillator, the position of the seed on the detector can be seen, which is the range with greater signal intensity with a high coefficient of variation of 5.33 %.

Metric	**1 mm**	**2 mm**	**3 mm**	**5 mm**	**No EJ-200**
Seed Activity (mCi)	0.433	0.433	0.433	0.433	0.433
Peak Intensity	4292	4792	4984	2886	3415
Median Intensity	1649	1660	1625	1602	1582
Mean Intensity	1650	1663.6	1628.5	1601.5	1589.5
Intensity Range	2749	3221	3473	1406	1941
Signal-to-Noise Ratio (SNR)	27.07	25.04	24.96	36.59	18.74
Coefficient of Variation (%)	3.7	3.99	4.01	2.73	5.33
Integrated Intensity	6.04×10^6	6.09×10^6	5.96×10^6	5.86×10^6	5.82×10^6

Table 3.3: Summary of metrics of the I-125 Seed intensity profiles for EJ-200 scintillator thicknesses on the detector

Figure 3.7 illustrates the difference in intensity profile for a single seed with an integration time of 10 seconds for measurement with and without EJ-200 scintillator.

The results of applying moving average filters with window sizes of 0, 5, 45, and 99 are plotted and indicate that excessive filtering introduced negative values in the data, especially in the tail region, as can be observed in Figure 3.8. The maximum peak intensity was relatively constant.

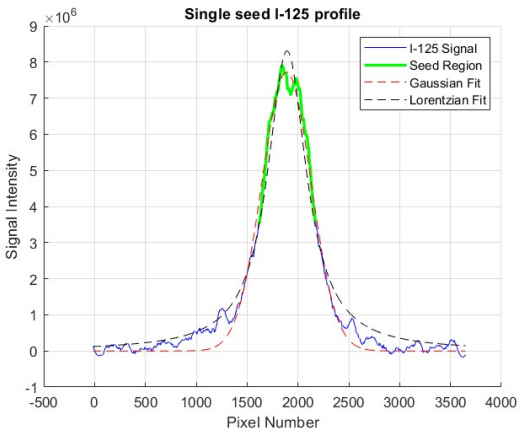

(a) Intensity profile of a single I-125 Seed with an integration time of 10 s.

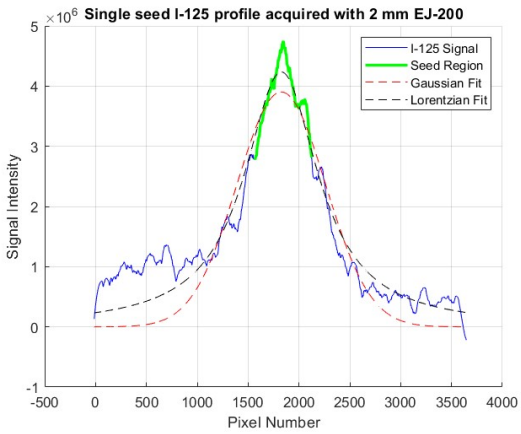

(b) Intensity profile of a single I-125 Seed using the EJ-200 for an integration time of 10 s.

Figure 3.7: Intensity profile of a single I-125 Seed for an integration time of 10 seconds with and without EJ-200 scintillator. The signal with scintillator has a broader FWHM.

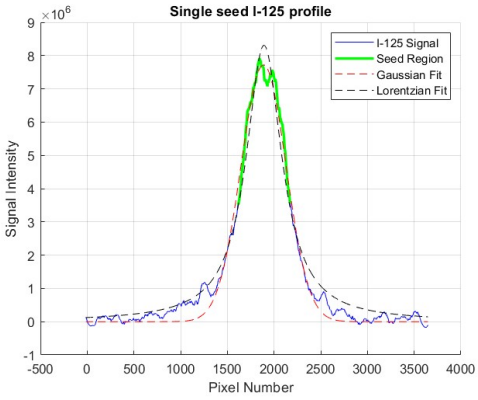

(a) I-125 seed profile acquired over 10 s measurement period, with moving average filter zero (Peak Intensity is 7.909×10^6).

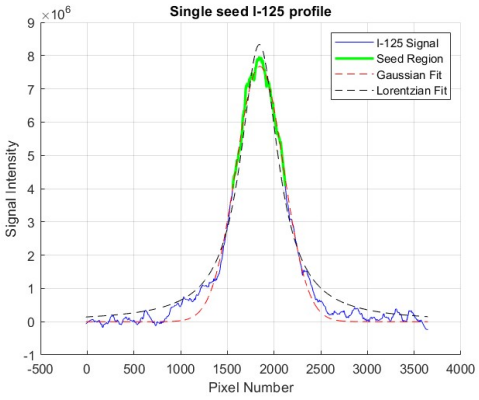

(b) I-125 seed profile acquired over 10 s measurement period, with moving average filter 5 (Peak Intensity is 7.949×10^6).

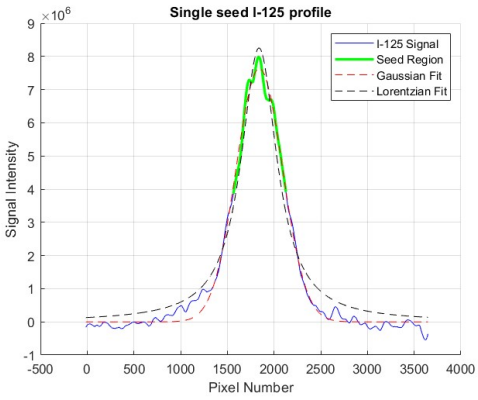

(c) I-125 seed profile acquired over 10 s measurement period, with moving average filter 45 (Peak Intensity is 7.985×10^6).

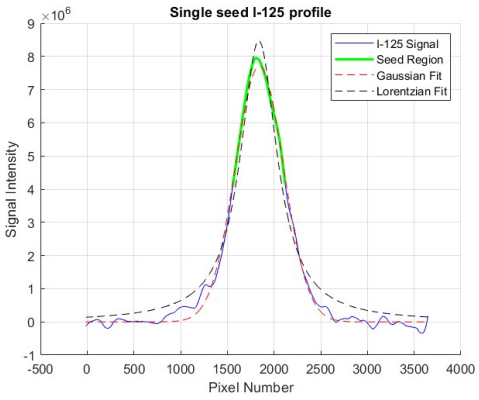

(d) I-125 seed profile acquired over 10 s measurement period, with moving average filter 99 (Peak Intensity is 7.950×10^6).

Figure 3.8: Intensity profiles of a single I-125 seed (Activity 0.433 mCi) with varying moving average filters. The y-axis represents the signal intensity (photon counts), and the x-axis corresponds to the pixel number.: (a) set to Zero, (b) set to 5, (c) set to 45, (d) and set to 99.

Measurements with time durations 10, 15, 20 and 30 s were plotted as shown in Figure 3.9. The mean and median intensities increased with increasing measurement duration, as shown in Table 3.4. This increase can be attributed to multiple factors inherent to the TCD1304 sensor, including dark current accumulation, Compton scattering, potential pixel saturation, and temperature-dependent effects. The dark current accumulation, which arises from thermally generated electrons within the sensor, is directly proportional to the integration time and is further influenced by temperature. As the measurement duration increased, the contribution of the dark current became more significant, leading to an increase in the mean and median intensities. Specific pixels may also approach their full-well capacity at longer exposure times, resulting in charge overflow into adjacent pixels [104]. Furthermore, Compton scattering of 35.5 keV gamma photons from I-125 may introduce additional scattered photons that unpredictably increase the mean and median of the detected signal intensity.

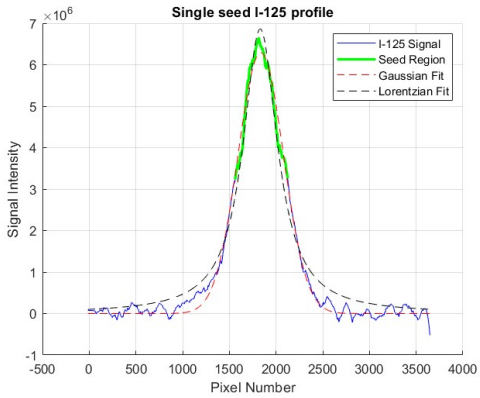

(a) Intensity profile of a single I-125 seed (0.4198 mCi) acquired over a 10 s measurement duration.

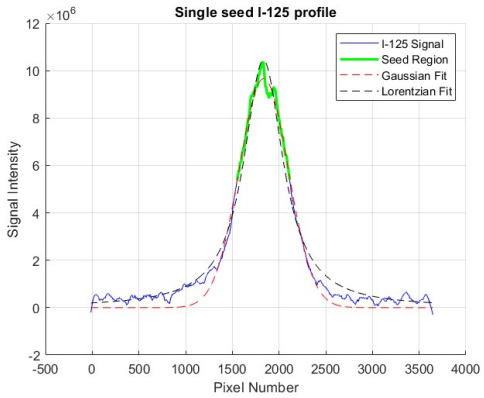

(b) Intensity profile of a single I-125 seed (0.4198 mCi) acquired over a 15 s measurement duration.

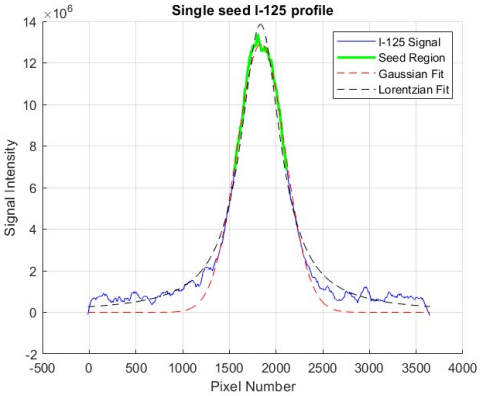

(c) Intensity profile of a single I-125 (0.4198 mCi) seed acquired over a 20 s measurement duration.

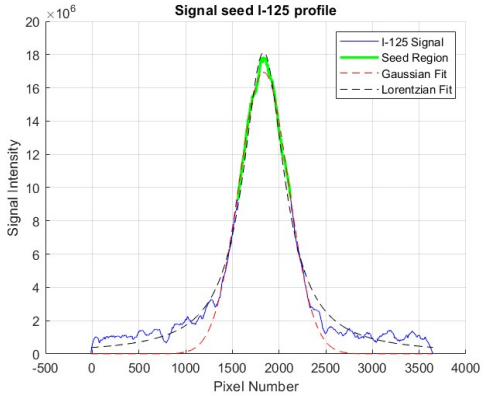

(d) Intensity profile of a single I-125 seed (0.4198 mCi) acquired over a 30 s measurement duration.

Figure 3.9: Intensity profiles of a single I-125 seed (Activity 0.4198 mCi) with measurement duration of (a) 10 s, (b) 15 s, (c) 20 s, (d) 30 s.

Measurement duration	**10 sec**	**15 sec**	**20 sec**	**30 sec**
Seed Activity (mCi)	0.4198	0.4198	0.4198	0.4198
Peak Intensity	6.639×10^6	1.037×10^7	1.335×10^7	1.783×10^7
Median Intensity	1.855×10^5	5.505×10^5	9.46×10^5	1.408×10^6
Mean Intensity	1.092×10^6	2.026×10^6	2.82×10^6	3.872×10^6

Table 3.4: Comparison of peak, mean and median intensity for measurement duration of 10, 15, 20 and 30 seconds.

Data for 10 s duration acquisition for different seed activities (0.506 mCi, 0.448 mCi, 0.489 mCi, 0.059 mCi, 0.122 mCi, 0.054 mCi) were used to calibrate the

seed activity detection. The 10 s measurement duration was chosen because it provided sufficient data for reliable analysis. Although this was an experimental setup, in a clinical setting, choosing a longer duration would increase the procedure time, which is generally considered suboptimal in clinical settings. Seed activity was estimated using a linear regression model based on the known seed activity and the area under the Lorentzian fit curve (Listing A.1 in appendix). Figure 3.10 shows the intensity signal from the I-125 seed strand for seed_space_seed placed on the CCD detector. Similar to the single seed result, the sensor detected the seeds and the spacer. This is observed in the shape of the curve.

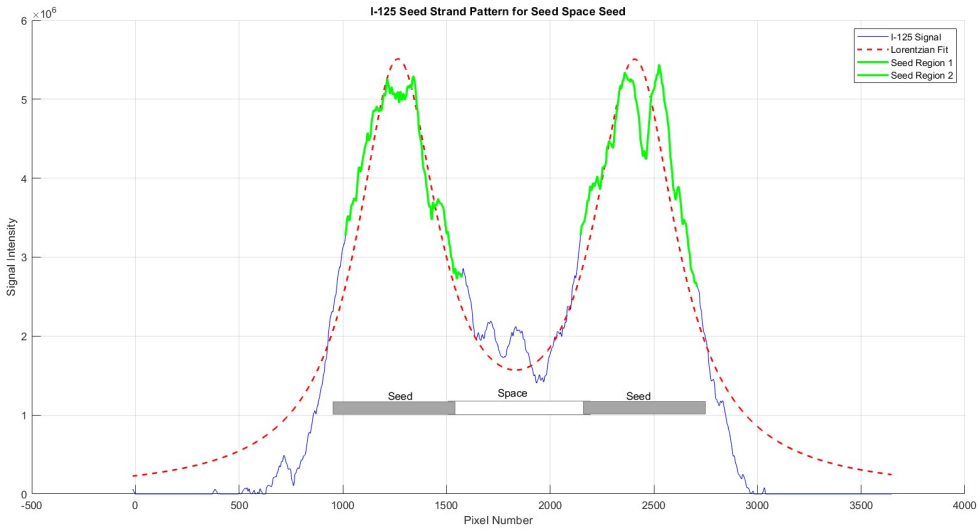

Figure 3.10: Intensity profile of I-125 seed_space_seed strand for an integration time of 10 seconds with Lorentzian fit and illustration of the seed strand.

The intensity profile was fitted using a Lorentzian function. The Lorentzian fit better fitted the I-125 profile because of its narrow peak and longer tail, as shown in Figure 3.11. The maximum of both peaks was 5.5×10^6 while the Gaussian and combined fit had different maxima for each peak. The Lorentzian fit also models scattering at the tail better than the Gaussian fit. Similar to Figure 3.10, the measured intensity profile of a single seed with known activity of 0.448 mCi is presented in Figure 3.12. The measured activity was 0.381 mCi, indicating a difference of 14.96% relative to the nominal value.

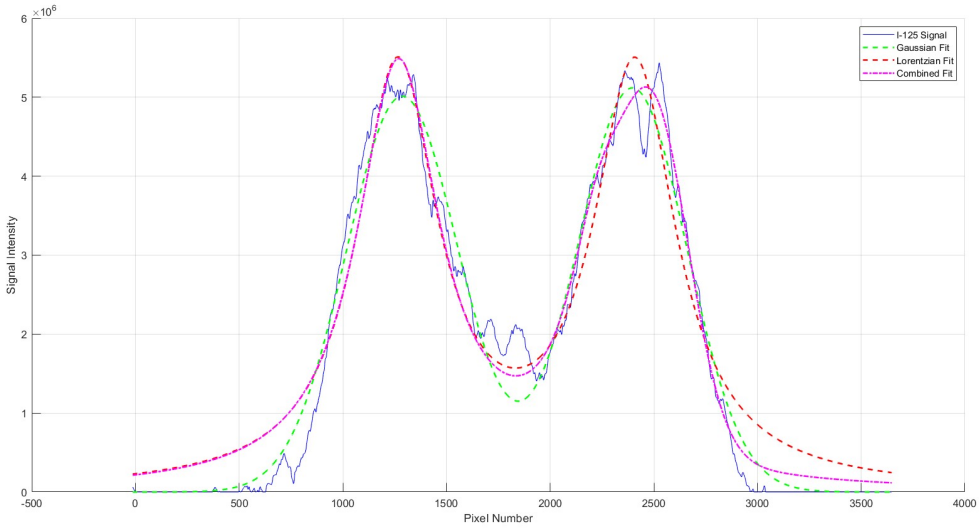

Figure 3.11: Comparison of fit models to the Intensity profile of I-125 seed_space_seed strand for an integration time of 10 seconds.

Table 3.5 presents the results of the signal from the seed_space_seed strand. This includes the centre-to-centre seed distance, detected seed length for each seed, and full-width-half-maximum value for both Lorentzian and Gaussian fits. In addition, the determined activity of each seed was reported with a systematic uncertainty of 0.35%, derived from the radiometric calibration uncertainty of the CCD sensor, as documented by Ferrero et al [105]. An 8.5% percentage difference was observed between the known seed strength and the measured seed strength.

Seed	**Detected length**	**FWHM (Lorentzian)**	**FWHM (Gaussian)**	**Seed Activity**	**Measured Activity**
Seed 1	4.502 mm	3.78 mm	5.09 mm	0.329 mCi	0.303±0.001 mCi
Seed 2	4.502 mm	3.78 mm	5.09 mm	0.329 mCi	0.303±0.001 mCi
Single Seed	4.502 mm	3.74 mm	6.44 mm	0.448 mCi	0.381±0.001 mCi
Calculated centre-to-centre seed distance: 10 mm					
Measured centre-to-centre seed distance: 9.069 ± 0.008 mm					

Table 3.5: Results of the signal from the I-125 seed_space_seed strand intensity profile position on the CCD sensor.

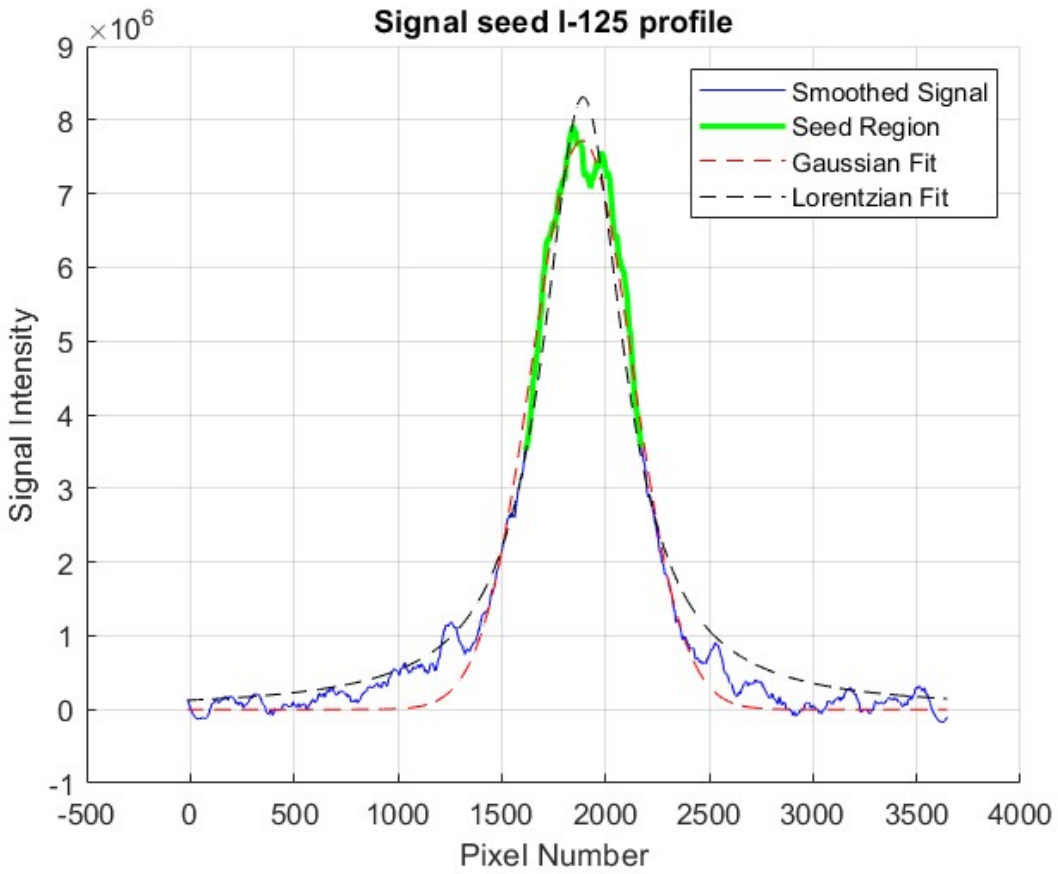

Figure 3.12: Intensity profile of a single I-125 seed with an activity of 0.448 mCi, measured using an integration time of 10 s.

3.3 Part 3: Seed Logistics and Strands

The measured seed strands of different strengths by the linear sensor were analysed. Figure 3.13 shows the strand of a seed-seed-seed strand. The results are shown in Table 3.6. The calculated lengths, derived from the manufacturer's specifications by summing the lengths of each strand component, served as a reference for assessing the accuracy of the measurements [99]. The mean absolute error (MAE), root mean squared error (RMSE), and mean absolute percentage error (MAPE) was calculated as 0.27 mm, 0.30 mm, and 1.6%, respectively, with a coefficient of determination (R^2) of 99.8%. This indicates that the measurement data follows a similar trend as the calculated data.

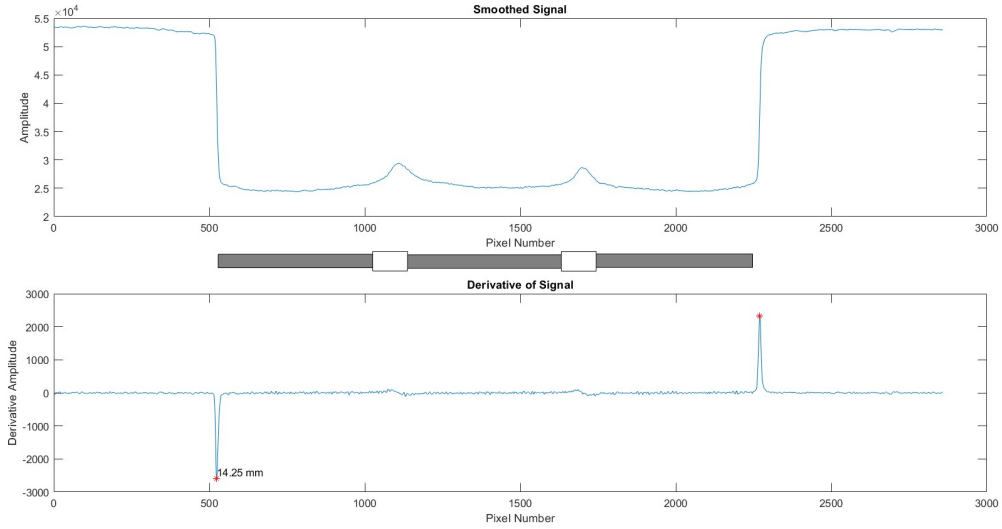

Figure 3.13: Seed Seed Seed pattern with the graphic for visualisation of the mentioned pattern

Reference date/Activity	Strand pattern	Calculated length (mm)	Measured length (mm)	Absolute difference (mm)
18.1.2008/18.3MBq	Single seed	4.50	4.48 ± 0.008	0.02
	Seed-Space-Seed-Space-Seed	24.50	24.20 ± 0.008	0.30
	Seed-Space-Seed-Seed	19.50	19.27 ± 0.008	0.23
	Seed-Seed-Seed	14.50	14.25 ± 0.008	0.25
25.09.2021/18.43MBq	Single seed	4.50	4.56 ± 0.008	0.06
	Seed-Space-Seed-Space-Seed	24.50	24.10 ± 0.008	0.40
	Seed-Space-Seed-Seed	19.50	19.10 ± 0.008	0.40
	Seed-Seed-Seed	14.50	14.13 ± 0.008	0.37
10.12.2022/20.09Mbq	Single seed	4.50	4.56 ± 0.008	0.06
	Seed-Space-Seed-Space-Seed	24.50	24.14 ± 0.008	0.36
	Seed-Space-Seed-Seed	19.50	19.10 ± 0.008	0.40
	Seed-Seed-Seed	14.50	14.13 ± 0.008	0.37

Table 3.6: Groups of Iodine-125 seeds used in brachytherapy showing strand patterns, lengths, and the mean absolute error in millimetres.

None of the signals showed any influence from radioactivity on the measuring sensor. Figures 3.14 and 3.15 show the Bland-Altman and scatter plot with a colour gradient.

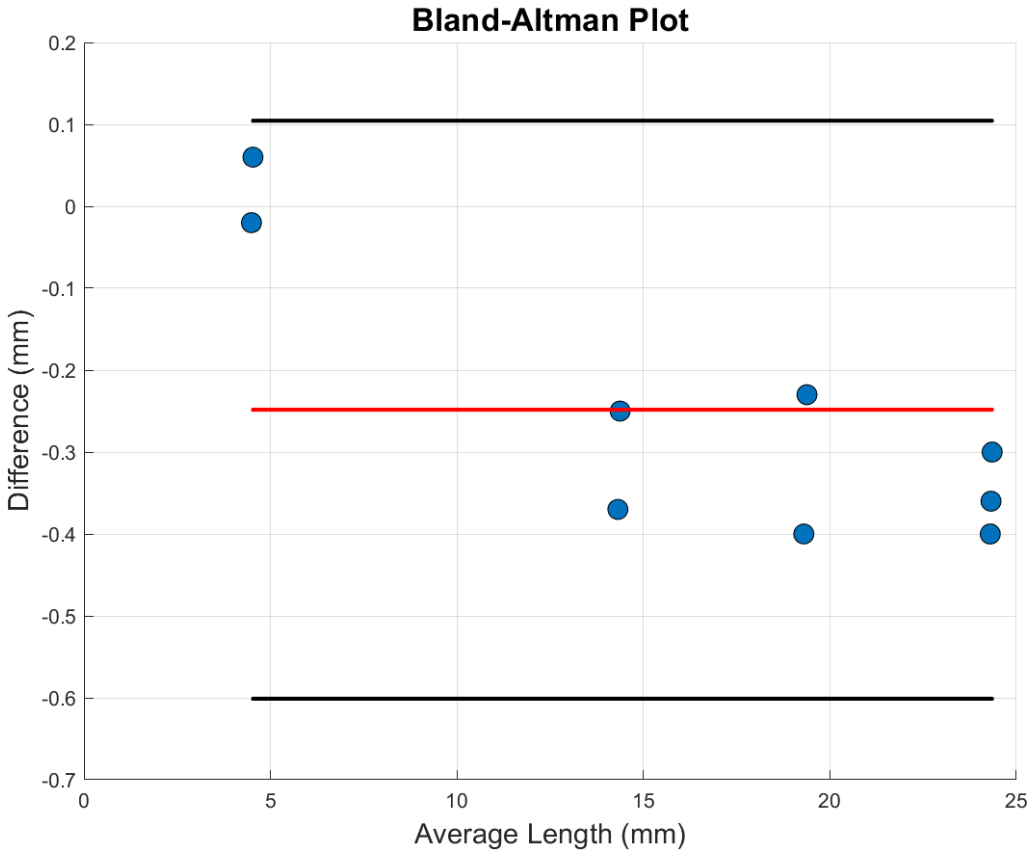

Figure 3.14: Bland-Altman plot of measurement agreement: The plot shows differences between measured and true lengths against their mean values. The red line represents the average bias, and the dark lines indicate the 95% limits of agreement.

The Bland-Altman plot shows that the limits of agreement range from -0.1 mm to +0.6 mm, with a negative mean difference of 0.25 mm between the calculated and measured lengths of the I-125 seed strands, indicating a slight systematic bias. The slight underestimation of the strand lengths is likely due to the degradation of the bioabsorbable SourceLink™ spacers used for seed linkage. The remaining patient spacers employed in the procedure had expired, although they had not been previously opened. According to the manufacturer, the material begins to lose mechanical strength after 150 days [99].

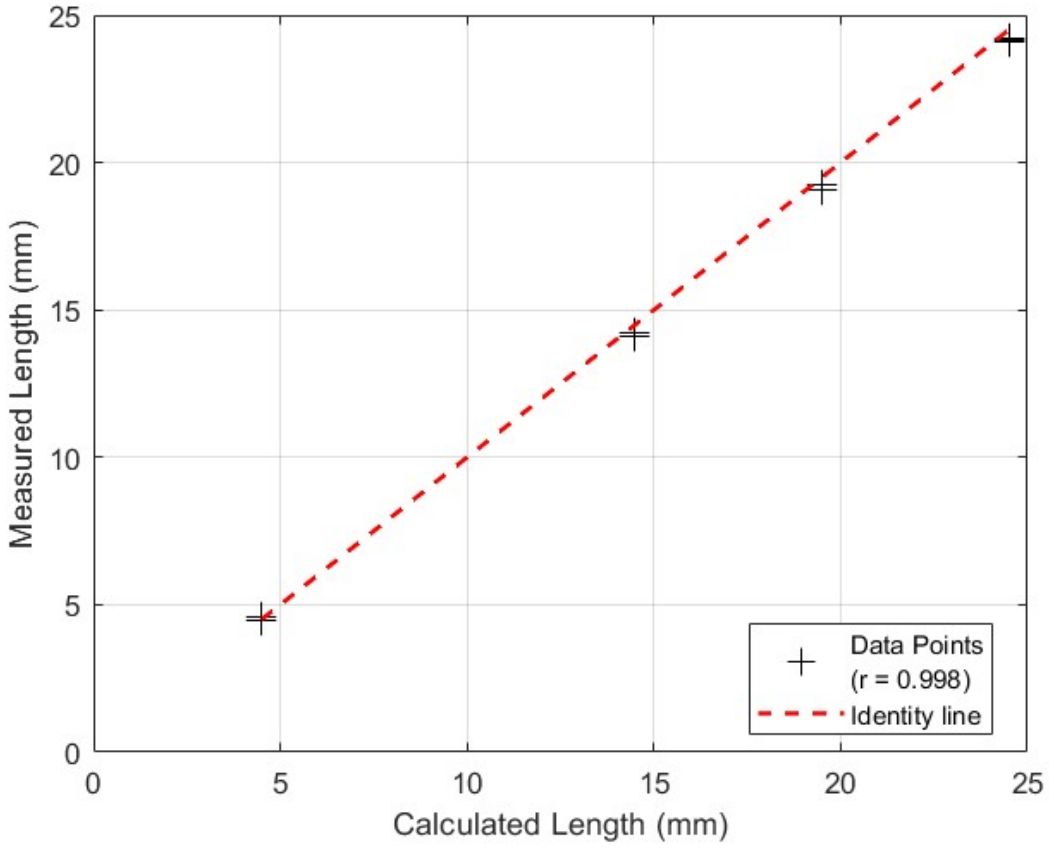

Figure 3.15: Scatter plot with line of equality (y=x) comparing measured and calculated length. Data points from the mid to upper range indicate a slight underestimation. The correlation coefficient is r =0 .998.

This degradation in material integrity may have resulted in strand length reduction due to the compression force applied to the stylet during the assembly of seeds and connectors. Consequently, the sensor's measurement accurately reflected this reduced length, and this factor could also explain the 0.2% unexplained variation. Manual verification using the mentioned digital calliper in section 2.2.1 confirmed this observation (total combined uncertainty of ±0.0382 mm). Figures A.1, A.3, and A.2 in the appendix show the signal outputs obtained from the different seed strands for non-radioactive and radioactive seeds. The same trend as indicated from the Bland-Altman plot is seen in Figure 3.15 showing the scatter plot with an R-value of 0.998.

4. Discussion

4.1 Part 1: Template

The prostate D90 and V150% are crucial parameters, particularly the implications on the urethral dose, as they are associated with potential morbidity such as incontinence [106]. This study has demonstrated that the proposed approach of planning oblique inner needles can substantially increase V100%, reduce V150% and consequently minimise the D10 and D30 for the urethra. The high standard deviation observed in the prostate PTV suggests a wide variability in prostate size within the data set. This indicated that the in-house template was tested across various prostate sizes and proved to be versatile.

The standard template, designed by Dr. J. Hayes and available through Liberty Medical Inc., is designed to mimic the shape of the prostate and comes in three sizes: small (17 needle holes), medium (18 needle holes) and large (22 needle holes) [107]. This template allowed only parallel needle insertion. In contrast, the custom-designed template included nine grid holes that offered additional oblique insertion, enabling more flexible and precise seed placement. This allowed for single-seed deposition at the base, away from the bladder neck, and at the apex, away from the urethra. Using the custom template, the dose to OARs can be minimised compared to the standard template. The template design also mitigates issues with pubic arch interference, as it allows insertion of all needles without the need to tilt the ultrasound probe, thus avoiding obstruction by pubic bones and enhancing the target coverage of the prostate. Furthermore, it potentially solves the historical exclusion of some patients from LDR brachytherapy due to public arc obstruction as shown in Figure 1.4. Compared to the approach by Urribarri et al., who developed and implemented a new needle template with additional rows of 2.5 mm offset holes to improve needle placement in small prostates ($\leq$ 20 cm^3) [108], the custom-designed in-house oblique needle template demonstrated in this retrospective study

improve dose to the target structure and minimise dose to OARs for prostate of varying sizes.

Xuemin Di et al. demonstrated the effectiveness of a 3D printed transperirectal CT-guided brachytherapy template in reducing the rectal dose in patients who had previously undergone treatment [109]. Their case study of two patients showed a reduction in the number of needles required and proved effective for large prostates. The study, with a template using both parallel and oblique insertion features, further emphasises this advantage, showing improved dose conformity compared with plans created using only parallel needles. Although the literature suggests that LDR-PB generally results in lower OAR toxicity compared to other brachytherapy methods [110], this study demonstrates that the use of customisable templates could further benefit patients, particularly those with large prostates or interference with the pubic arch.

The findings in this study support the use of the in-house template for patients with prostate volumes ≥ 65 ml, enabling treatment with improved and more acceptable doses to OARs, so as not to increase the possibility of acute urinary retention and mitigate the effect of large prostate as per the finding of J. Crook et al. [111] By allowing oblique insertion of up to $\pm 30^{\circ}$, the template helps to enhance dose distribution to the target and minimises the dose to OARs.

Furthermore, because oblique insertion allows seed placement from various angles, the template is suitable for focal brachytherapy applications [13]. Although some experienced brachytherapists can place oblique needles without templates, a template offers additional confidence to clinicians, especially those new to the field, allowing them to focus on other critical aspects of the procedure with a reduced risk of injury to the patient. Bon Ruy et al. demonstrated that oblique insertion is feasible without a template, but using a structured guide significantly reduces the learning curve and procedural risks [112].

The results presented demonstrate that the in-house design template design has the potential to reduce the risk of acute urinary retention, which is known to increase with prostate size [111] and for normal size prostate, the results showed a reduction of dose to OARs. With improved dose conformity and minimised OARs exposure, this approach is advantageous for treating all patients with the LDR-PB procedure. The ability to use oblique needles also makes use of the seed anisotropy factor/effect (as shown in Figure 4.1) as investigated by C. C. Ling et al. [113]. The custom in-house template demonstrates significant

advantages in dose conformity, reduced OAR exposure, and adaptability for a range of prostate sizes, supporting its potential for broader clinical application in LDR-PB.

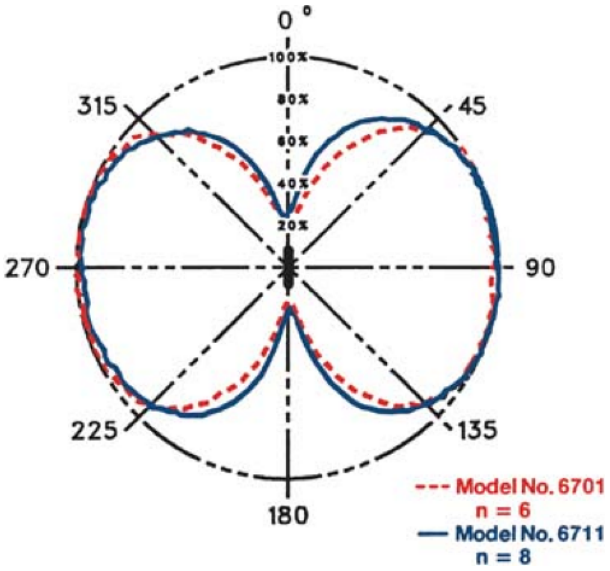

Figure 4.1: Anisotropy of two iodine 125 seed models. The plot represents average results from six 6701 seed models and eight 6711 models, adapted with permission [113].

Finally, research by Jerg K.I. et al. [81] highlighted the sensitivity of seed placement near OARs, validating the importance of oblique inner needles for dose reduction. By leveraging anisotropy in radioactive seed designs, the custom template allows dose gradient manipulation through optimised inner seeds placement. Further studies are needed to quantify the long-term benefits and assess the biological impact of dose reductions achieved using this novel template design.

4.2 Part 2: Seed Strength Verification

This study section demonstrates the feasibility of integrating the Toshiba TCD1304 CCD sensor into the QuickLink™ Loader system for seed activity measurement. The loader is designed to configure the seed strands during LDR-PB intraoperative procedures. The CCD sensor can be integrated into the system to measure and verify the strength of each seed as it is dispensed from the seed cartridge.

Depending on the sensor's location within the QuickLink™ Loader system, a single seed can be measured immediately after it is released from the cartridge before compression with connectors (Figure 4.2). The measurement can also be performed after compression with the connectors. The sensor can be installed at the cartridge-connector bin site, where seed dispensing from the cartridge can be monitored during implantation. Bard Medical Seed cartridges usually contain 10-20 seeds in transparent plastic packages. With an embedded CCD device on the metal wall of the loader system, as illustrated in Figure 4.2, the sensor can measure the total seed activity of the cartridge more effectively than the procedure proposed by John S. Muryn et al. and others in the literature [114][76][87][115], which provides the possibility of measuring and monitoring cartridge activity.

The optimal position for the second sensor, as shown in Figure 4.2 would be best beneath the ruler, centred within the assembly base, with the aforementioned components covered by the lead glass door. This position ensures adequate access to light, which is essential for the sensor's operation. In this configuration, the sensor can accurately manage strand logistics, facilitating precise handling of seeds, connectors, and strands. As highlighted in the results section, the sensor's accuracy also presents the potential for assessing the quality of seed strand connectors. This additionally provides clinicians with valuable information regarding the clinical relevance of strand lengths shorter than intended, which may result from reduced mechanical integrity of the bioabsorbable connector material. Although the manufacturer guarantees 150 days of mechanical integrity for the SourceLink™ spacers, to the author's knowledge, no studies have investigated this issue in clinical LDR-PB systems.

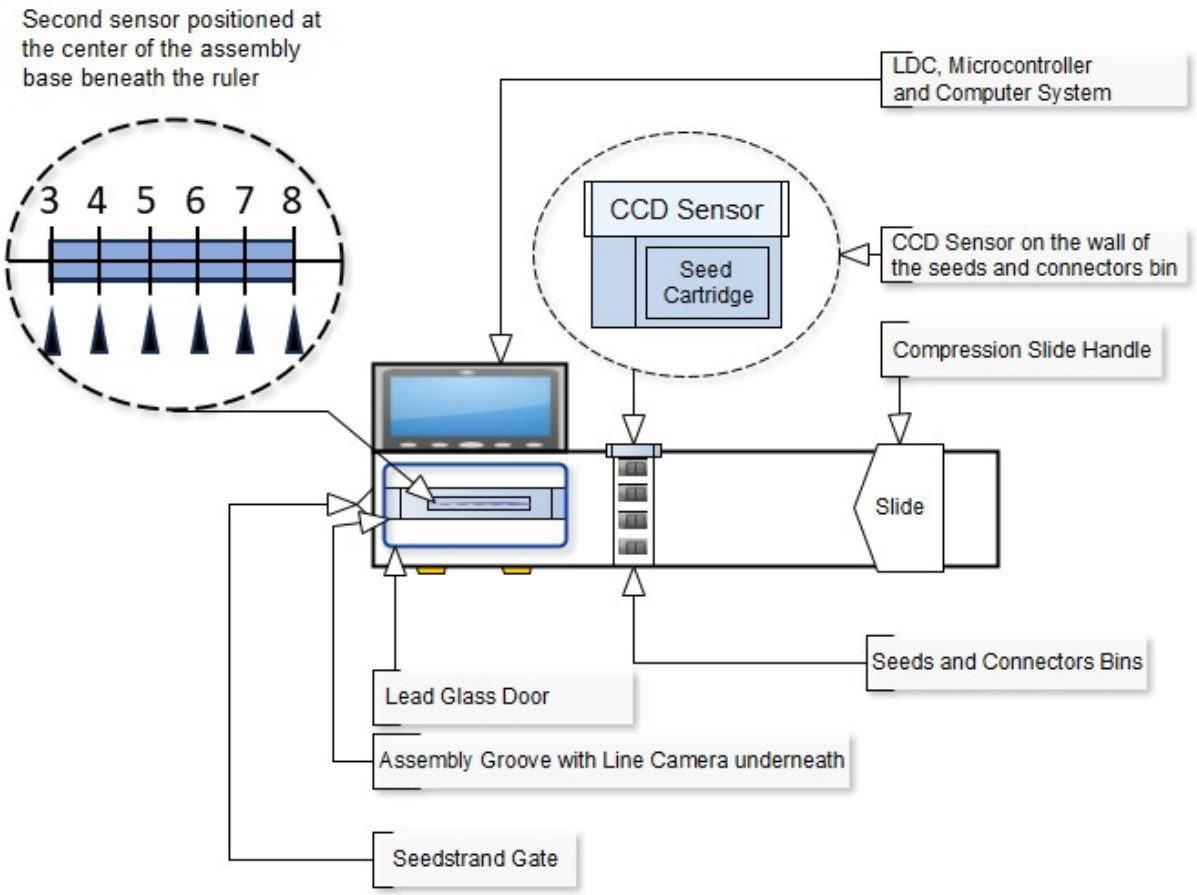

Figure 4.2: Conceptual sketch of the improved Loader system, featuring an integrated LCD screen and a linear CCD sensor embedded within the metal wall of the loader at the position of the source and connectors bin.

The feasibility study by Tanaka et al. proposed a method for estimating the strength of a moving I-125 source during implantation, in which the source is pushed through the needle into the to-be-treated target volume using the needle stylet, with a detector positioned 8 cm from the needle [116]. Although this method demonstrated potential for source strength verification, it presents notable limitations compared to the approach investigated in this study. The 8 cm distance between the detector and the needle in Tanaka's setup could introduce variability in measurement accuracy during the implantation procedure due to potential shielding by adjacent needles and the variable positioning of the active needle. In contrast, the approach presented in this study ensures a consistent measurement distance between the source and detector because the seed is directly positioned on the detector, thereby eliminating distance-dependent uncertainties and shielding effects from other needles.

Additionally, in Tanaka's method, by the time the measuring system provides clinicians with the source strength, the source may already have been implanted into the prostate volume, leaving the clinician to make decisions based on a potentially incorrect implantation activity. In contrast, the approach proposed in this study enables real-time source strength verification before the source is picked up for implantation, allowing clinicians to intervene immediately if an incorrect source activity is detected, thereby reducing the risk of implanting seeds with unintended strengths. Moreover, while Tanaka's method focused on moving seed measurement at an unknown speed, our approach has the potential to measure the activity of moving seeds in the loader system directly on the detector, an aspect that requires further investigation in future studies. These advantages highlight the feasible enhanced functionality and clinical utility of the proposed strategy to address some of the mentioned challenges in real-time intraoperative brachytherapy procedures.

A QuickLink™ Loader system that can measure seed activity in real-time during brachytherapy procedures could offer significant clinical advantages. It would provide clinicians with real-time information on the seed strength levels of each seed, with added confidence that the treatment plan is executed correctly. This real-time feedback could help optimise workflow, improving treatment precision because clinicians are more focused on aspects essential to improved patient outcomes.

Furthermore, measuring seed activity during the treatment phase would eliminate the need for pre or post-procedure radioactive activity assays conducted by medical physicists [57][20][117]. All seeds used for treatment could be continuously measured, reducing the need for a few calibrated seeds or seeds remaining after the procedure, which are then measured to verify the already implanted seeds. This study provides a system with potential benefits in the field of brachytherapy because it opens up new possibilities for developing an advanced and comprehensive seed-tracking system within the loader. In the event of a seed misfeed within the loader, the system allows the clinician to quickly locate the misplaced seed, eliminating the need to interrupt the entire procedure.

Overall, the study suggests that implementing this system could significantly save time for medical physicists, streamline the seed verification process before implantation in the operating room, and mitigate any debate about seed verifi-

cation after implantation. This can improve the overall quality of intraoperative brachytherapy.

However, it is worth noting that this study had some limitations. While the QuickLink™ Loader system's feasibility and potential benefits of the system are demonstrated, it is essential to acknowledge that further work is needed to accurately measure seed activity using an appropriate calibration methodology. Additionally, practical considerations, such as cost, maintenance, sterilisation of the loader, and compatibility with the existing system, should be addressed for successful implementation in clinical settings. This study is the first, as of the time of writing this thesis, to investigate the use of a linear CCD sensor for seed activity measurement intraoperatively and for its potential integration with the QuickLink™ Loader for intraoperative low-dose-rate prostate brachytherapy.

4.3 Part 3: Seed Logistics and Strands

The presented work aimed to develop a system that efficiently counts and documents the configuration of seeds and radioactive seed strands for insertion into the prostate gland during brachytherapy procedures. This work demonstrates the feasibility of integrating the proposed idea into the existing QuickLink™ Loader, making it convenient and practical for clinicians. The system is capable of accurately documenting the number of seeds and seed strands used and can distinguish between various strand patterns. Additionally, incorporating a small portable LCD screen provides clinicians with enhanced visibility for verifying the assembled seed strand.

This real-time feedback could help optimise the workflow, improve treatment precision, and potentially improve patient outcomes. Moreover, recording seed logistics during the treatment phase would eliminate the debate among brachytherapy clinicians in the operating room regarding the number of already implanted seeds. This level of efficiency and precision can enhance the overall quality of brachytherapy.

4.4 Summary of Findings

In the study on investigation of the learning curve (accepted manuscript 2), it is shown that the learning curve of a novice brachytherapist could be shortened by adding a post-intraoperative planning task to the workflow. This task was performed outside the operating room after completion of the procedure and was shown to accelerate the learning rate. The evaluation of the in-house designed prototype template with an oblique insertion option both in Variseed and on a phantom with a target volume size greater than 60 ml indicated a minimal dose to the OAR and a better dose distribution to the target volume. Using the designed template, patients with public arc interference can be treated without exclusion. Similarly, the novel concept of integrating the linear CCD sensor and an LCD screen into the QuickLink loader system would help streamline the workflow and improve the qualitative results. The integration provides the brachytherapy team with comprehensive digital information on I-125 seed/spacer logistics, SourceLink™ material integrity through precise length measurements, radioactive seed strength monitoring, and documentation of assembled seed patterns for each patient treated during the LDR-PB procedure. The possibility of intraoperative verification of seed strength during the procedure represents a substantial advancement over the current recommendation of the AAPM to measure at least 10% of seeds before implantation [20]. This measurement is usually performed a day or two before implantation and involves a radiation exposure risk for the medical physicist performing the seed strength measurement. The sensor can accurately measure the lengths of the seed and the pattern of the seed strands, as shown in Table 3.5. However, as indicated, the variability observed in the radioactive strength measurement suggests that linear calibration is not sufficient to accurately determine the seed strength. This, therefore, sets the stage for further investigation. The idea of implementing a sensor system for the QuickLink loader system has already been discussed with Bard Medical and forwarded to the R&D department. This demonstrates the practical relevance and potential of the study in the real world.

The significance of this strategy in increasing the learning rate for a novice brachytherapist goes beyond shortening the learning curve. Retrospective post-intraoperative plans generated after the operation can be used in a knowledge-based planning database. A brachytherapy TPS with knowledge-based planning capability would benefit the planner because of the added workflow tasks that

would help shorten the learning curve. Brachytherapists can quickly generate high-quality treatment plans based on improved post-intraoperative plans. However, the QuickLink loader system with an incorporated line sensor and screen provides real-time seed activity monitoring and seed-strand tracking. These benefits are valuable to clinicians because they can allocate time to other patient-related aspects of the procedure, such as seed deposition in the target volume. Additionally, because of the oblique needle insertion and seed deposition option, using the in-house design template for focal LDR-PB would serve better than the conventional rigid parallel template.

The impact of this study extends to the post-planning phase. The orderly documentation of seed strands built during the implant procedure improves post-planning procedures, reducing reliance solely on the TPS for counting and identifying seed strands. Since post-dosimetry is usually conducted four weeks after the implant, the spacers have already started to degrade, making it difficult for the planner to identify the strands accurately. Thus, with the available information from the CCD sensor system, the logistics of LDR-PB are improved, leading to greater accuracy in post-implant dosimetry.

4.5 Future Perspectives/Outlook

While this study demonstrates preliminary yet significant outcomes, further validation and development are necessary, especially with respect to the design of the Quickloader system to seamlessly accommodate both the line sensor and the portable LCD screen. Similar to most operating room instruments, the loader must be sterilised after each brachytherapy session. This cannot be performed with the electronic components intact, as the components would be damaged. Therefore, the integration design must consider the dismantling of electronic components before sterilisation. Additionally, the design must incorporate the reuse of electronic components in a sterile environment. Furthermore, to replace the 10% assayed recommendation of the AAPM, the calibration process must be robust and adhere to the standards established by the Physikalisch-Technische Bundesanstalt (PTB), Germany's National Metrology Institute. This guarantees traceability and ensures that the calibration procedure is in accordance with international standards.

Building on this study, future work should aim to refine the line camera calibration or use a coating material on the surface of the detector with a peak

emission wavelength that fits the peak sensitivity range of the sensor. In this study, using the EJ-200 was not optimal because its peak emission wavelength was approximately 425 nm, whereas that of the TCD1304 sensor was between 550 and 600 nm. Furthermore, the coupling between the scintillator and the CCD sensor was not optimal, which affected the detected signal intensity.

5. Conclusion

To address the challenges faced in the treatment of prostate cancer with intraoperative LDR brachytherapy modality, this study evaluated the components of the procedure that influenced the quality and outcome of the treatment. By investigating the learning curve, evaluating the proposed oblique template, and incorporating the linear CCD sensor into the QuickLink™ loader for both radioactive source logistics and strength verification, the investigation aimed to overcome both the challenges in the procedure and possible limitations in patient selection. Drawing on the experience with LDR-PB, addressing these challenges is essential and would help mitigate the decline of the modality in practice and hospitals.

Additionally, this work demonstrates the feasibility of enhancing the QuickLink™ loader system with additional functionality to serve as a quality assurance tool for seed strand logistics, verification of seed-spacer arrangement, assessment of source link integrity, and real-time seed strength evaluation during intraoperative LDR-PB procedures.

In conclusion, the concept provides a valuable tool for process control and quality assurance. It equips brachytherapy clinicians with the means to minimise risk and provide high-quality intraoperative treatment. Implementing these concepts will also lead to safer, more efficient, and error-free prostate brachytherapy procedures, ultimately benefiting both patients and clinicians. A system is proposed that allows clinicians to concentrate on the critical aspects of the prostate seed implant process, thereby eliminating potential confusion during the procedure in the operation room. This system can potentially improve the overall efficiency of LDR-PB treatment, ensuring a smoother experience for clinicians.

Bibliography

[1] World Cancer Research Fund. Prostate cancer statistics vworld cancer research fund international. https://www.wcrf.org/cancer-trends/prostate-cancer-statistics/. [Accessed 03-09-2024].

[2] World Health Organization (WHO). Cancer today. https://gco.iarc.who.int/today/en, 2024. Accessed: 03-Sep-2024.

[3] Sung Hyuna, Ferlay Jacques, Siegel Rebecca L., Laversanne Mathieu, Soerjomataram Isabelle, Jemal Ahmedin, and Bray Freddie. Global cancer statistics 2020: Globocan estimates of incidence and mortality worldwide for 36 cancers in 185 countries. *CA: A Cancer Journal for Clinicians*, 71(3):209–249, 2021.

[4] Roderick C. N. van den Bergh, Stacy Loeb, and Monique J. Roobol. Impact of early diagnosis of prostate cancer on survival outcomes. *European Urology Focus*, 1(2):137–146, 2015.

[5] Pamela McMahon Daniel A. Ollendorf, Julia Hayes and Steven D. Pearson. ICER Report Suggests Similar Levels of Effectiveness among Management and Treatment Options for Low-Risk Prostate Cancer - ICER — icer.org. https://icer.org/news-insights/press-releases/final-harmonized-report-010509/. [Accessed 05-09-2024].

[6] A Harat, M Harat, and M Martinson. A Cost-Effectiveness and Quality of Life Analysis of Different Approaches to the Management and Treatment of Localized Prostate Cancer — ncbi.nlm.nih.gov. https://www.ncbi.nlm.nih.gov/pmc/articles/PMC7026676/. [Accessed 05-09-2024].

[7] Oncology Medical Physics. Prostate brachytherapy, 2024. Accessed: 2024-11-19.

[8] Martin Jeffrey M., Handorf Elizabeth A., Kutikov Alexander, Uzzo Robert G., Bekelman Justin E., Horwitz Eric M., and Smaldone Marc C. The rise and fall of prostate brachytherapy: Use of brachytherapy for the treatment of localized prostate cancer in the national cancer data base. *Cancer*, 120(14):2114–2121, 2014.

[9] Usama Mahmood, Thomas Pugh, Steven Frank, Lawrence Levy, Gary Walker, Waqar Haque, Matthew Koshy, William Graber, David Swanson, Karen Hoffman, Deborah Kuban, and Andrew Lee. Declining use of brachytherapy for the treatment of prostate cancer. *Brachytherapy*, 13(2):157–162, 2014.

[10] NHJ Bittner, BW Cox, B Davis, M King, CA Lawton, GS Merrick, P Orio, Z Ouhib, P Rossi, T Showalter, W Jr Small, and NR Schechter. ACR-ABS-ASTRO Practice Parameter for Transperineal Permanent Brachytherapy of Prostate Cancer - PubMed — pubmed.ncbi.nlm.nih.gov. https://pubmed.ncbi.nlm.nih.gov/35588224/. [Accessed 04-09-2024].

[11] Sophie J. Otter, Alexandra J. Stewart, and Phillip M. Devlin. Modern brachytherapy. *Hematology/Oncology Clinics of North America*, 33(6):1011–1025, 2019. Contemporary Topics in Radiation Medicine, Part I: Current Issues and Techniques.

[12] A Armstrong, H Ho, M. Mark, Tacey, D Bolton, Y Chan, A Tan, C W Cham, T Pham, K McMillan, G Koufogiannis, G Dip, P Manohar, M Guerrieri, M Ng, D L Joon, F Foroudi, M Y Tan, and M Chao. Low-dose-rate brachytherapy and long-term treatment outcomes in patients younger than 60 years of age — ncbi.nlm.nih.gov. https://www.ncbi.nlm.nih.gov/pmc/articles/PMC10993894/. [Accessed 06-09-2024].

[13] S. S. Mahdavi, I. T. Spadinger, S. E. Salcudean, P. Kozlowski, S. D. Chang, T. Ng, J. Lobo, G. Nir, H. Moradi, M. Peacock, and W. J. Morris. Focal application of low-dose-rate brachytherapy for prostate cancer: a pilot study. *Journal of Contemporary Brachytherapy*, 9(3):197–208, Jun 2017. Epub 2017 Jun 13.

[14] Bradley R. Prestidge and William S. Bice. Clinical outcomes of a phase ii, multi-institutional cesium-131 permanent prostate brachytherapy trial. *Brachytherapy*, 6(2):78, 2007.

[15] Brian J Moran, Stephanie R. Rice, Arpit M. Chhabra, Neha Amin, Michelle Braccioforte, and Manuj Agarwal. Long-term biochemical outcomes using cesium-131 in prostate brachytherapy - PubMed — pubmed.ncbi.nlm.nih.gov. https://pubmed.ncbi.nlm.nih.gov/31427178/. [Accessed 13-09-2024].

[16] Martin T. King, Mira Keyes, Steven J Frank, Juanita M. Crook, Wayne M. Butler, Peter J. Rossi, Brett W. Cox, Timothy N. Showalter, Firas Mourtada, Louis Potters, Richard G. Stock, Marisa A. Kollmeier, Michael J. Zelefsky, Brian J. Davis, Gregory S. Merrick, and Peter F. Orio. Low dose rate brachytherapy for primary treatment of localized prostate cancer: A systemic review and executive summary of an evidence-based consensus statement. *Brachytherapy*, 20(6):1114–1129, 2021.

[17] Joseph Safdieh, Andrew Wong, Joseph P. Weiner, David Schwartz, and David Schreiber. Utilization of prostate brachytherapy for low-risk prostate cancer: Is the decline overstated? *Journal of Contemporary Brachytherapy*, 8(4):289–293, 2016.

[18] Becton, Dickinson and Company. Bard® brachysource® i-125 implants with sourcecap™, 2022. [Online]. Available: https://eu.bd.com/emea-peripheral-interventions/lib/asset/227.pdf. [Accessed: 18-Oct-2024].

[19] Felix Fels, Ernest Okonkwo, Jörg Günter Großmann, Thomas Schadt, Sebastian Laschke, György Lövey, Dieter Lansing, Ulrich Freund, Reiner Steurer, and Felix Momm. Permanent interstitial low-dose-rate brachytherapy for prostate cancer: institutional experience with implementation and predictive factors for outcome and side effects. *Journal of Radiotherapy in Practice*, 22:e103, 2023.

[20] Yan Yu, Lowell L. Anderson, Zuofeng Li, David E. Mellenberg, Ravinder Nath, M. C. Schell, Frank M. Waterman, Andrew Wu, and John C. Blasko. Permanent prostate seed implant brachytherapy: Report of the american association of physicists in medicine task group no. 64. *Medical Physics*, 26(10):2054–2076, 1999.

[21] King Matin, T. Low dose rate brachytherapy for primary treatment of localized prostate cancer: A systemic review and executive summary of an evidence-based consensus statement - PubMed — pubmed.ncbi.nlm.nih.gov. https://pubmed.ncbi.nlm.nih.gov/34509378/. [Accessed 10-09-2024].

[22] Qinghua Huang and Zhaozheng Zeng. A review on real-time 3d ultrasound imaging technology. *BioMed Research International*, 2017(1):6027029, 2017.

[23] Brian J. Davis, Eric M. Horwitz, W. Robert Lee, Juanita M. Crook, Richard G. Stock, Gregory S. Merrick, Wayne M. Butler, Peter D. Grimm, Nelson N. Stone, Louis Potters, Anthony L. Zietman, and Michael J. Zelefsky. American brachytherapy society consensus guidelines for transrectal ultrasound-guided permanent prostate brachytherapy. *Brachytherapy*, 11(1):6–19, 2012. Special Issue: American Brachytherapy Society Guidelines for Prostate and Gynecology.

[24] Reyhaneh Nosrati, Matthew Wronski, Chia-Lin Tseng, Hans Chung, Ana Pejović-Milić, Gerard Morton, and Greg J. Stanisz. Postimplant dosimetry of permanent prostate brachytherapy: Comparison of mri-only and ct-mri fusion-based workflows. *International Journal of Radiation Oncology*Biology*Physics*, 106(1):206–215, 2020.

[25] P Blanchard, C Ménard, and S J Frank. Clinical Use of Magnetic Resonance Imaging Across the Prostate Brachytherapy Workflow — ncbi.nlm.nih.gov. https://www.ncbi.nlm.nih.gov/pmc/articles/PMC6075683/. [Accessed 11-09-2024].

[26] H Kunogi, Y Wakumoto, T Kawamoto, M Oshima, S Horie, and K Sasai. Focal low-dose-rate prostate brachytherapy for low- and intermediate-risk prostate cancer — ncbi.nlm.nih.gov. https://www.ncbi.nlm.nih.gov/pmc/articles/PMC7787206/. [Accessed 11-09-2024].

[27] Michael S. Schaulin, Guila Delouya, Daniel Zwahlen, and Daniel Taussky. Tracing the evolution of prostate brachytherapy in the 20th century. *Oncology*, 102(3):283–290, 10 2023.

[28] Glenn P. Glasgow. Low-Dose-rate brachytherapy. https://oncohemakey.com/low-dose-rate-brachytherapy/.

[Accessed 16-09-2024].

[29] IsoRay. sec.gov. https://www.sec.gov/Archives/edgar/data/728387/000114420405031397/v027047_10ksb.htm. [Accessed 16-09-2024].

[30] Mark J. Rivard. Monte carlo characterization of cs-131 brachytherapy source. *Brachytherapy*, 6(2):112, 2007.

[31] J Booher, P Domenig, B Goldman, T Campbell, K Verdecchia, J A Boura, and P J Chuba. Comparison of Three Groups of Patients Having Low Dose Rate Prostate Brachytherapy: Prostate-Specific Antigen Failure and Overall Survival — ncbi.nlm.nih.gov. https://www.ncbi.nlm.nih.gov/pmc/articles/PMC8532522/. [Accessed 14-09-2024].

[32] Mark K. Murphy, R. Kim Piper, Lawrence R. Greenwood, Michael G. Mitch, Paul J. Lamperti, Stephen M. Seltzer, Matt J. Bales, and Mark H. Phillips. Evaluation of the new cesium-131 seed for use in low-energy x-ray brachytherapy. *Medical Physics*, 31(6):1529–1538, 2004.

[33] William S. Bice, Bradley R. Prestidge, Steven M. Kurtzman, Sushil Beriwal, Brian J. Moran, Rakesh R. Patel, and Mark J. Rivard. Recommendations for permanent prostate brachytherapy with 131cs: A consensus report from the cesium advisory group. *Brachytherapy*, 7(4):290–296, 2008.

[34] Bayerisches Landesamt für Umwelt. Merkblatt un2910 - radioaktive stoffe, freigestelltes versandstück, 2023. [Accessed: 2025-01-17].

[35] Wayne M. Butler, William S. Bice Jr., Larry A. DeWerd, James M. Hevezi, M. Saiful Huq, Geoffrey S. Ibbott, Jatinder R. Palta, Mark J. Rivard, Jan P. Seuntjens, and Bruce R. Thomadsen. Third-party brachytherapy source calibrations and physicist responsibilities: Report of the aapm low energy brachytherapy source calibration working group. *Medical Physics*, 35(9):3860–3865, 2008.

[36] Jose Perez-Calatayud, Facundo Ballester, Åsa Carlsson Tedgren, Alex Rijnders, Mark J. Rivard, Michael Andrássy, Yury Niatsetski, Thorsten Schneider, and Frank-André Siebert. Gec-estro acrop recommendations on calibration and traceability of le-ldr photon-emitting brachytherapy sources at the hospital level. *Radiotherapy and Oncology*, 135:120–129, 2019.

[37] Eckert & Ziegler®. About us - eckert & ziegler, 2025. [Accessed: 2025-01-17].

[38] Becton Dickinson®. Product page: 1251csf, 2025. [Accessed: 2025-01-17].

[39] Eckert & Ziegler Medical. IsoSeed I-125 - Radioactive Seed for Brachytherapy, 2025. [Accessed: 2025-01-17].

[40] Donald B Fuller, James A Koziol, and Anne C Feng. Prostate brachytherapy seed migration and dosimetry: analysis of stranded sources and other potential predictive factors. *Brachytherapy*, 3(1):10–19, 2004.

[41] Mahdi Aima, Larry A. DeWerd, Michael G. Mitch, Charles G. Hammer, and William S. Culberson. Dosimetric characterization of a new directional low-dose rate brachytherapy source. *Medical Physics*, May 2018. Epub ahead of print.

[42] Richard Stock, David Beyer, Jed Kaminetsky, and William Ge. Performance of a palladium-103 line source for prostate brachytherapy implants: A phase i trial. *Brachytherapy*, 16(5):1007–1012, September 2017.

[43] CivaTech Oncology. CivaSheet. `https://civatechoncology.com/civasheet/`. Accessed: 2024-12-02.

[44] A. S. Meigooni, H. Zhang, J. R. Clark, V. Rachabatthula, and R. A. Koona. Dosimetric characteristics of the new radiocoil™ wire line source for use in permanent brachytherapy implants. *Medical Physics*, 31(11):3095–3105, 2004.

[45] David J. Eaton. Electronic brachytherapy–current status and future directions. *British Journal of Radiology*, 88(1049):20150002, May 2015. Epub 2015 Mar 6.

[46] J.H.L. Mott and J.M. Daniel. Interactions of electromagnetic radiation and subatomic particles with matter – part 1. *Clinical Oncology*, 33(7):451–454, 2021. doi: 10.1016/j.clon.2021.02.004.

[47] Raja Aamir. *Using MARS Spectral CT for Identifying Biomedical Nanoparticles.* PhD thesis, 08, 08 2013.

[48] Ervin B. Podgorsak. *Radiation Physics for Medical Physicists.* Springer, Berlin, Heidelberg, 2005. Published as part of the Medical Physics Journal series.

[49] You Hu, Shirley Yuen, Tom Pickles, Mira Keyes, and WJ Morris. Impact of urethral-sparing techniques on urinary morbidity in low-dose-rate prostate brachytherapy. *Brachytherapy*, 19(1):37–45, 2019.

[50] OncohemaKey. Physics and dosimetry of brachytherapy, 2024. Accessed: 23-Dec-2024.

[51] Robert D. Zwicker. Quimby-based brachytherapy systems, 2005. Accessed: 23-Dec-2024.

[52] Ginette Marinello. Paris system for interstitial brachytherapy. In Yves Lemoigne and Alessandra Caner, editors, *Radiotherapy and Brachytherapy*, pages 219–225, Dordrecht, 2009. Springer Netherlands.

[53] S. B. Awan, M. Hussain, S. A. Dini, and A. S. Meigooni. Historical review of interstitial prostate brachytherapy. *Iranian Journal of Radiation Research*, 5(4):153–168, 2008. Review article.

[54] Mark J. Rivard, Bert M. Coursey, Larry A. DeWerd, William F. Hanson, M. Saiful Huq, Geoffrey S. Ibbott, Michael G. Mitch, Ravinder Nath, and Jeffrey F. Williamson. Update of aapm task group no. 43 report: A revised aapm protocol for brachytherapy dose calculations. *Medical Physics*, 31(3):633–674, 2004.

[55] Dylan Mann-Krzisnik, Frank Verhaegen, and Shirin A. Enger. The influence of tissue composition uncertainty on dose distributions in brachytherapy. *Radiotherapy and Oncology*, 126(3):394–410, 2018.

[56] Luc Beaulieu, Åsa Carlsson Tedgren, Jean-François Carrier, Stephen D. Davis, Firas Mourtada, Mark J. Rivard, Rowan M. Thomson, Frank Verhaegen, Todd A. Wareing, and Jeffrey F. Williamson. Report of the task group 186 on model-based dose calculation methods in brachytherapy beyond the tg-43 formalism: Current status and recommendations for clinical implementation. *Medical Physics*, 39(10):6208–6236, 2012.

[57] Ravinder Nath, Lowell L. Anderson, Jerome A. Meli, Arthur J. Olch, Judith Anne Stitt, and Jeffrey F. Williamson. Code of practice for brachytherapy physics: Report of the aapm radiation therapy committee task group no. 56. *Medical Physics*, 24(10):1557–1598, 1997.

[58] Carl Salembier, Pablo Lavagnini, Philippe Nickers, Paola Mangili, Alex Rijnders, Alfredo Polo, Jack Venselaar, and Peter Hoskin. Tumour and

target volumes in permanent prostate brachytherapy: A supplement to the estro/eau/eortc recommendations on prostate brachytherapy. *Radiotherapy and Oncology*, 83(1):3–10, 2007.

[59] Ann Henry, Bradley R. Pieters, Frank André Siebert, and Peter Hoskin. Gec-estro acrop prostate brachytherapy guidelines. *Radiotherapy and Oncology*, 167:244–251, 2022.

[60] Ronald S. Sloboda. Optimization of brachytherapy dose distributions by simulated annealing. *Medical Physics*, 19(4):955–964, July–August 1992.

[61] A. M. Elbasan. Monte carlo simulation of dose rate distributions around brachytherapy sources, 2016. [Accessed: 2025-01-18].

[62] C Shen, J Davies, T Siauw, E Poulin, K Gonzalez, J Larson, X Huang, C Sprague, S Ganguli, J Jensen, E Lessard, V Weinberg, J Pouliot, I Hsu, P Keall, HT Chung, L Ball, and MK Buyyounouski. Rapid treatment planning for low-dose-rate prostate brachytherapy with tp-gan. arXiv preprint arXiv:2103.09996, 2021.

[63] Peter R Carroll, Kelly L Greene, and Katsuto Shinohara. A unified approach to prostate cancer diagnosis and treatment was developed at the university of california, san francisco. *Journal of Clinical Oncology*, 23(32):8172–8175, 2005.

[64] Aniket Moitra, Shubham Choudhury, and Yogesh Ghadi. Solving the brachytherapy seed placement problem using simulated annealing and greedy algorithm. *Journal of Computational Oncology*, 3(1):1–15, 2023.

[65] Jin Zhang, Xinjun Li, Xiaobo Wang, et al. A new technique for transperirectal iodine-125 seed implantation in prostatic cancer guided by ct and 3d printed template: Two case reports. *Frontiers in Oncology*, 12:1031970, 2022.

[66] Ming-Wei Huang, Jian-Guo Zhang, Lei Zheng, Shu-Ming Liu, and Guang-Yan Yu. Accuracy evaluation of a 3D-printed individual template for needle guidance in head and neck brachytherapy. *Journal of Radiation Research*, 57(6):662–667, 12 2016.

[67] Mark J. Rivard, Dee-Ann Radford Evans, and Ian Kay. A technical evaluation of the nucletron first system: Conformance of a remote afterloading brachytherapy seed implantation system to manufacturer specifications

and aapm task group report recommendations. *Journal of Applied Clinical Medical Physics*, 6(1):22–50, 2005.

[68] Laurence Thomas, Antony Chemin, Nicolas Leduc, Sarah Belhomme, Emilie Rich, Olivier Lasbareilles, Antoine Giraud, Edouard Descat, Guilhem Roubaud, and Paul Sargos. Manual vs. automated implantation of seeds in prostate brachytherapy: Oncologic results from a single-center study. *Brachytherapy*, 17(1):214–220, 2018. Treatment Delivery Verification in Brachytherapy: Prospects of Technology Innovation.

[69] Tiberiu Popescu, Alex Cristian Kacsó, Doina Pisla, and Gabriel Kacsó. Brachytherapy next generation: robotic systems. *Journal of Contemporary Brachytherapy*, 7(6):510–514, 2015.

[70] T. K. Podder, N. E. Kalman, G. S. Ibbott, and et al. Aapm and gec-estro guidelines for image-guided robotic brachytherapy: Report of task group 192. *Medical Physics*, 41(10):101501, 2014. Available at PubMed: `https://pubmed.ncbi.nlm.nih.gov/25281939/`.

[71] Zhouping Wei, Gang Wan, Lori Gardi, Gregory Mills, Donal Downey, and Aaron Fenster. Robot-assisted 3d-trus guided prostate brachytherapy: System integration and validation. *Medical Physics*, 31(3):539–548, 2004.

[72] Gerd Strassmann, Peter Olbert, Axel Hegele, Detlev Richter, Emmanouil Fokas, Nina Timmesfeld, Rainer Hofmann, and Rita Engenhart-Cabillic. Advantage of robotic needle placement on a prostate model in hdr brachytherapy. *Strahlentherapie und Onkologie*, 187(6):367, 2011.

[73] Susan Richardson. A 2-year review of recent nuclear regulatory commission events: What errors occur in the modern brachytherapy era? *Practical Radiation Oncology*, 2(3):157–163, 2012.

[74] Mark J. Rivard, Dee-Ann Radford Evans, and Ian Kay. A technical evaluation of the nucletron first system: Conformance of a remote afterloading brachytherapy seed implantation system to manufacturer specifications and aapm task group report recommendations. *Journal of Applied Clinical Medical Physics*, 6(1):22–50, 2005.

[75] William Y Song, Kari Tanderup, and Bradley Pieters. *Emerging technologies in brachytherapy*. CRC press, 2017.

[76] Shunsuke Furutani, Takuya Saze, Hitoshi Ikushima, Masataka Oita, Kyousuke Ozaki, Yoshiomi Kishida, Yoshihiro Takegawa, and Hiromu Nishitani. Quality assurance of i-125 seeds for prostate brachytherapy using an imaging plate. *International Journal of Radiation Oncology*Biology*Physics*, 66(2):603–609, 2006.

[77] Eckert & Ziegler BEBIG GmbH. Isocord® - stranded seeds in unique radiation protection magazines, 2024. [Online]. Available: `https://medical.ezag.com/en/products/isocord/`. [Accessed: 18-Oct-2024].

[78] Andris J. Zauls, Harry Clarke, Michael S. Ashenafi, John M. Watkins, and David T. Marshall. Permanent prostate brachytherapy using real-time dosimetry combined with intraoperatively built custom links of seeds provides equivalent dosimetric results as traditional gun applicators. *Brachytherapy*, 7(2):187, 2008.

[79] Bundesamt für Strahlenschutz (BfS). Strahlenschutzgesetz (strlschg), 2025. [Accessed: 2025-01-17].

[80] Varian Medical Systems. Variseed - brachytherapy treatment planning system, 2025. [Accessed: 2025-01-17].

[81] Katharina I. Jerg, Ernest Chukwudi N. Okonkwo, Frank A. Giordano, Yasser Abo-Madyan, Felix Momm, and Jürgen W. Hesser. Real-time definition of single seed placement sensitivity in low-dose-rate prostate brachytherapy. *Brachytherapy*, 23(2):224–236, 2024.

[82] Suzhou Yifuhui New Materials Co Ltd. The ultimate guide to pom plastic: Understanding polyoxymethylene properties and uses, 2024. Accessed: 23-Dec-2024.

[83] BASF. Medical applications of ultraform® pro (pom), 2024. Accessed: 23-Dec-2024.

[84] Bebig Medical. Products. `https://www.bebigmedical.com/products_34/`. Accessed: 2024-10-09.

[85] CIRS, Inc. Tissue-equivalent ultrasound prostate phantom. `https://www.cirsinc.com/products/all/77/tissue-equivalent-ultrasound-prostate-phantom/`. Accessed: 23-Dec-2024.

[86] Nicholas G. Zaorsky, Brian J. Davis, Paul L. Nguyen, Timothy N. Showalter, Peter J. Hoskin, Yasuo Yoshioka, Gerard C. Morton, and Eric M. Horwitz. The evolution of brachytherapy for prostate cancer. *Nature Reviews Urology*, 14(7):415–439, 2017.

[87] Plato C. Lee, Stuart J. Starr, Kathy Zuhlke, and Brian J. Moran. Comparisons of a proposed five-seed assay method with the single-seed and batch assay methods for i-125 seeds in ultrasound-guided prostate implants. *Radiation Oncology Investigations*, 7(6):374–381, 1999.

[88] Kenichi Tanaka, Ken-ichi Kamo, Kunihiko Tateoka, Osamu Asanuma, Kaori Sato, Hiromitsu Takeda, Koh-ichi Sakata, and Jun Takada. A comparison of the dose distributions between the brachytherapy 125i source models, stm1251 and oncoseed 6711, in a geometry lacking radiation equilibrium scatter conditions. *Journal of Radiation Research*, 56(2):366–371, 01 2015.

[89] Toshiba Semiconductor & Storage Products. Tcd1304dg - linear image sensors, 2024. [Online]. Available: https://toshiba.semicon-storage.com/ap-en/semiconductor/product/linear-image-sensors/detail.TCD1304DG.html. [Accessed: 18-Oct-2024].

[90] Eljen Technology. Ej-200 scintillator characteristics, 2024. Accessed: 10-Mar-2024.

[91] M. Moszynski, M. Kapusta, M. Mayhugh, D. Wolski, and S.O. Flyckt. Absolute light output of scintillators. *IEEE Transactions on Nuclear Science*, 44(3):1052–1061, 1997.

[92] Oncology Medical Physics. Iodine-125. Accessed: 23 October 2024.

[93] National Institute of Standards and Technology (NIST). X-ray mass attenuation coefficients - pyrex glass. https://physics.nist.gov/PhysRefData/XrayMassCoef/ComTab/pyrex.html. Accessed: 23 October 2024.

[94] Andor Technology (Oxford Instruments). Quantum efficiency (qe) in high energy ccd detectors. https://andor.oxinst.com/learning/view/article/quantum-efficiency-(qe)-in-high-energy-ccd-detectors. Accessed: 23 October 2024.

[95] MathWorks, Inc. *Wavelet Denoising and Nonparametric Function Estimation.* Accessed: 09-Jan-2025.

[96] MathWorks, Inc. *wavedec: Multilevel 1-D Wavelet Decomposition.* Accessed: 09-Jan-2025.

[97] MathWorks, Inc. *Savitzky-Golay Filtering: sgolayfilt.* Accessed: 09-Jan-2025.

[98] Eureca Messtechnik GmbH. Eureca line scan cameras. Accessed: 23-Oct-2024.

[99] Bard Medical. Sourcelink. `https://pdf.medicalexpo.com/pdf/bard-medical/sourcelink/78646-133286-_3.html`. Accessed: 10-Jan-2025.

[100] Anelise Ruzzarin, Paulo Alberto Lima da Cruz, Johnny de Almeida Rangel, Carlos José da Silva, Akira Iwahara, and Ricardo Tadeu Lopes. Radioactivity characterization of 125i brachytherapy seeds used in prostate cancer treatment. *Journal of Radioanalytical and Nuclear Chemistry*, 323(2):721–729, 2020.

[101] J J Lifton and S Carmignato. Simulating the influence of scatter and beam hardening in dimensional computed tomography. *Measurement Science and Technology*, 28(10):104001, sep 2017.

[102] J.T.M. de Haas, P. Dorenbos, and C.W.E. van Eijk. Measuring the absolute light yield of scintillators. *Nuclear Instruments and Methods in Physics Research Section A: Accelerators, Spectrometers, Detectors and Associated Equipment*, 537(1):97–100, 2005. Proceedings of the 7th International Conference on Inorganic Scintillators and their Use in Scientific adn Industrial Applications.

[103] Daniel Robertson, Cheukkai Hui, Louis Archambault, Radhe Mohan, and Sam Beddar. Optical artefact characterization and correction in volumetric scintillation dosimetry. *Physics in Medicine and Biology*, 59(1):23, dec 2013.

[104] Toschiba. Tcd1304 ccd sensor documentation, 2016. Accessed: 2024-01-29.

[105] A. Ferrero and Joaquín Campos. Low-uncertainty absolute radiometric calibration of a ccd. *Metrologia*, 48(5):S69–S73, 2011. Accessed: 2024-01-30.

[106] Joelle Helou and Tomer Charas. Acute and late side-effects after low dose-rate brachytherapy for prostate cancer; incidence, management and technical considerations. *Brachytherapy*, 20(5):956–965, 2021.

[107] Liberty Medical Inc. Prostate templates. Accessed: 2024-10-15.

[108] Jaime Urribarri and Peter Orio. Clinical implementation of an in-house made perineal template for low dose rate prostate brachytherapy treatment. *Brachytherapy*, 21(6, Supplement):S95, 2022.

[109] Xuemin Di, Hongtao Zhang, Xiaoli Liu, Jinxin Zhao, Zhen Gao, Huimin Yu, Xiaohua Su, Yansong Liang, and Juan Wang. A new technique for trans-perirectal iodine-125 seed implantation in prostatic cancer guided by ct and 3d printed template: Two case reports. *Frontiers in Oncology*, 12:1031970, 2022. Accessed: 2024-10-15.

[110] D. Lee, T. Li, M. A. Hallman, D. Chen, Y. Dong, B. K. Leachman, I. Veltchev, R. Greenberg, M. L. Sobczak, and E. M. Horwitz. Comparison of toxicities in high dose rate versus low dose rate brachytherapy as monotherapy in patients with low to favorable intermediate risk prostate cancer. *International Journal of Radiation Oncology, Biology, Physics*, 99(2):E252, 2017. Accessed: 2024-10-16.

[111] Juanita Crook, Michael McLean, Charles Catton, Ivan Yeung, John Tsihlias, and Melania Pintilie. Factors influencing risk of acute urinary retention after trus-guided permanent prostate seed implantation. *International Journal of Radiation Oncology*Biology*Physics*, 52(2):453–460, 2002.

[112] Bon Ryu, Jeff Bax, Chandima Edirisinge, Craig Lewis, Jeff Chen, David D'Souza, Aaron Fenster, and Eugene Wong. Prostate brachytherapy with oblique needles to treat large glands and overcome pubic arch interference. *International Journal of Radiation Oncology*Biology*Physics*, 83(5):1463–1472, 2012.

[113] C. Clifton Ling, David Y. Huang, Colleen Barnett, Don Goffinet, Michael Mariscal, L.W. Bob Roberts, Karen K. Fu, and Theodore Phillips. Improved dose distribution with customized i-125 source loading in tem-

porary interstitial implants. *International Journal of Radiation Oncology*Biology*Physics*, 15(3):769–774, 1988.

[114] John S. Muryn and D. Allan Wilkinson. A method for confirming a third-party assay of i-125 seeds used for prostate implants. *Journal of Applied Clinical Medical Physics*, 18(1):53–58, 2017.

[115] Yuki Otani, Takahiro Yamada, Shingo Kato, Naoto Shikama, Kazuto Funakoshi, Isao Kuroda, Hodaka Numasaki, Takayuki Nose, Takushi Dokiya, and Masahiko Oguchi. Source strength assay of iodine-125 seeds sealed within sterile packaging. *Journal of Applied Clinical Medical Physics*, 14(2):253–263, 2013.

[116] Kenichi Tanaka, Satoru Endo, Kunihiko Tateoka, Osamu Asanuma, Ken-ichi Kamo, Kaori Sato, Hiromitsu Takeda, Masaru Takagi, Masato Hareyama, and Jun Takada. Measurement of the strength of iodine-125 seed moving at unknown speed during implantation in brachytherapy. *Journal of Radiation Research*, 55(1):162–167, 06 2013.

[117] Gerald J. Kutcher, Lawrence Coia, Michael Gillin, William F. Hanson, Steven Leibel, Robert J. Morton, Jatinder R. Palta, James A. Purdy, Lawrence E. Reinstein, Goran K. Svensson, Mona Weller, and Linda Wingfield. Comprehensive qa for radiation oncology: Report of aapm radiation therapy committee task group 40. *Medical Physics*, 21(4):581–618, 1994.

Appendix

A. Appendix

Table A.1: Summary of statistics for dosimetric parameters for Prostate target volume (PTV Prostate)

PTV Prostate	V100 % (IntraOp)	V150 % (IntraOp)	D90 Gy (IntraOp)	V100 % (ObInp)	V150 % (ObInp)	D90 Gy (ObInp)
Number of Patients	34	34	34	34	34	34
Mean	**98.39**	**62.18**	**194.93**	**99.31**	**59.17**	**194.63**
Median	98.36	62.67	195.30	99.18	61.88	197.67
Standard Deviation	0.69	5.31	5.31	0.29	7.46	13.92
25th Percentile	97.97	59.05	191.44	99.05	59.23	193.54
75th Percentile	98.93	65.83	199.02	99.60	63.17	198.86
Minimum	96.89	50.35	183.74	98.85	26.50	119.23
Maximum	99.46	71.75	205.65	99.86	64.72	204.37

Table A.2: Summary of statistics for dosimetric parameters for OAR Rectum

OAR Rectum	D0.1cm3 Gy(IntraOp)	D2cm3 Gy(IntraOp)	V100 % (IntraOp)	D0.1cm3 Gy(ObInp)	D2cm3 Gy(ObInp)	V100% (ObInp)
Number of Patients	34	34	34	34	34	34
Mean	**164.55**	**98.03**	**5.41**	**156.00**	**98.16**	**0.18**
Median	169.84	97.60	5.03	164.02	101.34	0.16
Standard Deviation	27.29	18.85	5.79	25.17	20.47	0.17
25th Percentile	147.25	85.34	0.18	141.35	87.37	0.01
75th Percentile	187.26	109.87	8.59	173.23	113.78	0.30
Minimum	101.31	57.75	0.00	96.24	54.74	0.00
Maximum	197.93	128.24	19.58	199.81	148.92	0.48

Table A.3: Summary of statistics for dosimetric parameters for OAR Urethra

OAR Urethra	D10 Gy(IntraOp)	D30 Gy(IntraOp)	D10(ObInp)	D30(ObInp)
Number of Patients	34	34	34	34
Mean	**213.13**	**201.42**	**205.45**	**195.60**
Median	212.79	201.12	204.24	195.60
Standard Deviation	9.81	7.33	7.68	5.54
25th Percentile	207.29	196.65	201.11	192.16
75th Percentile	216.72	206.09	209.36	200.35
Minimum	187.76	178.84	190.06	183.16
Maximum	238.45	216.80	233.51	203.75

```
    % Setup calibration data
    function [linearModel] = setupCalibrationData()
    % Define calibration data (integrated areas and reference activities)
    integratedAreas = [7645395987.510, 5608682980.979, 4885634219.294,
        1508013080.740, 2508452427.411, 2301833134.175];
    referenceActivities = [0.506, 0.448,0.489, 0.059, 0.122, 0.054];

    % Perform a linear regression model fit
    linearModel = fitlm(integratedAreas, referenceActivities, 'RobustOpts',
         'on');
    end

    % Estimate and display activity based on Lorentzian fit
    function estimateAndDisplayActivity(lorentzFit, seedLength,
        pixelNumbers, FWHM_Gauss_mm, FWHM_Lorentz_mm)
    % Set up calibration data for activity estimation
    [linearModel] = setupCalibrationData();

    % Calculate the total area under the Lorentzian curve
    totalArea = integrateLorentzian(lorentzFit, min(pixelNumbers), max(
        pixelNumbers));

    % Estimate the activity based on the total area under the Lorentzian
        curve
    totalActivity = calculateActivity(totalArea, linearModel);

    % Display the estimated activity and FWHM values
    displayActivityResults(totalActivity, seedLength, totalArea,
        FWHM_Gauss_mm, FWHM_Lorentz_mm);
end
```

Listing A.1: The linear calibration data correlating the reference activities with the integrated area.

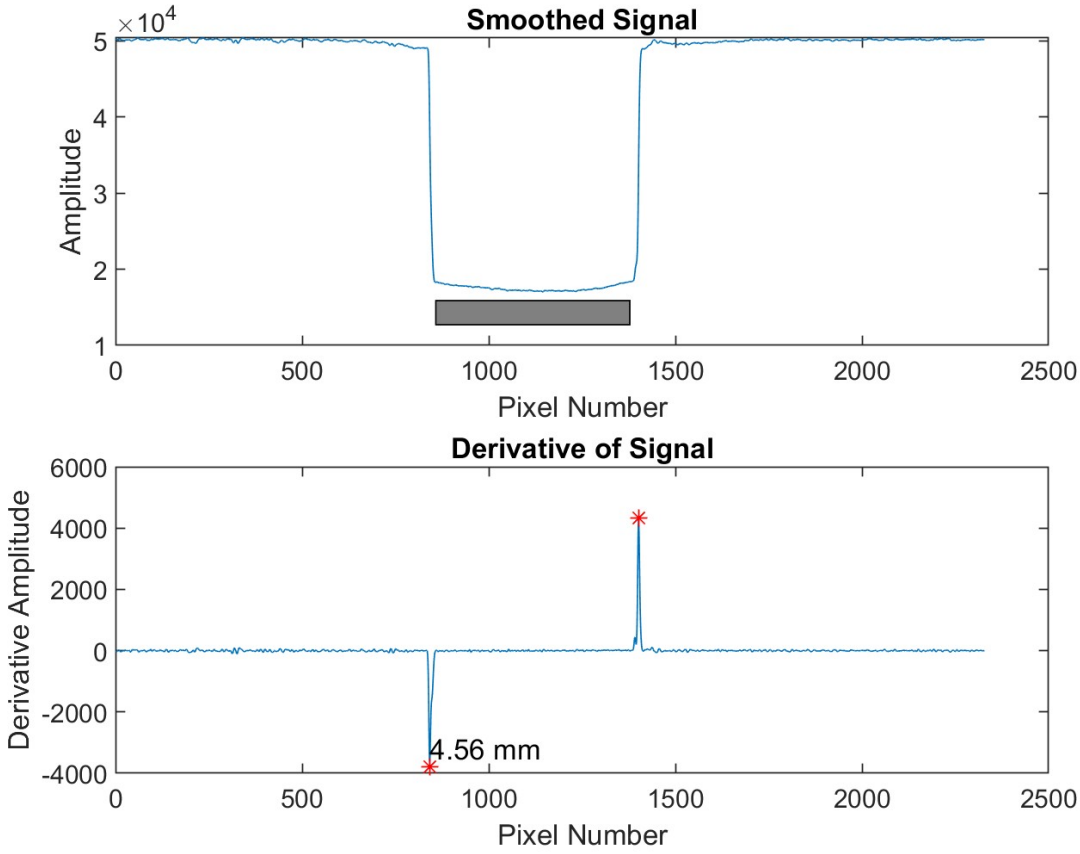

Figure A.1: Single seed signal

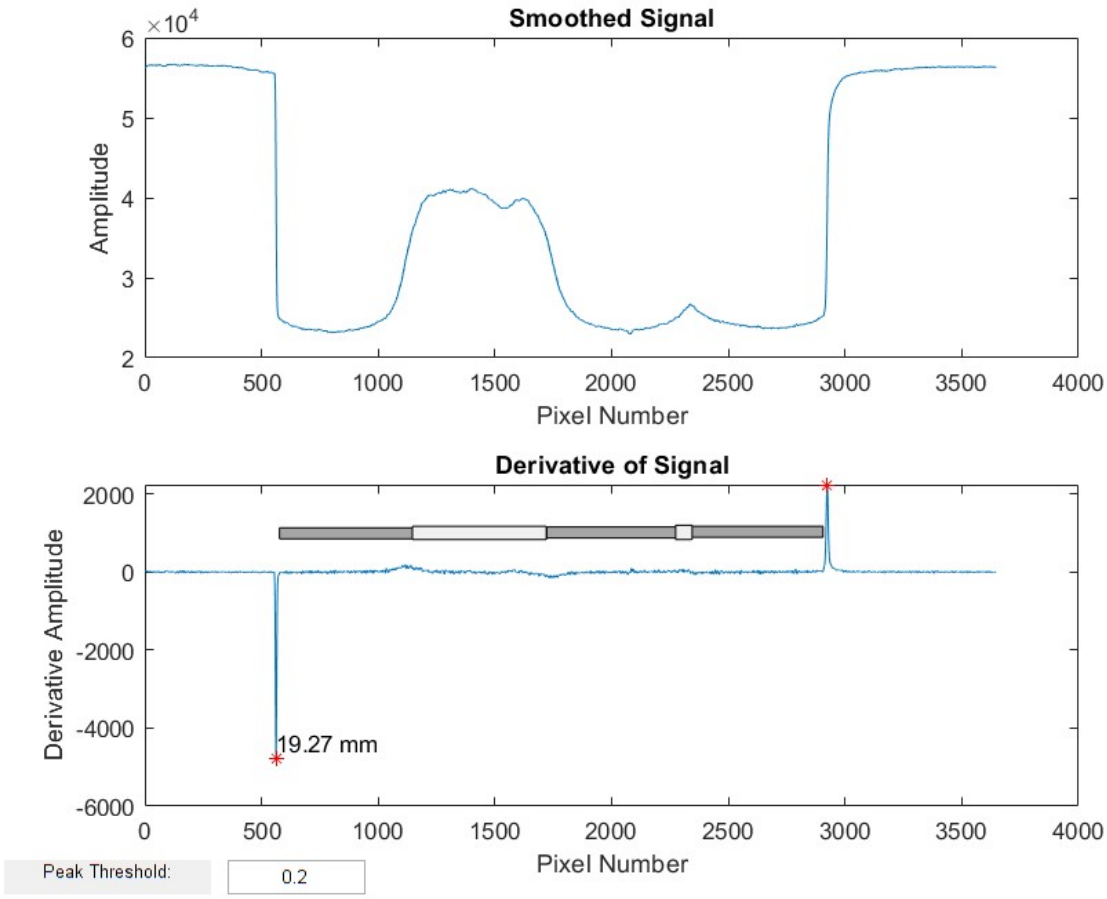

Figure A.2: Seed Space Seed Seed strand signal

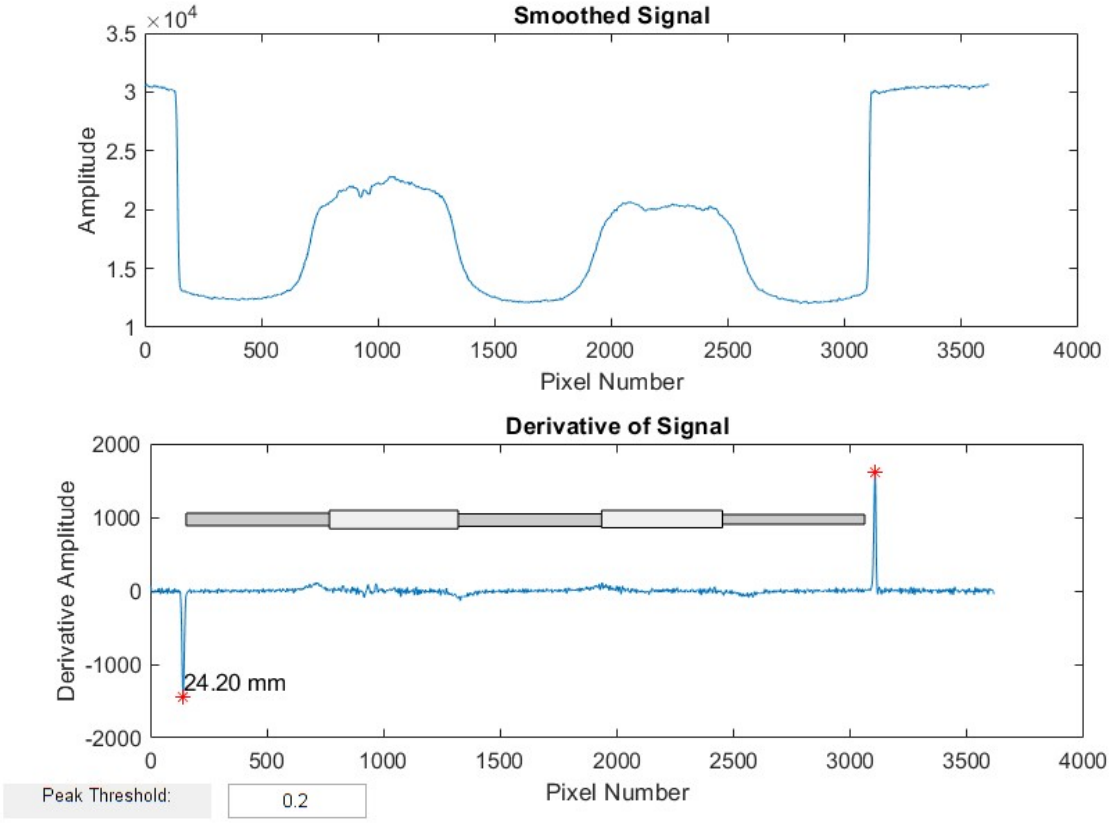

Figure A.3: Seed Space Seed Space Seed strand with a graphic for visualisation of the pattern

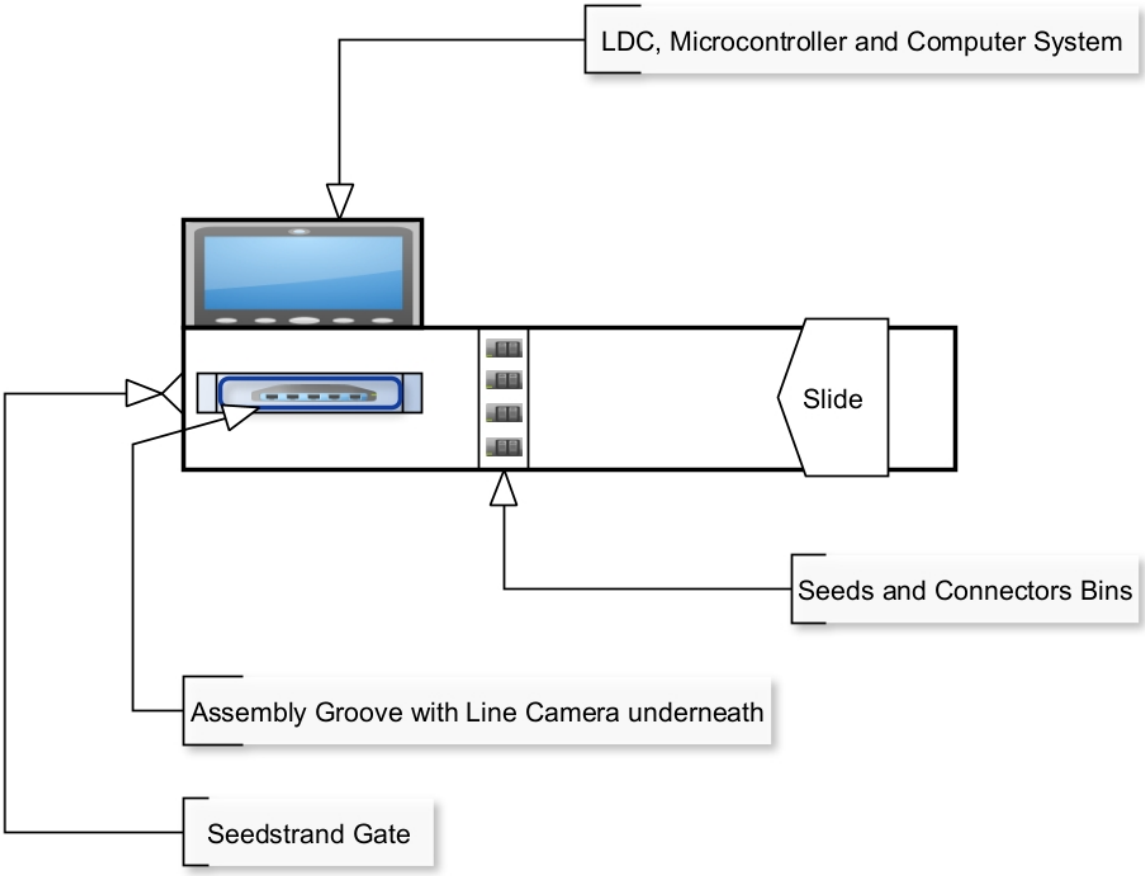

Figure A.4: Sketch of the proposed modernisation of the current QuickLink™ loader

A.1 Detailed estimation of the number of photons detected

1. Activity Conversion to Becquerel

- Assumed Activity: $0.464\,\text{mCi}$
- Conversion factor: $1\,\text{mCi} = 3.7 \times 10^7\,\text{Bq}$
- Activity in Bq:

$$0.464 \times 3.7 \times 10^7 = 1.7168 \times 10^7\,\text{Bq}$$

2. Photon Emission Rate

- Assuming each decay results in the emission of one or more photons, the photon emission rate corresponds to the decay rate (Bq) of the I-125

source:

$$1.7168 \times 10^7 \text{ photons/s}$$

3. Transmission Through Glass

- Glass thickness[89]: $0.7\,\text{mm} = 0.07\,\text{cm}$
- Mass Attenuation Coefficient[93] (μ/ρ): $0.616\,\text{cm}^2/\text{g}$(Approximation for energies around 27-35 keV)
- Density of Glass: $2.5\,\text{g/cm}^3$
- Linear Attenuation Coefficient (μ):

$$0.616 \times 2.5 = 1.54\,\text{cm}^{-1}$$

- Transmission (T):

$$\exp(-1.54 \times 0.07) \approx 0.90$$

4. Geometric Factor

- Detector area (A):

$$29.1\,\text{mm} \times 8\mu\text{m} = 0.2328\,\text{mm}^2 = 2.328 \times 10^{-7}\,\text{m}^2$$

- Distance from source to detector (d):

$$0.7\,\text{mm} = 0.0007\,\text{m}$$

- Solid Angle (Ω):

$$\frac{A}{d^2} = \frac{0.0000002328}{(0.0007)^2} \approx 0.475\,\text{sr}$$

- Fraction of photons hitting the detector:

$$\frac{\Omega}{4\pi} \approx \frac{0.475}{4 \times 3.14} = 0.0378$$

5. Effective Photons Detected

- Photons impacting the CCD:

$$1.7168 \times 10^7 \times 0.90 \times 0.0378 \approx 584,055 \,\text{photons/s}$$

6. Energy Absorption

- Energy absorbed is given as:

$$\text{Energy absorbed} = \text{Initial photon energy} \times \left(1 - e^{-\mu_{\text{glass}} \times 0.07}\right)$$

- Assumption of an average energy of 27 keV:

$$\text{Energy absorbed} = 27\,\text{keV} \times \left(1 - e^{-1.54 \times 0.07}\right)$$

- Thus, the energy absorbed is approximately:

$$\text{Energy absorbed} \approx 27\,\text{keV} \times 1.1023 \approx 2.65\,\text{keV}$$

7. Photons Detected after considering QE

- Assuming QE: 10% (or 0.10)
- Photons detected:

$$584,055 \times 0.10 \approx 58,405 \,\text{photons/s}$$

The calculation results indicated that the measurement time must be considered in order to measure a sufficient number of photons.

Optimal exposure time and frame rate

For a frame rate of **30 Hz**, each frame must be captured within **33.3 ms**. This is calculated as:

$$\text{Total time per frame} = \frac{1\,\text{s}}{30\,\text{frames}} = 33.3\,\text{ms}$$

Readout Time is calculated as:

$$\text{Readout Time} = \frac{\text{Number of Pixels}}{\text{Data Rate}} = \frac{3648}{500,000} = 7.3\,\text{ms}$$

Thus, the exposure time for 30 Hz is:

$$\text{Exposure Time} = 33.3\,\text{ms} - 7.3\,\text{ms} = 26\,\text{ms}$$

The optimal setup for **30 Hz** is as follows:

- **Exposure time**: 26 ms
- **Readout time**: 7.3 ms
- **Frame rate**: 30 Hz
- **Total time per frame**: 33.3 ms

For a frame rate of **60 Hz**, each frame must be captured within **16.7 ms**. This is calculated as:

$$\text{Total time per frame} = \frac{1\,\text{s}}{60\,\text{frames}} = 16.7\,\text{ms}$$

With the same readout time:

$$\text{Exposure Time} = 16.7\,\text{ms} - 7.3\,\text{ms} = 9.4\,\text{ms}$$

The optimal setup for **60 Hz** is as follows:

- **Exposure time**: 9.4 ms
- **Readout time**: 7.3 ms
- **Frame rate**: 60 Hz
- **Total time per frame**: 16.7 ms

B. Complete list of Publications

Peer-reviewed publications included in this dissertation

- Felix Fels, **Ernest Okonkwo**(Contributed equally), Jörg Günter Großmann, Thomas Schadt, Sebastian Laschke, György Lövey, Dieter Lansing, Ulrich Freund, Reiner Steurer, Felix Momm "Permanent interstitial low-dose-rate brachytherapy for prostate cancer: institutional experience with implementation and predictive factors for outcome and side effects", *Journal of Radiotherapy in Practice*, 2023.
- **Ernest Okonkwo**, Günter Grossmann,Felix Fels, Thomas Schadt, Sebastian Laschke, Reiner Steurer, Felix Momm, Jürgen Hesser "Post-intraoperative planning: a strategy for shortening the learning curve and developing knowledge-based low-dose-rate prostate brachytherapy." *Publisher. Springer Nature.*
- Acceptance letter for the manuscript:

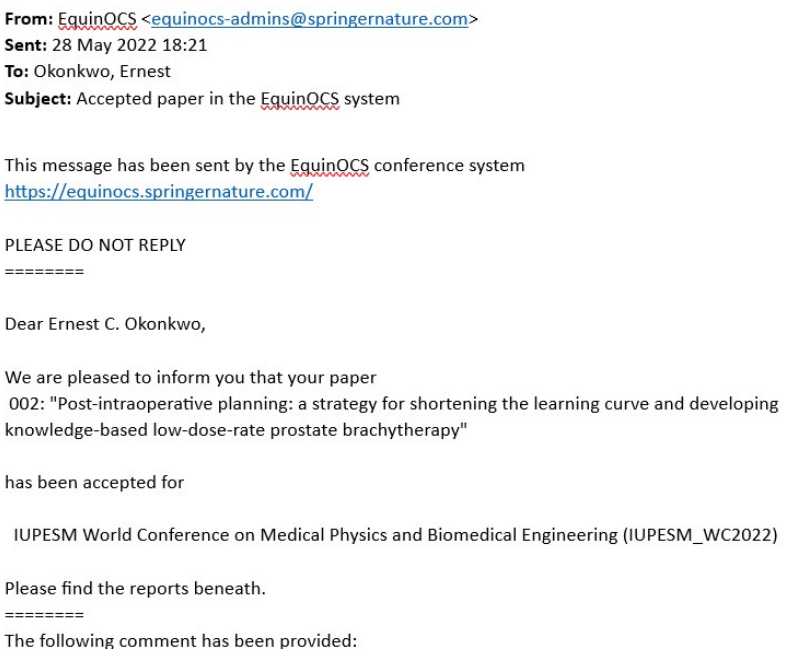

From: EquinOCS <equinocs-admins@springernature.com>
Sent: 28 May 2022 18:21
To: Okonkwo, Ernest
Subject: Accepted paper in the EquinOCS system

This message has been sent by the EquinOCS conference system
https://equinocs.springernature.com/

PLEASE DO NOT REPLY
========

Dear Ernest C. Okonkwo,

We are pleased to inform you that your paper
002: "Post-intraoperative planning: a strategy for shortening the learning curve and developing knowledge-based low-dose-rate prostate brachytherapy"

has been accepted for

IUPESM World Conference on Medical Physics and Biomedical Engineering (IUPESM_WC2022)

Please find the reports beneath.
========
The following comment has been provided:

Other peer-reviewed publications

- Zanzem Tung, Ndimofor Chofor, Pierre Bopda, Rebecca Bücker, **Ernest Okonkwo** " MephidA e.V., Enhancing Radiotherapy Service and Cancer Care in Low Resource Countries", *SAJ Biotechnology*, 5:205, 2018.
- Holger Wirtz, Ralf Müller-Polyzou,Anke Engbert, Rebecca Bücker,Godfrey Azangwe, Tomas Kron, Marian Petrovic, Mahmudul Hasan **Ernest Okonkwo**, and Smith, Jane. "Chapter 17: Emerging Technologies for Improving Access to Radiation Therapy." In *The Modern Technology of Radiation Oncology, Vol 4*, edited by Jacob Van Dyk, vol. 4, ISBN: 9781951134037, 2020.
- Sebastian Hentsch,Kouya Francine Tchintseme, Azeh Ivo, Buecker Rebecca,Henze Larissa, Baiyee Toegel Emily, Bardin Richard, Ngassam Ketchatcham Anny Nadège,**Okonkwo Ernest**,Tung Zanzem Atem. "Implementation, practise and experiences of an international online multidisciplinary tumour board (IMDTB) with a cancer centre in the northwest region of Cameroon", *International Journal of Gynecological Cancer*, 2020.
- Ndimofor Chofor, Pierre Bopda, Rebecca Bücker, Azeh Ivo, **Ernest Okonkwo**, Kra Joel,Zanzem Tung, Taofeeq Ige,Holger Wirtz, Wilfred Ngwa. "Mobilising stakeholders to improve access to state-of-the-art radiotherapy in low- and middle-income countries", *Ecancermedicalscience*, 2021.
- AK.I. Jerg, L. Boggaram Naveen, G. Kanschat, **E.C.N. Okonkwo**, J.W. Hesser, "Diffuse domain approach for flexible needle insertion and relaxation.", *Int J Numer Meth Biomed Engng.*, 2023.
- K.I. Jerg, **E.C.N. Okonkwo**, F.A. Giordano, Y. Abo-Madyan, F. Momm, J.W. Hesser, "Real-time definition of single seed placement sensitivity in low-dose-rate prostate brachytherapy." *Brachytherapy.*, 2023.
- Ntumsi Tontu, William W.Y. Cheung, Marcus Jones, Dennis Palmer,**E.C.N. Okonkwo**, Eric Moore, Keith Streatfield, Laurie Elit, "Developing a modern radiotherapy department in a rural hospital in Cameroon: The Mbingo experience.", *echnical Innovations & Patient Support in Radiation Oncology* , 2024.

ernest.okonkwo@medma.uni-heidelberg.de

+49 1797900212

Am Sahlesbach 8, 77654 Offenburg, Germany

E. Okonkwo

E. Okonkwo

English
Pidgin
Igbo
German
French

Ernest C. N. Okonkwo

Medical Physicist at Ortenau Klinikum Offenburg-Kehl

Work experience

Medical Physicist

Oct 2007 - present

Department of Radiation Oncology

Ortenau Klinikum Offenburg-Kehl

- Radiation Protection Officer
- Implementation of Low dose rate prostate brachytherapy procedure
- Implementation of dosemanagement system
- commissioning of Varian® Truebeam linear accelerator
- Gave a talk at Berlin Digitalization & Innovation Conference 2025

Further Education

Dec 2009 - Jun 2019

- Research Course in Radiotherapy Physics, Madrid/Spain
- Brachytherapy for Prostate Cancer, Avignon/France
- Radiation biology for medical physicists, EUTEMPE-RX, Pavia /Italy
- Varian course „High Energy Clinac Technical Maintenance 1" (Las Vegas/USA)

Education

MSc. in Engineering Physics

Oct 2005 - July 2007

Carl-von-Ossietzky Universität Oldenburg

Specialisation; Medical Physics with MSc thesis at ETH, Zürich

MEng. in Engineering Physics

Oct 2003 - April 2005

Carl-von-Ossietzky Universität Oldenburg

Specialisation; Biomedical Engineering

BSc. in Engineering Physics

Oct 2000 - Sept 2003

Carl-von-Ossietzky Universität Oldenburg

Specialisation; Biomedical Physics.

Certifications

“Fachanerkennung für Medizinische Physik” in Radiation therapy **24.06.2017**

Deutsche Gesellschaft für Medizinische Physik e.V. (DGMP)

Publications

Felix Fels, ***Ernest Okonkwo****(Contributed equally), Jörg Günter Großmann, Thomas Schadt, Sebastian Laschke, György Lövey, Dieter Lansing, Ulrich Freund, Reiner Steurer, Felix Momm*. **"Permanent interstitial low-dose-rate brachytherapy for prostate cancer: institutional experience with implementation and predictive factors for outcome and side effects"** *Journal of Radiotherapy in Practice (2023)*

Ernest Okonkwo*, Günter Grossmann,Felix Fels, Thomas Schadt, Sebastian Laschke, Reiner Steurer, Felix Momm, Jürgen Hesser*. **"Post-intraoperative planning: a strategy for shortening the learning curve and developing knowledge-based low-dose-rate prostate brachytherapy."** *Publisher. Springer Nature/Submitted and accepted*

AK.I. Jerg, L. Boggaram Naveen, G. Kanschat, ***E.C.N. Okonkwo****, J.W. Hesser.*. **"Diffuse domain approach for flexible needle insertion and relaxation."** *Int J Numer Meth Biomed Engng. (2023)*

K.I. Jerg, ***E.C.N. Okonkwo****, F.A. Giordano, Y. Abo-Madyan, F. Momm, J.W. Hesser.*. **"Real-time definition of single seed placement sensitivity in low-dose-rate prostate brachytherapy."** *Brachytherapy. (2023)*

Taofeeq Abdallah Ige, and ***E.C.N. Okonkwo***. **"MEDICAL PHYSICS IN NIGERIA – A ROAD MAP."** *Deutsche Gesellschaft für Medizinische Physik ISBN 3-925218-88-2 (2010)*

Project participation

*Ntumsi Tontu, William W.Y. Cheung, Marcus Jones, Dennis Palmer,****E.C.N. Okonkwo****, Eric Moore, Keith Streatfield, Laurie Elit*. **"Developing a modern radiotherapy department in a rural hospital in Cameroon: The Mbingo experience."** *Technical Innovations & Patient Support in Radiation Oncology(2024)*

*Claire Dempsey, Iyobosa Uwadiae,Sola Osunsami, Joshua Audu,Bode Ogunleye,****Ernest Okonkwo****.*. **“National Medical Physics Certification Programs for Low-Middle Income Countries (Project CERTIPHY).”** *ESTRO 2024,Volume 194 Supplement, 1S2-S6038, Radiotherapy & Oncology (2024)*

Book Contribution

Holger Wirtz, Ralf Müller-Polyzou,Anke Engbert, Rebecca Bücker,Godfrey Azangwe, Tomas Kron, Marian Petrovic, Mahmudul Hasan ***Ernest Okonkwo****, and Smith, Jane.*. **“Chapter 17: Emerging Technologies for Improving Access to Radiation Therapy.”** *The Modern Technology of Radiation Oncology, Vol 4(2020), dited by Jacob Van Dyk, vol. 4, ISBN: 9781951134037, 2020.*

Poster and Presentation

*Sebastian Hentsch,Kouya Francine Tchintseme, Azeh Ivo, Buecker Rebecca,Henze Larissa, Baiyee Toegel Emily, Bardin Richard, Ngassam Ketchatcham Anny Nadège,**Okonkwo Ernest**,Tung Zanzem Atem*. **"Implementation, practise and experiences of an international online multidisciplinary tumour board (IMDTB) with a cancer centre in the northwest region of Cameroon",** *International Journal of Gynecological Cancer (2020)*

*Vanessa Ruf, Felix Fels, Felix Momm, Jörg Günter Großmann, Reiner Steurer,**Okonkwo Ernest**.*. **"Dose assessment of staff and radiation protection in the operating theatre during low dose rate (LDR) brachytherapy for prostate cancer",** *DEGRO 2019 in Münter*

***Okonkwo Ernest**, Tung Zanzem, Chofor Mark, Bopda Pierre.*. **"Eliminating global medical physics disparities"** *World Congress on Medical Physics and Biomedical. Engineering prague, IUPESM Prague 2018*

***Okonkwo Ernest**, Lydia Asana, Rebecca Bücker, Richard Samba, Wilfred Ngwa.*. **"Harambee: tuning African brain drain to gain in global radiation oncology using information and communication technology",** *International Conference on Advances in Radiation Oncology (ICARO2-2017)*

*Richard Ndi Samba, Augustin Simoa, **Okonkwo Ernest***. **"Situation of Radiation Therapy, Cancer Diagnosis and Radiation Protection of Patients in Cameroon"** *Proceedings of the 14th International Congress of the International Radiation Protection Association, ISBN 978-0-9989666-2-5), (2016)*

*M. K. Tchitnga, and **Okonkwo Ernest***. . **"Stand der Technik – Strahlentherapie in Kamerun"** *47. JAHRESTAGUNG DER DEUTSCHEN GESELLSCHAFT FÜR MEDIZINISCHE PHYSIK (2016)*

Awards

Harvard Global Health Catalyst AiD Impact Award: for MEPHIDA e.V., www.globalhealthcatalystsummit.org

Internships

02/2006 – 05/2006 *MeVis GmbH, Bremen* – Analysis of CT data based on statistical parameters.
03/2004 – 12/2004 *University of Oldenburg* – Department for Automation and Measurement Technology.
09/2002 – 02/2003 *Rijksuniversiteit Groningen, Netherlands* – Department for Biomedical Engineering.

Research Interests

Brachytherapy, Radiology

Computer Programming

MATLAB, LabVIEW

Hobbies

Mountain biking, Football, Computer, Travelling

C. Acknowledgment

I would like to express my sincere gratitude to Prof. Dr. Jürgen Hesser, for giving me the opportunity to work in his group. I am grateful for the continuous guidance and support that I received and for letting me work and contribute to the prostate cancer treatment modality, which is part of our treatment options for our prostate cancer patients. Thank you for allowing me the opportunity to explore my own ideas based on my clinical experiences and enriching it with your wide-range research experience.

I am thankful to Prof. Dr. Felix Momm, whose collaboration was crucial in re-establishing low-dose-rate prostate brachytherapy in the department of radiation oncology and radiation therapy at the Ortenau Clinic Offenburg-Kehl. Your partnership as chief radiation oncologist has been a cornerstone of this endeavour.

A special thanks to Dr. Katharina Jerg, for her collaborations and also Prof. Dr. Wilfred Ngwa for the encouragement.

I would also like to express my appreciation to my siblings and parents for their unconditional support and encouragement, and particularly to my mom, who encouraged me despite knowing the demands of family and work responsibilities I had.

Above all, I thank my wife and our four wonderful children that God has blessed us with, for their constant support and understanding have been my bedrock throughout the years. Thank you.